The effect of compensator-induced scatter on external beam dose calculations

BY

FREDERIK CARL PHILIPPUS DU PLESSIS

Thesis submitted to comply with the requirements for the Ph.D degree in the Faculty of Health Sciences, Medical Physics Department, at the University of the Free State.

November 2003

Promotor: Prof. C.A. Willemse

CONTENTS

CHAPTER 1 Introduction

1.1 The radiobiological foundation of radio therapy 5
1.2 The evolution of treatment planning for photon beams 6
1.3 Advanced treatment planning for photon beams 7
1.4 Compensators for intensity modulation 7
1.5 Aim 9
1.6 Outline of the study 10
1.7 References 11

CHAPTER 2 Monte Carlo calculation of effective attenuation coefficients for various compensator materials

2 Preface 21
2.1 Introduction 21
2.2 Methods 23
2.3 Results and Discussion 26
2.3.1 Effect of depth and beamlet size 32
2.3.2 Effect of voxel size and compensator retractal distance 44
2.3.3 Effect of flattening filter in real situations 44
2.4 Application of EACs in this study 45
2.5 Conclusion 46
2.6 References 48

CHAPTER 3 Modeling scatter and beam hardening for a pencil beam after traversing a semi-infinite slab of compensator material

3 Preface 52

3.1 Introduction 52
3.2 Methods 54
3.3 Results and Discussion 55
3.3.1 Relative pencil beam dose profiles vs. compensator thickness 56
3.3.2 Modeling relative scatter dose and beam hardening 62
3.4 The depth dependence of α 75
3.5 The depth dependence of β 80
3.6 Dose calculations for real compensators using the modified PBs 83
3.7 Conclusion 84
3.8 References 86

CHAPTER 4 Description and dosimetric evaluation of a pencil beam based compensator planning system for regular open fields

4 Preface 90
4.1 Introduction 90
4.2 Description of the compensator planning system (CPS) 91
4.3 Methods 94
4.3.1 Rebinning a PB from cylindrical to Cartesian co-ordinates 94
4.3.2 Testing the rebinning algorithm 96
4.4 Results and Discussion 97
4.5 Conclusion 105
4.6 References 106

CHAPTER 5 Modeling dose distributions for simple compensators with a pencil beam based compensator planning system

5.1 Introduction 107
5.2 Methods 107
5.2.1 DOSXYZ simulations 108
5.2.2 CPS calculations 109
5.3 Results and Discussion 110

5.3.1 Relative dose profiles for 5x5 cm^2 fields 112
5.3.2 Relative dose profiles for 10x10 cm^2 fields 115
5.3.3 Relative dose profiles for 20x20 cm^2 fields 118
5.3.4 Side penetration correction function 121
5.3.5 The effect of scatter and beam hardening correction 130
5.3.6 The properties of the determined narrow beam EACs 134
5.4 Determination of the shape of a compensator from a known dose weight matrix (DWM) 137

5.4.1 Primary and total scatter dose contributions 142
5.5 Conclusion 144
5.6 References 147

CHAPTER 6 **Retrospective comments and future developments of this study**

6.1 Introduction 150
6.2 Assumptions of this study 150
6.3 Future developments 151
Abstract 153
Acknowledgements 157

CHAPTER 1

Introduction

1.1 The radiobiological foundation of radio therapy

Radiation therapy entails the irradiation of tumors with ionizing radiation that includes particles such as high energy electrons, photons and neutrons. Ionizing radiation imparts energy to the matter it traverses. This imparted energy is expressed as the radiation dose with the unit [Joule/kg] or [Gy]. It is well known that ionizing radiation therapy is applied to control malignant neoplasms but may also induce it through cell mutations.[1 - 3] Cells may undergo a variety of changes due to the effects of radiation which primarily involves breaks in the DNA chain [4, 5] This may cause cell responses [6] such as cell death, sterility, DNA repair or mutations.[7] The type of radiation has also an effect on the cell responses and are related to the relative biological effect (RBE) and the linear energy transfer (LET) of the radiation used.[8] These effects can be studied through cell survival curves, which indicate the fraction of surviving cells as a function of absorbed dose given in a single fraction to the medium. Cell survival can be described by the so-called linear quadratic model. Different cells would give rise to different cell survival curves and the accuracy of the delivered dose would affect the tumor control probability (TCP). The accuracy of the delivered dose to a patient should be within 3 – 5 percent to achieve a standard deviation in TCP of less than 10 percent.[9] Factors like patient motion, inexact placement of the treatment field, and uncertainties in beam monitoring and calibration is among the parameters that cause inaccuracies in the delivered dose. From a treatment planning point-of-view inaccuracies in the dose calculation, e.g. due to inadequate handling of the tissue inhomogeneities, will affect the overall accuracy.[10] These factors are the driving force behind the quest for improving treatment planning techniques in order to achieve a uniform dose to the tumor and a minimal dose to the surrounding healthy tissues. An accuracy of 2 - 3 percent in terms of dose delivery had been proposed to achieve a total accuracy of 5 percent.[9]

1.2 The evolution of treatment planning for photon beams

Radiation causes damage to healthy as well as malignant tissues and it is necessary to plan a radiation treatment before it is implemented on a patient.[11, 12] In order to plan the radiation treatment, sophisticated computer programs [13] are necessary to calculate the distribution of the energy imparted in a model of the patient. This model is derived from a set of CT images [14] of the relevant site in the patient. In the planning stage the number of beams, their field size, as well as their incoming direction into the patient are determined.[15 - 17] These beams are all directed at the target volume as determined from the CT images. Since a patient model is not homogeneous, but a configuration of different tissues and bone types, it is necessary to take these heterogeneities into account. Through the years various dose calculation algorithms that take inhomogeneities into account have been developed. They can be classified into correction based algorithms [18 - 25] such as the generalized Batho and equivalent-tissue-air ratio (ETAR) methods, or beam modeling algorithms [26 - 33] e.g. convolution/superposition methods. Monte Carlo (MC) based dose calculations are considered to be the most accurate method to determine dose distributions in any arbitrary geometrical model including CT based patient models. This is because the MC method is based on the simulation of actual transport processes of particles such as photons end electrons using the basic physical principles. Various codes are available, such as EGS4, MCNP, PENELOPE, ITS3 and others,[34 - 40] for use in particle transport simulations and dosimetry.

These algorithms and MC codes allow us to calculate dose distributions more accurately. With these developments came a shift in the way treatment planning was to be viewed. Most of the conventional treatment planning techniques concentrated on the calculation of the dose distribution for a predetermined set of fields and regular field shapes. Improvements in computing technology and new algorithms now allow even more sophisticated treatment planning techniques, as discussed next.

1.3 Advanced treatment planning for photon beams

Some of the more advanced treatment planning techniques involve conforming the field to the target shape, as determined by the radiation oncologist, as seen from the direction of the beam. This can be done by means of a multileaf collimator (MLC) or the use of cerrobend blocks [41 - 46], which are locally manufactured from a low melting point alloy. These blocks are mounted on a Plexiglas shadow tray in the path of the beam underneath the accelerator radiation head. The purpose of these blocks is to shield some parts of the rectangular beam so that it conforms to the target volume shape. This type of treatment technique is known as conformal therapy.

The current state of the art technique is to modulate the intensity of the field [47 - 50], that is, to modify the energy fluence of the particles in the field. Adding together beams with a pre-determined non-uniform intensity can produce a dose-distribution with a concave shape. This has a benefit to patients when the target volume surrounds or partially surrounds an organ at risk of radiation injury.[51] This process can be achieved by considering the treatment field as a set of smaller sub-fields called beamlets or beam elements. Intensity modulation can be achieved by utilizing a MLC or by the use of compensators. The treatment of cancer by means of modulated beam intensities is called Intensity Modulated Radiation Therapy or IMRT.[52 - 54]

1.4 Compensators for intensity modulation

In certain radiation treatment procedures it is necessary to compensate for missing tissues with the purpose of obtaining a uniform dose distribution at a certain depth in the patient. [55 - 57] The use of a compensator has skin sparing advantages over the use of bolus.[58] Beam modifiers e.g. blocks and compensators influence the radiation dose at a certain reference point in a phantom.[59 - 61] This is mainly attributed to primary radiation attenuation and scatter alteration.[62, 63] Electrons are also liberated from the beam filter and can contribute to the surface dose in a patient.[64] Compensators are not only useful in compensating for missing tissue but can also be utilized as photon beam intensity modulators. Here the emphasis changes from using them as accessories that compensate for missing tissues to accessories that compensate for missing dose. This entails determining the correct shape of the compensator to achieve the desired intensity modulation determined through inverse treatment planning.[65 - 67] Here a certain dose distribution is required in the target volume and the aim is to derive the dose contribution of a set of non-opposing fields directed at the target. Other critical organs might be in the way of the beams and thus require more attenuation of the intensity than beams not traversing these organs at risk. Thus calculating these beam intensity modulations requires the setting up of a constraining function to optimize the dose in the target. [65] This procedure is simplified by subdividing each beam into a set of beamlets [68] or finite sized pencilbeams.[69] By adjusting the relative contribution or weight of each beamlet the optimal dose distribution within the required constraints can be calculated. These assigned weights of the beamlets are related to the thickness of the compensator at the beamlet location. Scatter effects from the compensator make this technique more complicated. This compensator shape has to be derived from the beamlet weights. For the case of obtaining the desired intensity modulation using an MLC, numerous studies have been done.[54, 70] Here the MLC is set to a specific shape and a certain dose is delivered. Then it is set to a new field shape and the procedure is repeated. This is known as the step-and-shoot technique.[71, 72] Others have adapted this technique to the extent where the leaves of the MLC move continuously while the radiation takes place. This is known as dynamic-leaf intensity modulation.[73 - 75] In practice the dose distribution from these beamlets are calculated with Monte Carlo codes such as MCDOSE.[68] The Monte Carlo method is the most accurate way of determining dose distributions in any phantom/patient model.[76 - 80] All other methods [13, 81, 82] have degrees of uncertainty in their dose calculations due to simplifications in the mathematical models that enable quick results. With faster computers and MC codes such as MCDOSE and VMC [34] the need for these less accurate models is rapidly declining although they may give satisfactory results for certain clinical treatments. It has been shown that the Monte Carlo method is the only method accurate enough to calculate dose distributions from beamlets in inverse treatment planning or intensity modulation. [69]

The main contribution of IMRT is to limit the complications in organs at risk without compromising the required dose to the target volume to such an extent that the radiation treatment is not sufficient for proper tumor control.[68, 70, 83] Thus IMRT would enhance the quality of life of the patient. IMRT can be implemented by modulating regular or conformed x-ray beams with compensators. Compensators can be manufactured at the department of radiotherapy at National Hospital using a locally developed automated milling machine to cut out a negative cast of the compensator shape in Styrofoam blocks. With the appropriate inverse planning software IMRT can thus be implemented in a relatively economic way.

1.5 Aim

Currently there is little known of the effects in the form of scatter and beam hardening introduced by the compensator on external beam dose calculations. This is more of a problem in the case of the finite sized beamlets used for IMRT dose calculations. When IMRT is done using an MLC, the shape of the dose distribution from an individual beamlet can be regarded as invariant, because the weighting process only changes the time during which the beamlet is irradiating. However, when IMRT is done using a compensator, the shape of the individual beamlet dose distribution is not invariant any more, but depends on the thickness through changes in scatter and beam hardening effects. It is not clear how the scatter dose enhancement behaves as a function of:

a) beam energy
b) field size
c) and compensating material.

The aim of this study is the following:

1. A systematic analysis of the influence of beam energy, beamlet size and compensating material on the compensator induced attenuation and scatter.
2. Derive a pencil beam model that take these effects into account.
3. Develop a planning system, based on the above model, that can design compensators based on a given dose distribution.
4. Validate the planning system.

1.6 Outline of the study

Compensator materials used in this study include: wax, aluminum, copper, (yellow) brass, and lead. The energies under study include 6, 8 and 15 MV x-rays that correspond to the photon energies used locally. These findings would then pave the way for introducing compensators as intensity modulating devices. As a first approximation the thickness of a compensator can be derived using effective attenuation coefficients (EACs). The derivation and properties of these EACs using the EGS4 based DOSXYZ MC code is the topic of Chapter 2. In Chapter 3 a method is described to parameterize the scatter and beam hardening effects of poly-energetic pencil beams (PBs) after traversing known thicknesses of different compensator materials. These poly-energetic pencil beams were derived using the EGSnrc based DOSRZnrc Monte Carlo code.[84] In Chapter 4 a locally developed code is described that uses these PBs to include the effect of scatter and beam hardening in a compensator calculation model. A fast rebinning technique is described (cylindrical to cartesian co-ordinates) for calculating dose distributions with the superposition method. A validation procedure is described where calculated dose distributions in water are compared with corresponding dose distributions from DOSXYZ MC simulations. In Chapter 5 the code is tested for parallel beams for simple compensator shapes against DOSXYZ MC simulations. An iterative optimization technique is used to derive the shape of the compensator from a matrix of beamlet weights. In Chapter 6 an overview of the study is given.

1.7 References

[1] United Nations Scientific Committee on the Effects of Atomic Radiation, *Sources and Effects of Ionizing Radiation.* United Nations, New York, 1993.

[2] W.F Heidenriech, M.Atkinson and H.G. Paretzke, ‘ Radiation-Induced Cell Inactivation can Increase the Cancer risk.’, Radiation Research **155**, 870 – 872 (2001).

[3] J.U. Schmollack, S.L. Klaumeunzer and J. Kiefer, ‘ Stochastic Radial Dose Distributions and Track Structure Theory.’, Radiation Research. **153**, 469 – 478 (2000).

[4] B.M. Sutherland, P.V. Bennett, J.C. Sutherland and J. Laval, ’ Clustered DNA damages induced by X rays in Human Cells.’ Radiation Research **157**, 611 – 616 (2002).

[5] F. Vázques-Gundín, M.T. Rivero, J. Gosálvez and J.L. Fernández, ’ Radiation-Induced DNA Breaks in Different Human Satellite DNA Sequence Areas, Analyzed by DNA Breakage Detection-Fluorescence *In Situ* Hybridization. Radiation Research **157**, 711 – 720 (2002).

[6] J. Yarnold, ‘ Molecular aspects of cellular responses to radiotherapy.’, Radiotherapy and Oncology **44**, 1 – 7 (1997).

[7] A.P. Casarat, *Radiation Biology*, Prentice-Hall, New Jersey, USA,1968.

[8] G.W. Barendsen, ‘The Relationships between RBE and LET for Different Types of Lethal Damage in Mammalian Cells: Biophysical and Molecular Mechanisms. . Radiation Research **139**, 257 – 270 (1994).

[9] A. Brahme, ‘ Dosimetric Precision Requirements in Radiation Therapy.’, Acta Radiologica Oncology, **23**, 379 – 391 (1984).

[10] M. Goiten, ' Calculation of the uncertainty in the dose delivered during radiation therapy.' , Med. Phys. **12**, 608 – 612 (1985).

[11] A. Upton, 'Cancer induction and non-stochastic effects.', BJR. **60,** 1 – 16 (1987).

[12] J.S. Laughlin, F. Chu, L. Simpson, and C. Watson, 'Radiation Treatment Planning.', Cancer. **39**, 719 – 728 (1977).

[13] A. Ahnesjö, and M.M. Aspradakis, 'Dose calculations for external photon beams in radiotherapy.', Phys. Med. Biol. **44**, R99 – R155 (1999).

[14] C.D. Collins, O. Constant, I. Fryatt, P.R. Blake and C.A. Parsons, 'Relationship of computed tomography tumour volume to patient survival in carcinoma of the cervix treated by radical radiotherapy.', BJR. **67**, 252 – 256 (1994).

[15] M. Goiten, 'Calculation of the uncertainty in the dose delivered during radiation therapy.', Med. Phys. **12**, 608 – 612 (1985).

[16] A.T. Redpath, B.L. Vickery and D.H. Wright, 'A Set Of FORTRAN Subroutines For Optimizing Radiotherapy Plans.', Computer Programs in Biomedicine. **5**, 158 – 164 (1975).

[17] S.C. McDonald and P. Rubin, 'Optimization Of External Beam Radiation Therapy.', Int. J. Radiation Oncology Biol. Phys. **2**, 307 – 317 (1977).

[18] J.R., Cunningham,' Scatter-Air Ratios.', Phys.Med.Biol. **17,** 42 – 51 (1972).

[19] G. Orton.:Progress in Medical Radiation Physics, Chapter 2 'Tissue Inhomogeneity Corrections in Photon-Beam Treatment Planning', Plenum press. New York.1982.

[20] M.R. Sontag, J.J. Battista, M.J. Bronskill, and J.R. Cunningham,' Implications of computed tomography for inhomogeneity corrections in photon beam dose calculations.', Med. Phys.**4,** 143 – 149 (1977).

[21] M.R. Sontag. And J.R Cunningham.' Corrections to absorbed dose calculations for tissue inhomogeneities.', Med.Phys. **4,** 431 – 436 (1977).

[22] M.R. Sontag, and J.R. Cunningham,' The equivalent tissue-air ratio method for making absorbed dose calculations in a heterogeneous medium.', Radiology **129**, 787 – 794 (1978).

[23] H.D. Thames,' First scatter to off-axis points and the Clarkson method.', Phys.Med.Biol. **18,** 444 – 451 (1973).

[24] E. El-Khatib, and J.J. Battista,' Improved lung dose calculation using tissue-maximum ratios in the Batho correction.', Med.Phys. **11,** 279 – 286 (1984).

[25] E. El-Khatib, and J.J. Battista,'Accuracy of lung dose calculations for large-field irradiation with 6 MV x rays.', Med.Phys. **13**, 111 – 116 (1986).

[26] A. Ahnesjo, P. Andreo, and A. Brahme,' Calculation and application of point spread functions for treatment planning with high energy photon beams.', Acta Oncologica **26**, 49 – 51 (1987).

[27] R. Mohan, C. Chui, and L. Lodofsky, ' Differential pencilbeam dose computation model for photons.', Med.Phys.**13**, 64 – 73 (1986).

[28] T.R. Mackie, A.F. Bielajew, D.W.O. Rogers, and J.J. Battista, ' Generation of photon energy deposition kernels using the EGS Monte Carlo code.', Phys. Med. Biol. **33**, 1 – 20 (1988).

[29] M.B. Sharpe, and J.J. Battista,' Dose calculations using convolution and superposition principles: The orientation of dose spread kernels in divergent x-ray beams.', Med. Phys. **20,** 1685 - 1694 (1993).

[30] P. Storchi and E. Woudstra, 'Calculation models for determining the absorbed dose in water phantoms in off-axis planes of rectangular fields of open and wedged photon beams.', Phys. Med. Biol. **40**, 511 – 527 (1995).

[31] E. Wong, Y. Zhu, and J. Van Dyk, ' Theoretical developments on fast transform convolution dose calculations in inhomogeneous media.', Med. Phys. **23,** 1511 - 1521 (1996).

[32] S. Liu, K.B. Lind, and A. Brahme, ' Two accurate algorithms for calculating the energy fluence profile in inverse radiation therapy planning.', Phys. Med. Biol. **38,** 1809 – 1824 (1993).

[33] Y. Liu, F. Yin, and Q. Gao, ' Variation method for inverse treatment planning.', Med. Phys. **26,** 356 – 363 (1999).

[34] I. Kawrakow, M. Fippel, and K. Friedrich, ' 3D electron dose calculation using a Voxel based Monte Carlo algorithm (VMC).', Med. Phys. **23,** 1413 – 1418 (1996).

[35] D.M.J. Lovelock, C.S. Chui, and R. Mohan, ' A Monte Carlo model of photon beams used in radiation therapy.', Med. Phys. **22,** 1387 – 1394 (1995).

[36] D.W.O. Rogers, B.A. Faddegon, G.X. Ding, C.-M. Ma, and We, et al.' BEAM: A Monte Carlo code to simulate radiotherapy treatment units.', Med.Phys. **22,** 503 – 524 (1995).

[37] C.-M. Ma, P. Reckwerdt, M. Holmes, D.W.O. Rogers, and B. Geiser,' DOSXYZ Users Manual', National Research Council of Canada (NRC, Ottawa): 1995.

[38] C. Manfredotti, U. Nastasi, R. Marchisio, C. Ongaro and G. Gervino, ' Monte Carlo simulation of dose distribution in electron beam radiotherapy treatment planning.', Nucl. Instr. Meths. **A291**, 646 – 654 (1990).

[39] W.R. Nelson, H. Hirayama, and D.W.O. Rogers, The EGS4 Code System, SLAC-Report-265, Stanford Linear Accelerator Center (1985).

[40] J.A. Halbleib, and T.A. Melhorn, ITS: The integrated TIGER Series of Coupled Electron/Photon Monte Carlo Transport Codes, Sandia Report SAN 84-0073, Sandia National Laboratories, Alberquerque, New Mexico: 1992.

[41] C.X. Yu, D. Yan, M.N. Du, S. Zhou and L.J. Verhey, 'Optimization of leaf positions when shaping a radiation field with a multileaf collimator.', Phys. Med. Biol. **40**, 305 – 308 (1995).

[42] P.B. Greer and T. van Doorn, 'A design for a dual assembly multileaf collimator', Med. Phys. **27**, 2242 – 2255 (2000).

[43] P. Storchi and E. Woudstra, 'Calculation of the absorbed dose distribution due to irregularly shaped photon beams using pencil beam kernels derived from basic beam data.', Phys. Med. Biol. **41**, 637 – 656 (1996).

[44] P.D. Higgins, D.N. Mihailidis, F.M. Khan, E.J. Lee, and A.S. Ahuja, 'Blocked field effects on collimator scatter factors.', Phys. Med. Biol. **42**, 2435 – 2447 (1997).

[45] J.L. Robar and B.G. Clark, 'A practical technique for verification of three-dimensional conformal dose distributions in stereotactic radiosurgery.', Med. Phys. **27**, 978 – 987 (2000).

[46] A.E. Schach von Wittenau, P.M. Bergstrom and L.J. Cox, 'Patient-dependant beam-modifier physics in Monte Carlo photon dose calculations.', Med. Phys. **27**, 935 – 947 (2000).

[47] M.R. Arnfield, J.V. Siebers, J.O. Kim, Q. Wu and P.J. Keall, 'A Method for determining multileaf collimator transmission and scatter for dynamic intensity modulated radiotherapy.', Med. Phys. **27**, 2231 – 2241 (2000).

[48] V.S. Spirou, and C.S. Chui, 'Generation of arbitrary intensity profiles by dynamic jaws or multileaf collimators.', Med. Phys. **21**, 1031 – 1041 (2000).

[49] M.G. Karlsson, M. Karlsson and B. Zackrisson, 'Intensity modulation with electrons: calculations, measurements and clinical applications.', Phys. Med. Biol. **43**, 1159 – 1169 (1998).

[50] C-M., Ma, T. Pawlicki, M.C. Lee, S.B. Jiang, J.S. Li, J. Deng, B. Yi, E. Mok and A.L. Boyer, 'Energy- and intensity-modulated electron beams for radiotherapy.', Phys. Med. Biol. **45**, 2293 – 2311 (2000).

[51] S Webb, ' The physical basis of IMRT and inverse planning', B. J. Radiol. **76**, 678 – 689 (2003).

[52] D.J. Convery, and M.E. Rosenbloom, 'Treatment delivery accuracy in intensity-modulated conformal radiotherapy.', Phys. Med. Biol. **40**, 979 – 999 (1995).

[53] S. Webb, 'Conformal intensity-modulated radiotherapy (IMRT) delivered by robotic linac-conformality versus efficiency of dose delivery.', Phys. Med. Biol. **45**, 1715 – 1730 (2000).

[54] A. Boyer, L. Xing, , C-M. Ma, B. Curran, A. Kania, and A. Bleier, 'Theoretical considerations of monitor unit calculations for intensity modulated beam treatment planning.', Med. Phys. **26**, 187 – 195 (1999).

[55] F. Ellis, A. Feldman, and R. Oliver, " A compensator for variations in tissue thickness for high energy beams.", Br. J. Radiol. **32**, 421 (1959).

[56] F.M. Khan, V.C. Moore and D.J. Burns, " The Construction of compensators for Cobalt Teletherapy.", Radiology **96**, 187 - 192 (1970).

[57] P.M.K. Leung, J. Van Dyk, and J. Robins, " A method of large irregular field compensation.", B. J. Radiol. **47**, 805 – 810 (1974).

[58] D.M. Robinson and J.W. Scrimger, "Optimized tissue compensators", Med. Phys. **17**, 391 – 396 (1990).

[59] E. El-Khatib, E.B. Podgorsak and C. Pla, "Calculation of dose in homogeneous phantoms for partially attenuated photon beams", Med. Phys. **13**, 928 – 935 (1986).

[60] J.E. Marrs, A.R. Hounsell and J.M. Wilkinson, "The efficacy of lead shielding in megavoltage radiotherapy", Br.J.Radiol. **66**, 140 – 144 (1993).

[61] E. El-Khatib, E.B. Podgorsak and C. Pla, 'Calculation of dose in homogeneous phantoms for partially attenuated photon beams', Med. Phys. **15**, 145 – 150 (1988).

[62] E. Papiez and G. Froese, "The calculation of transmission through a photon beam attenuator using sector integration", Med. Phys. **17**, 281 – 286 (1990).

[63] M.E. Castellanos and J.C. Rosenwald, "Evaluation of the scatter field for high-energy photon beam attenuators", Phys. Med. Biol. **43**, 277 – 290 (1998).

[64] S.J. Thomas and G. Bruce, "Skin dose near compensating filters in radiotherapy", Phys. Med. Biol. **33**, 703 – 710 (1988).

[65] S. Liu, B.K. Lind and A. Brahme, 'Two accurate algorithms for calculating the energy fluence profile in inverse radiation therapy planning.', Phys. Med. Biol. **38**, 1809 – 1824 (1993).

[66] T. Holmes, and T.R. Mackie, 'A comparison of three inverse treatment planning algorithms.', Phys. Med. Biol. **39**, 91 – 106 (1994).

[67] Y. Liu, F. Yin, and Q. Gao, 'Variation method for inverse treatment planning', Med. Phys. **26**, 356 – 363 (1999).

[68] J.S. Li, T. Pawlicki, J. Deng, S.B. Jiang, E. Mok and C-M. Ma, 'Validation of a Monte Carlo dose calculation tool for radiotherapy treatment planning.', Phys. Med. Biol. **45**, 2969 – 2985 (2000).

[69] W. Luab, M. Alber, M. Birkner and F. Nüsslin, 'Monte Carlo computation for IMRT optimization', Phys. Med. Biol. **45**, 1741 – 1754 (2000).

[70] J.H. Kung, G.T.Y. Chen and F.K. Kuchnir, 'A monitor unit verification calculation in intensity modulated radiotherapy as a dosimeter quality assurance.', Med. Phys. **27**, 2226 – 2230 (2000).

[71] J-S. Tsai, M.J. Rivard and M.J. Engler, 'Dependence of linac output on the switch rate of an intensity-modulated tomotherapy collimator.', Med. Phys. **27**, 2215 – 2225 (2000).

[72] S. X. Chang, T.J. Cullip and K.M. Deschesne, ‘Intensity modulation delivery techniques: “Step & shoot” MLC auto-sequence versus the use of a modulator.’, Med. Phys. **27**, 948 – 959 (2000).

[73] R. Svensson, P. Källman and A. Brahme, ‘An analytical solution for the dynamic control of multileaf collimators.’, Phys. Med. Biol. **39**, 37 – 61 (1994).

[74] C. Fiorino, A. Lev, M. Fusca, G.M. Cattaneo, F. Rudello and R. Calandrino, ‘Dynamic beam modulation by using a single computer-controlled absorber.’, Phys. Med. Biol. **40**, 221 – 240 (1995).

[75] F. Verhaegen, and H.H. Liu, ‘Incorporating dynamic collimator motion in Monte Carlo simulations: an application in modeling a dynamic wedge.’, Phys. Med. Biol. **46**, 287 – 296 (2001).

[76] F. Verhaegen, F.M. Buffa and C. Deehan, ‘Quantifying effects of lead shielding in electron beams: a Monte Carlo study.’, Phys. Med. Biol. **46**, 757 – 769 (2001).

[77] W. Van der Zee, and J. Welleweerd, ‘Calculating photon beam characteristics with Monte Carlo techniques.’, Med. Phys. **26**, 1883 – 1892 (1999).

[78] J.J. DeMarco, T.D. Solberg and J.B. Smathers, ‘A CT-based Monte Carlo simulation tool for dosimetry planning and analysis.’, Med. Phys. **25**, 1 – 11 (1998).

[79] H. Neuenchwander, T.R. Mackie and P.J. Reckwerdt, ‘MMC – a high-performance Monte Carlo code for electron beam treatment planning.’, Phys. Med. Biol. **40**, 543 – 574 (1995).

[80] L. Wang, C-S. Chui, and M. Lovelock, ‘A patient-specific Monte Carlo dose-calculation method for photon beams.’, Med. Phys. **25**, 867 – 878 (1998).

[81] T. Knöös, A. Ahnesjö, P. Nilsson, and L. Weber, 'Limitations of a pencil beam approach to photon dose calculations in lung tissue.', Phys. Med. Biol. **40**, 1411 - 1420 (1995).

[82] J.E. McGary, A.L. Boyer and T.R. Mackie, 'A comparison of Monte Carlo and analytic first scatter dose spread arrays.', Med. Phys. **26**, 751 – 759 (1999).

[83] S.A. Leibel, G.J. Kutcher, R. Mohan, L.B. Harrison, J.G. Armstrong and M.J. Zelefsky, 'Three-dimensional conformal radiation therapy at the Memorial Sloan-Kettering Cancer Center.', Semin. Radiat. Oncol. **2**, 274 – 290 (1992).

[84] I. Kawrakow, " Accurate condensed history simulation of electron transport: I. EGSnrc, the new EGS4 version", Med. Phys. **27**, 485 - 498 (2000).

CHAPTER 2

Monte Carlo calculation of effective attenuation coefficients for various compensator materials

2 Preface

One of the parameters that is required for the design of a compensator is the attenuation coefficient for the compensator material. This attenuation coefficient is sometimes termed an effective attenuation coefficient (EAC) when scatter effects and the beam energy spectrum is taken into account for its derivation. This Chapter is based on an extension of a recent publication [36] by the author with the emphasis on determining the EACs of various materials as a function of square beamlet size, to be used for the design of compensators from the beam intensity maps produced by inverse planning techniques.

2.1 Introduction

In certain radiation treatment procedures it is necessary to compensate for missing tissues due to patient surface irregularities, with the purpose of obtaining a uniform dose distribution at a certain depth in the patient.[1 - 3] The use of a compensator has skin sparing advantages over the use of bolus.[4] Beam modifiers e.g. blocks and compensators influence the radiation dose at a certain reference point in a phantom.[5 - 7] This is mainly attributed to primary radiation attenuation and scatter alteration.[8, 9] Electrons are also liberated from the beam filter and can contribute to the surface dose in a patient.[10]

The scatter effect due to beam modifying filters is of the order of 6 % of the transmitted primary dose for a 1cm copper attenuator for 4MV photon beams and becomes more prominent for large fields.[4, 11] Others [12] have studied the broad beam attenuation coefficient for lead at photon energies from Co-60 to 25 MV and found that the measured attenuation coefficients vary by as much as 16 % when compared to narrow beam data. Attenuator induced first order scatter were also studied by means of the analysis of the

Klein-Nishina Compton cross section.[13] It is known that the effective attenuation coefficient for these beam filters and wedges vary as a complicated function of the measurement depth in the phantom, the x ray beam field size, the thickness and material of the filter and the energy of the radiation beam.[14 - 18]

Monte Carlo codes such as DOSXYZ [19] can be used to determine effective attenuation coefficients (EACs) for narrow beams. This quantity depends on field size due to lateral electronic equilibrium that becomes important in narrow beam geometries.[20] Data presented by previous authors [21, 22] are mostly from measurements and does not include a comprehensive number of materials typically used for compensator manufacturing. The use of compensators has also shifted towards a need for obtaining uniform dose distributions in complete target volumes. Advanced radiation treatment planning such as inverse treatment planning can be used with compensators for intensity modulated radio therapy (or IMRT) purposes.

One way of modeling the compensator is by dividing the photon beam into a set of beamlets or beam elements and using their weights as a basis for compensator design.[23] The desired beam modulation is then obtained by determining the required thickness of the attenuator corresponding to the intensity of each beamlet, using EACs.

In this study the aim is to study the effect of field (beamlet) size, depth and material on the EAC using the DOSXYZ Monte Carlo code. Compensator materials namely wax, copper, brass, lead and aluminum were used with x-ray energies of 6 MV, 8 MV and 15 MV. The coefficients were derived for small fields corresponding to typical beamlet dimensions as used in beamlet based [24] treatment planning algorithms. Monte Carlo codes such as MCDOSE [24] perform dose calculations in a patient model by dividing a beam into a set of beamlets. The dose contribution from each beamlet is then weighted according to a pre-calculated intensity map obtained from an optimization algorithm. The desired beam intensity modulation in practice can then be obtained from the manipulation of the leaf settings of an MLC [25] or from the use of a compensator. Knowledge of the absorbed dose variation as a function of attenuator material, attenuator cross section area, attenuator thickness and its variation over depth in a water phantom is required for compensator manufacturing.

2.2 Methods

The EGS4 [26] user code DOSXYZ was used to determine EACs for various attenuator materials by calculating the central axis depth dose in a water phantom.

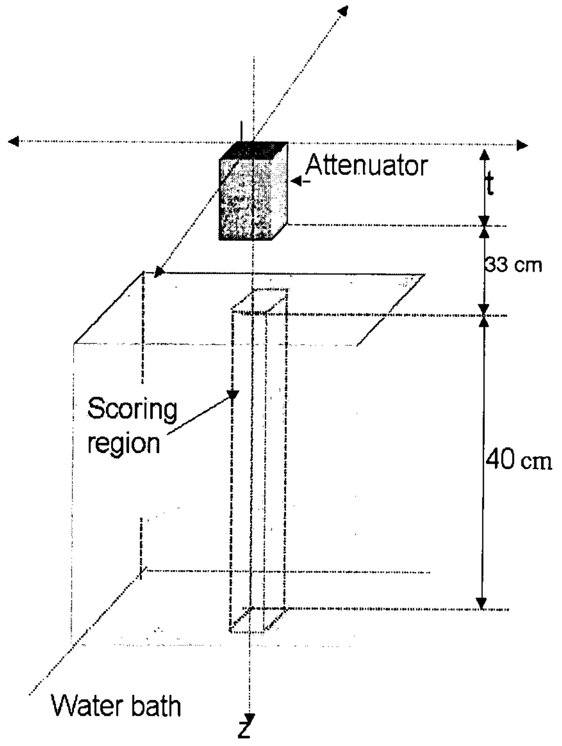

Figure 2.1. The DOSXYZ geometry used for the determination of the effective attenuation coefficient for various attenuators. The beamlet area and thickness (t) of a block of compensator material were varied and the dose was scored in the scoring region consisting of voxels with x, y and z dimensions of 0.5, 0.5 and 1 cm respectively. Between the attenuator and the water phantom there was a 33 cm airgap. The dimensions of the water phantom was 40 cm in the x, y and z directions.

Figure 2.1 shows the geometry of the water phantom as well as the location of the attenuator. The attenuator and water phantom were incorporated into the same geometry. The dimensions of the water phantom were 40x40x40 cm^3. The distance from the bottom of the attenuator to the top plane of the water phantom was 33 cm. The thickness (t) and the area of the attenuator were varied to coincide with beamlet dimensions. The attenuator materials that were used consisted of wax, copper, brass, lead and aluminum. The x-ray source used was a parallel beam incident perpendicularly to the xy-plane and its beam axis coincided with the z-axis of the DOSXYZ co-ordinate system. The depth dose was scored in a column of voxels, centered on the z–axis of the phantom, with dimensions of 0.5x0.5x1.0 cm^3 in the x, y and z directions respectively. This column extended to 40 cm in depth. Input energy spectra corresponding to 6, 8 and 15 MV x-ray sources were used. These spectra were obtained from previous BEAM [27] simulations for a Philips SL75/5 (6MV), a Philips SL75/14 (8MV) and a Philips SL25 (15 MV) accelerator. The energy spectra were obtained using the BEAMDP [28] code to analyze the phase space files, from the BEAM simulations, which were accumulated in scoring planes located just above the jaws for each accelerator.

The DOSXYZ simulations were performed for attenuator thicknesses of 0, 1, 2, 3, 4, 5, 6, 8, 10, 15, 20, 30, 40 and 50 mm for each compensator material, but the thickness of wax was also extended to 150 mm. These simulations were repeated for a range of square beamlets having areas with side lengths of 0.5, 1.0, 2.0, 3.0 and 5 cm. The depth dose data were analyzed by plotting it as a function of compensator thickness for different beamlet sizes. The number of histories was chosen to reduce the dose variance to below one percent and is a function of the thickness of the compensator media and the voxel size. A thickness of 4 cm of copper required for example 10^8 histories.

Each of the MC generated depth dose curves was normalized to its own maximum dose.

A FORTRAN code was written to fit a 5 parameter double exponential function to these normalized depth dose data from a depth of 4 cm down to 40. The equation is of the form:

$$FDD_{med}(z,A) = \alpha + \beta \exp(-\gamma z) + \delta \exp(-\varepsilon z) \qquad (2.1)$$

The five parameters, indicated by Greek symbols (α-ε), were determined by a least squares minimization method by iteratively choosing and varying the fitted constants at random to obtain the best fit between the MC calculated depth doses and the values calculated from equation 2.1. The fitted values agreed on average within less than one percent locally with the MC generated dose values. In equation 2.1, FDD_{med} indicates the normalized (or fractional) absorbed dose, at depth z, in water as a result of transmitted, attenuator scattered and in-phantom scattered x rays for absorber material, med, for a beamlet size A. The depth dose data beyond 4 cm depth were represented by these smoothing functions to reduce the statistical variance even further below the one percent level. Some representative fitting constants are given in table 2.1. The normalized depth dose data that were calculated using equation (2.1) were subsequently multiplied by the corresponding normalization doses (the maximum doses obtained during the MC calculation) to obtain smoothed absorbed dose data.

EACs were derived by plotting the logarithm of the smoothed depth dose values, for a given compensator material, beam energy and depth as a function of attenuator thickness. A linear regression was performed on these data and the gradient of each fitted line was determined. This yielded the EAC. This follows from the assumption that the absorbed dose at any specific depth in the water phantom can be expressed as:

$$D_{med}(z,A,t) = D_{med}(z,A,t=0)\exp(-\mu_{eff}t) \qquad (2.2)$$

where t, d, A and μ_{eff} represent thickness, depth, beamlet area, and EAC, respectively. $D_{med}(z,A,t=0)$ indicates the dose in water for zero absorber thickness which thus corresponds to the depth dose for an open beamlet of size, A, at depth, z, in water.

Table 2.1: Representative values of the fitting constants that were derived by using equation 2.1. The left-most column indicates the material and in brackets the beam energy, E(MeV), side length of square beamlet size, A(cm), and material thickness, t(cm).

Material(E,A,t)	α	β	$\gamma(cm^{-1})$	δ	$\varepsilon(cm^{-1})$
Wax(8, 5, 8.0)	1.3386	0.0572	-0.2963	0.0816	0.0594
Lead(15,3,3.0)	1.5285	0.0467	-0.4873	0.0800	0.0953
Brass(8,5,1.0)	2.1919	0.0582	-1.1126	0.0765	0.0462
Al(8,2,1.0)	1.6985	0.0382	-0.7632	0.0183	0.1398
Cu(6,5,5.0)	1.3455	0.0381	-0.3124	0.0130	0.1146

2.3 Results and Discussion

Figure 2.2 shows the photon energy spectra used in this study for 6, 8 and 15 MV x-rays respectively.

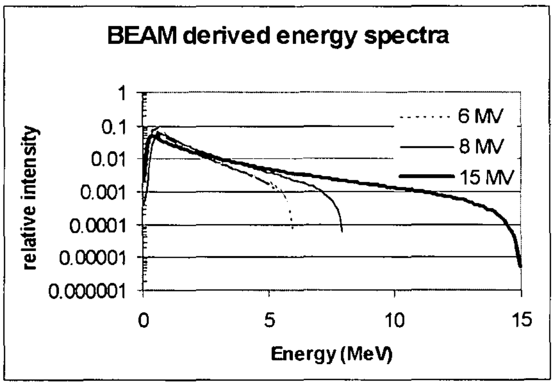

Figure 2.2. The energy spectra derived from the BEAM MC code simulations for the Philips SL75/5 (6MV), Philips SL75/14N (8MV) and Philips SL25 (15 MV) accelerators. The area under each spectrum is normalized to unity.

The EAC for square beamlet areas with side lengths of 0.5, 1.0, 2.0, 3.0 and 5.0 cm are shown in the next series of figures for wax, aluminum, copper, brass, and lead as a function of depth in water. Sets of three figures are shown for each compensator material at three different energies.

Wax Aluminum

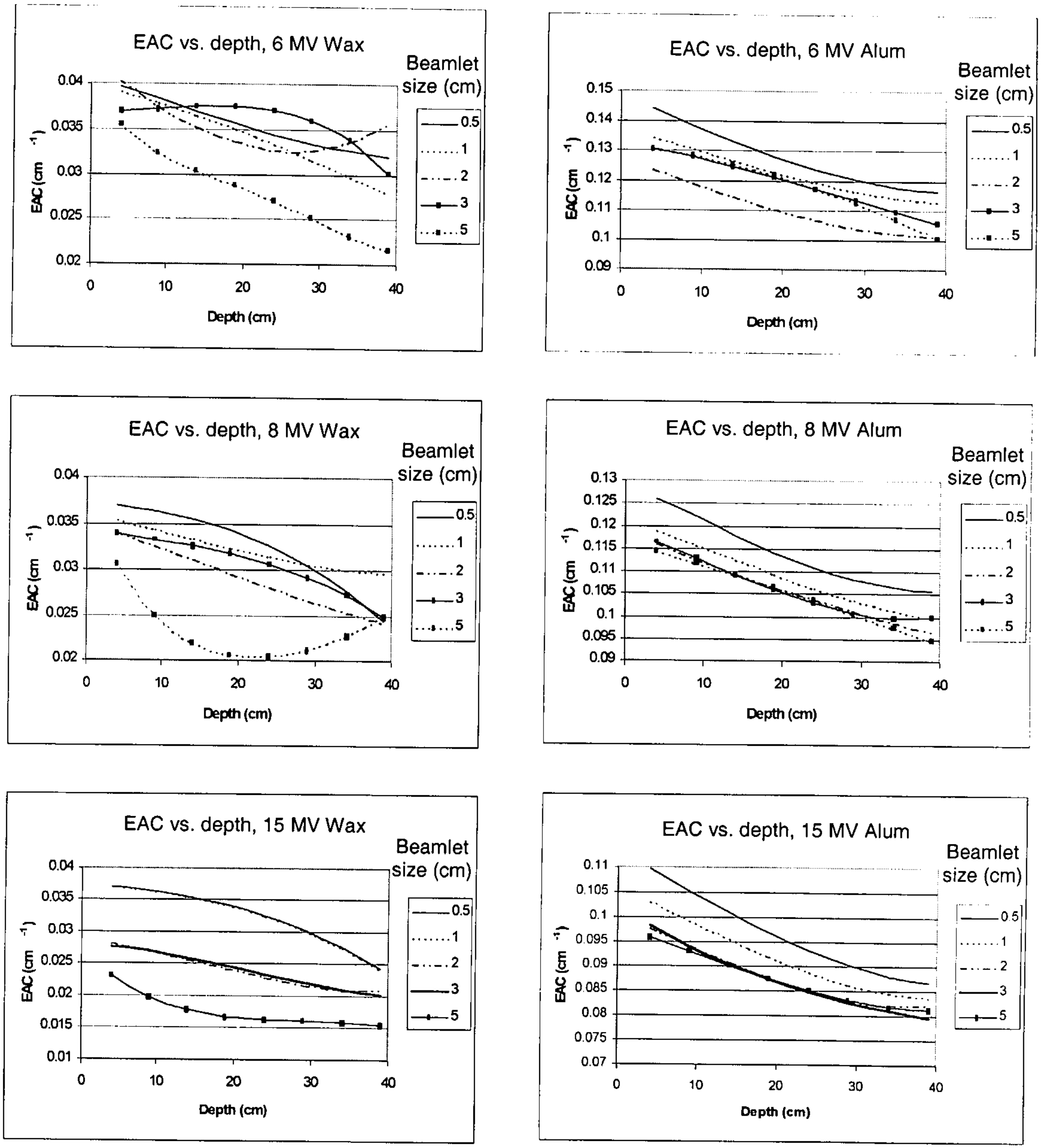

(a) (b)

Figure 2.3 a and b. Column (a) shows the EAC values calculated from depth dose analysis for wax and column (b) shows the corresponding EAC values for aluminum. The legend box in each graph indicate the length of the side of the square beamlet for which the EAC values were calculated.

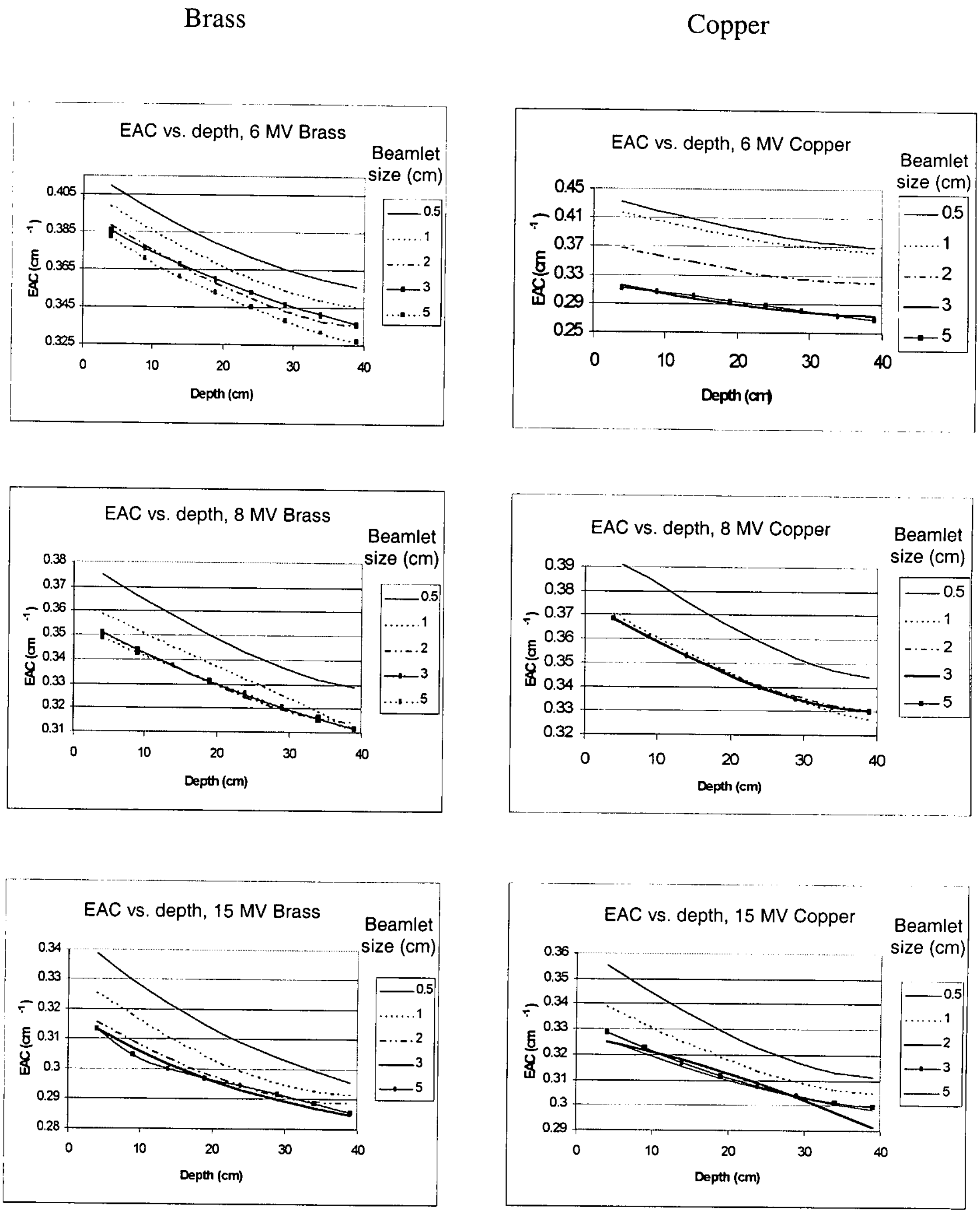

(c) (d)

Figure 2.3 c and d. Column (c) shows the EAC values calculated from depth dose analysis for brass and column (d) shows the corresponding EAC values for copper. The legend box in each graph indicate the length of the side of the square beamlet for which the EAC values were calculated.

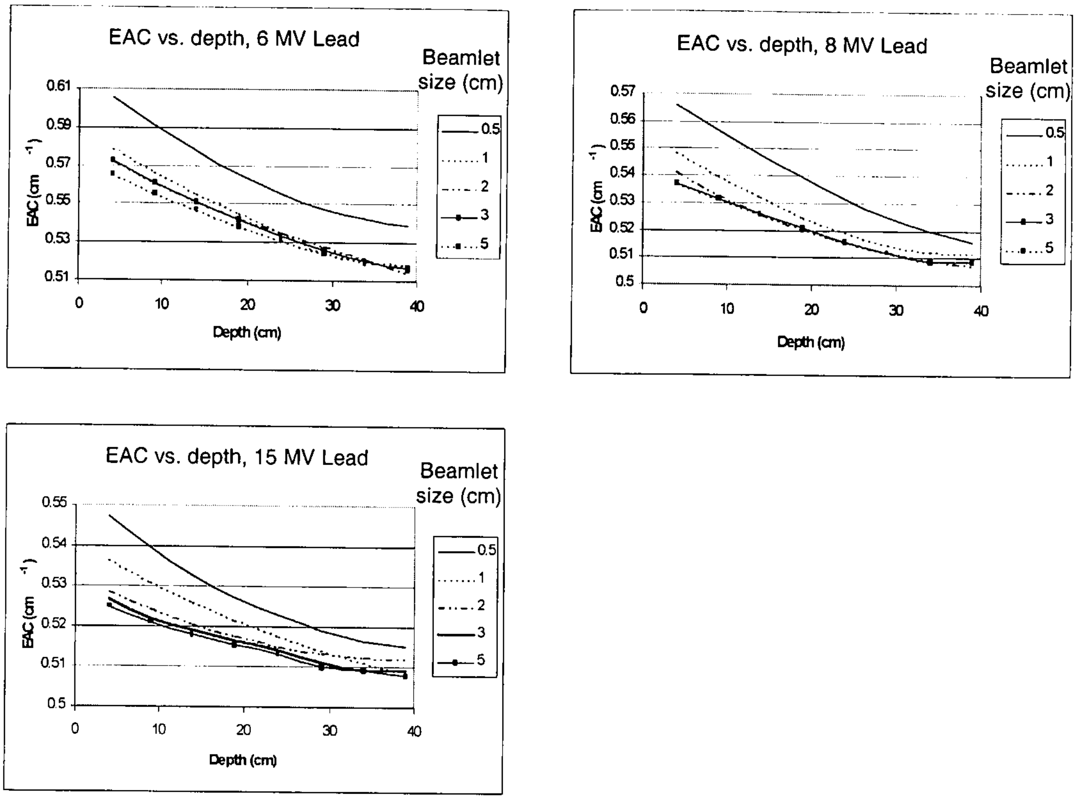

(e)

Figure 2.3 e. EAC values calculated from depth dose analysis for lead. The legend box in each graph indicate the length of the side of the square beamlet for which the EAC values were calculated.

From these plots it is clear that in general the EAC values decrease with depth. This result is true for almost all the materials studied. It is due to: a) beam hardening on the beamlet axis and b), increased scatter as the depth in water increases. The spurious results for wax particularly at 6 MV might be attributed to the fact that wax is not such an efficient beam filter as materials that contain higher atomic number (Z) atoms. The result is that the normalized, smoothed depth dose curves for each thickness of wax will have virtually identical shapes. The normalization doses will also be subjected to statistical variance. The result is that after denormalization, some of the smoothed depth dose data would be overlapping for the thin slabs of wax. This introduces variance on the absorbed dose vs. thickness data. Since the linear function fitted to these data has small slopes (EAC values) for wax, it is highly probable that there is significant variance in their values. The smoothing step introduces artifacts in terms of the behaviour of the EAC with depth and is more prominent for wax when compared to the other materials.

Another feature of these EACs is that their values initially decrease as the beamlet size increases, but then remain relatively constant. This is due to attainment of lateral electronic equilibrium at beamlet sizes of about 2x2 cm^2 and larger. Figure 2.4 is an alternative representation of the data to show how the EAC varies as a function of beamlet size.

Table 2.2: Materials used as beam absorbers in this study for the determination of their effective attenuation coefficients along with their physical densities. The mass electron density is expressed by Z/A.

Material	Density (g/cm^3)	Z	Z/A	Composition (wt%)
Wax (dental)	0.90	5.7*	0.743	C:H:O (83:13:4)
Aluminum	2.69	13	0.482	Al (100)
Brass	8.47	29.3*	0.457	Zn:Cu (34:66)
Copper	8.93	29	0.456	Cu (100)
Lead	11.34	82	0.397	Pb (100)

* Effective atomic number calculated for Z^2 dependence of cross section.

From figure 2.4 it can be observed that the EAC values become relatively constant for beamlet sizes larger than 3x3 cm^2, at all depths.

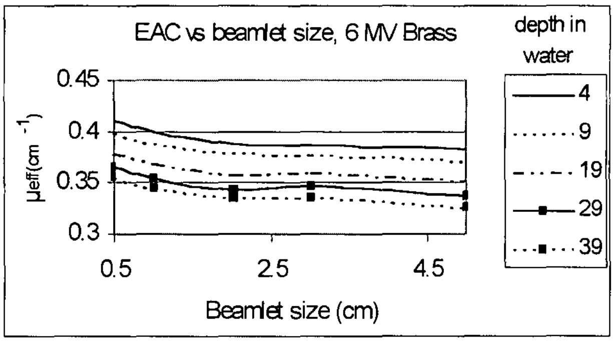

Figure. 2.4. (Bottom of previous page) Effective attenuation coefficients as a function of beamlet area at five constant depths of 4, 9, 19, 29 and 39 cm obtained for brass beam absorbers.

Table 2.3 shows the EAC values for the various materials shown in figures 2.3 (a – e) as a function of field size. The EAC values are tabulated here for a depth of 4 cm in water. The second column displays the values for the narrow beam attenuation coefficient which were calculated using data from Hubbell et. al [29]. These narrow beam EAC values were calculated by using the spectral data shown in figure 2.2. The spectra were re-binned into 1 MeV bins and the corresponding narrow beam linear attenuation coefficients were calculated by weighing the energy related coefficients against the number of photons in the corresponding energy bins. From the table it can be observed that the calculated narrow beam values correspond fairly well to the EAC values for the 0.5x0.5 cm^2 beamlet for copper, brass and aluminum. For wax and lead however the correspondence is not that good.

Table 2.3: Effective attenuation coefficients (EAC) in units of cm^{-1} at a depth of 4 cm in water. These data are shown for various beamlet sizes and beam energies. The second column shows theoretically calculated EAC values based on the spectra in figure 2.2 and on narrow beam attenuation data.

6 MV beam energy	EAC (calculated)	Side length of square beamlet size (cm)				
Material	Narrow beam	0.5	1.0	2.0	3.0	5.0
Wax	0.052	0.039	0.039	0.038	0.037	0.037
Aluminum	0.147	0.144	0.134	0.132	0.131	0.131
Brass	0.411	0.410	0.400	0.389	0.386	0.382
Copper	0.438	0.431	0.417	0.368	0.314	0.311
Lead	0.659	0.605	0.578	0.573	0.571	0.564

8 MV beam energy	EAC (calculated)	Side length of square beamlet size (cm)				
Material	Narrow beam	0.5	1.0	2.0	3.0	5.0
Wax	0.047	0.037	0.035	0.034	0.034	0.031
Aluminum	0.129	0.126	0.119	0.115	0.115	0.114
Brass	0.373	0.375	0.359	0.351	0.350	0.350
Copper	0.407	0.394	0.371	0.368	0.367	0.367
Lead	0.607	0.564	0.548	0.541	0.537	0.537

(continued on next page)

15 MV beam energy	EAC (calculated)	Side length of square beamlet size (cm)				
Material	Narrow beam	0.5	1.0	2.0	3.0	5.0
Wax	0.045	0.037	0.037	0.028	0.028	0.023
Aluminum	0.122	0.110	0.103	0.098	0.098	0.096
Brass	0.371	0.339	0.327	0.316	0.313	0.313
Copper	0.395	0.355	0.338	0.324	0.329	0.325
Lead	0.615	0.545	0.537	0.530	0.527	0.527

2.3.1 Effect of depth and beamlet size

The EAC depend on depth in water as well as beamlet size as shown in figures 2.3 and 2.4. Because the depth dependence is seen to be approximately linear (wax being an exception) the dependence of the EAC on depth and field size was approximated by the following equation:

$$\mu_{eff} = \mu_0(1-\mu_1 S^{\frac{1}{3}}) - \mu_2 d \tag{2.3}$$

The parameters μ_0, μ_1 and μ_2 have the following meanings: μ_0 is the theoretical narrow beam attenuation coefficient (see column 2 in table 2.3). μ_1 incorporates the effect of scatter from the square field size of side length, S (cm) on the value of the EAC. The parameter μ_2 represents the decrease in the EAC per unit depth. It was found that this parameterization reproduces the EAC values within 5 percent in most cases. In table 2.4 a summary of these parameters is shown for the materials used in this study.

Table 2.4: The parameters of equation 2.3 for the EAC of the materials used in this study.

Material	Energy (MV)	μ_0 (cm^{-1})	μ_1 ($cm^{-1/3}$)	μ_2 (cm^{-2})
Wax	6	0.052	0.173	0.00025
	8	0.047	0.233	0.00024
	15	0.045	0.362	0.00027
Aluminum	6	0.147	0.052	0.00074
	8	0.129	0.037	0.00056
	15	0.122	0.035	0.00053
Brass	6	0.411	0.105	0.00091
	8	0.373	0.020	0.00120
	15	0.371	0.005	0.00154
Copper	6	0.438	0.110	0.00156
	8	0.407	0.055	0.00122
	15	0.395	0.121	0.00097
Lead	6	0.659	0.088	0.00016
	8	0.607	0.045	0.00086
	15	0.615	0.105	0.00051

If the partial derivative with respect to d is applied to equation 2.3 it leads to:

$$\frac{\partial \mu_{eff}}{\partial d} = -\mu_2 \qquad (2.4)$$

This shows that the rate of change of the EAC per unit depth (cm) is given by the values of μ_2 in the right-most column of table 2.4. The transmitted dose D at depth z in water for a compensator with a thickness t, can be determined with equation 2.2:

$$D(z,t) = D(z,0)e^{-\mu_{eff}(z)t} \qquad (2.5)$$

The corresponding expression for the dose D at a certain reference depth z_{ref} would be:

$$D(z_{ref},t) = D(z_{ref},0)e^{-\mu_{eff}(z_{ref})t} \qquad (2.6)$$

The ratio of equation (2.5) and (2.6) yields:

$$\frac{D(z,t)}{D(z_{ref},t)} = \frac{D(z,0)}{D(z_{ref},0)} e^{-(\mu_{eff}(z)-\mu_{eff}(z_{ref}))t} \tag{2.7}$$

If equation (2.7) is expressed in terms of percentage depth doses, (2.7) becomes:

$$PDD(z,t) = PDD(z,0)e^{-\Delta\mu_{eff}(z)t} \tag{2.8}$$

The percentage change in terms of the fractional percentage depth dose can then be expressed as:

$$\frac{PDD(z,t)}{PDD(z,0)}(\%) = 100 * e^{-\Delta\mu_{eff}(z)t} \tag{2.9}$$

From equation (2.3), $\Delta\mu_{eff}(z)$ can be expressed as:

$$\Delta\mu_{eff}(z) = -\mu_2(z - z_{ref}) \tag{2.10}$$

If (2.10) is inserted into (2.9) the equation becomes:

$$\frac{PDD(z,t)}{PDD(z,0)}(\%) = 100 * e^{\mu_2(z-z_{ref})t} \tag{2.11}$$

The difference at any specific depth z, between the PDD under a compensator of thickness t, and the PDD of the open field, will be given by:

$$\Delta PDD(\%) = 100 * (e^{\mu_2(z-z_{ref})t} - 1) \tag{2.12}$$

The evaluation of equation (2.12) shows that the change in the percentage depth dose as a function of depth depends on the parameter μ_2. It, in turn, depends on the compensator material and the beam energy as shown in table 2.4. Figure 2.5 a – e shows a series of graphs for each compensator material and beam energy. In each graph the change in the percentage depth dose (delta PDD) as calculated with equation 2.12 was evaluated for a set of attenuator thicknesses, t, and a set of z – values for its own μ_2 value (table 2.4).

These graphs clearly show that the EAC determined at a single fixed depth should not be used over the whole range of depths for compensator thickness calculation purposes. It can lead to errors in the percentage dose that range between 3 percent for lead at 6 MV up to 30 percent for brass and copper. At thicknesses larger than 5 cm and depths larger than 10 cm the 5 percent error in the percentage dose will be exceeded. This is true for almost all the cases shown. For a treatment planning accuracy of at least 3 percent, the constraints would have to be made even stricter. On the basis of equation 2.12 it would be more accurate to incorporate the EAC variation with depth than to use only one value.

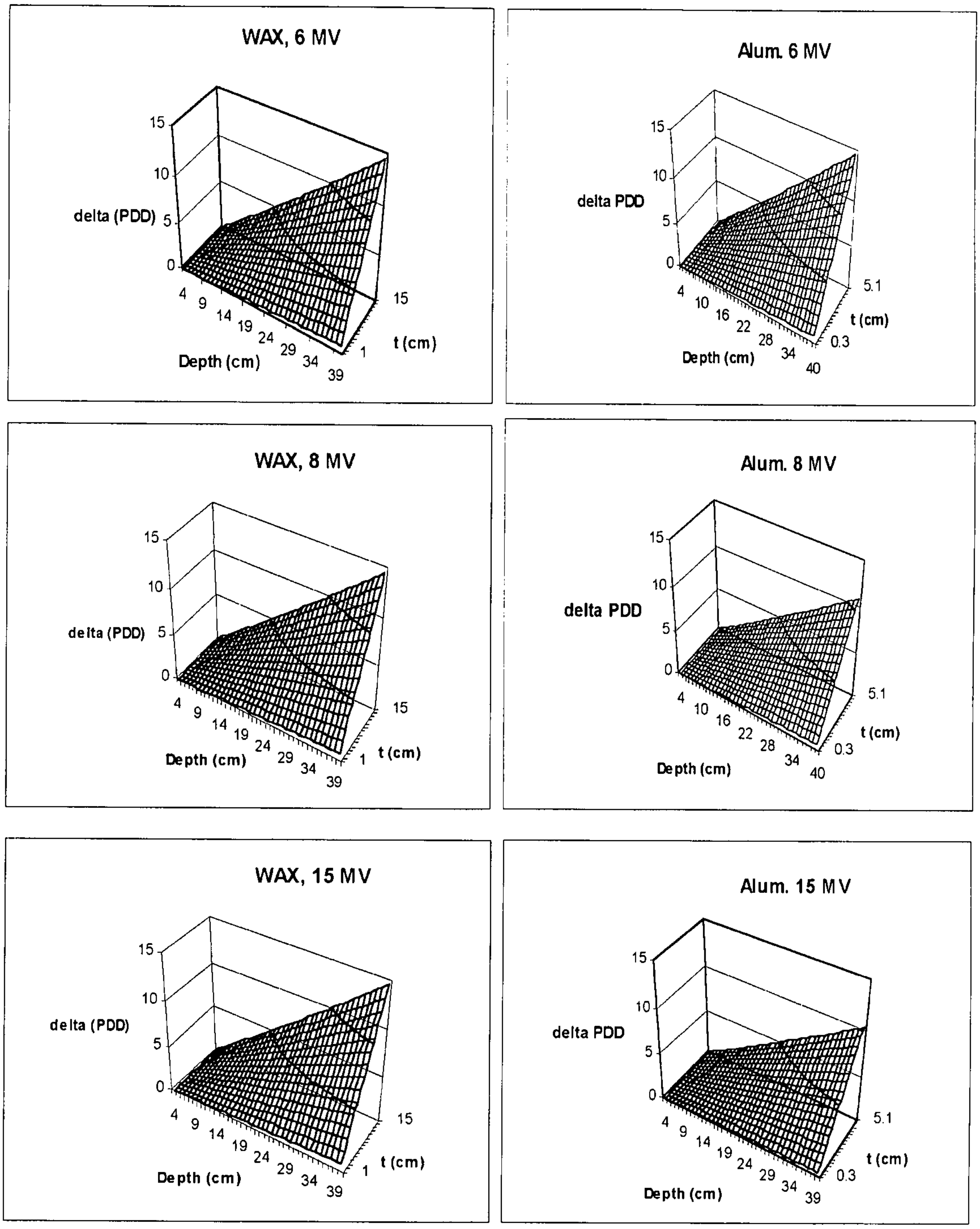

(a)

(b)

Figure 2.5 a and b. The change in the PDD as calculated with equation 2.12 for wax and aluminum over a range of thicknesses and depths. μ_2 was obtained from table 2.4 for each material and energy.

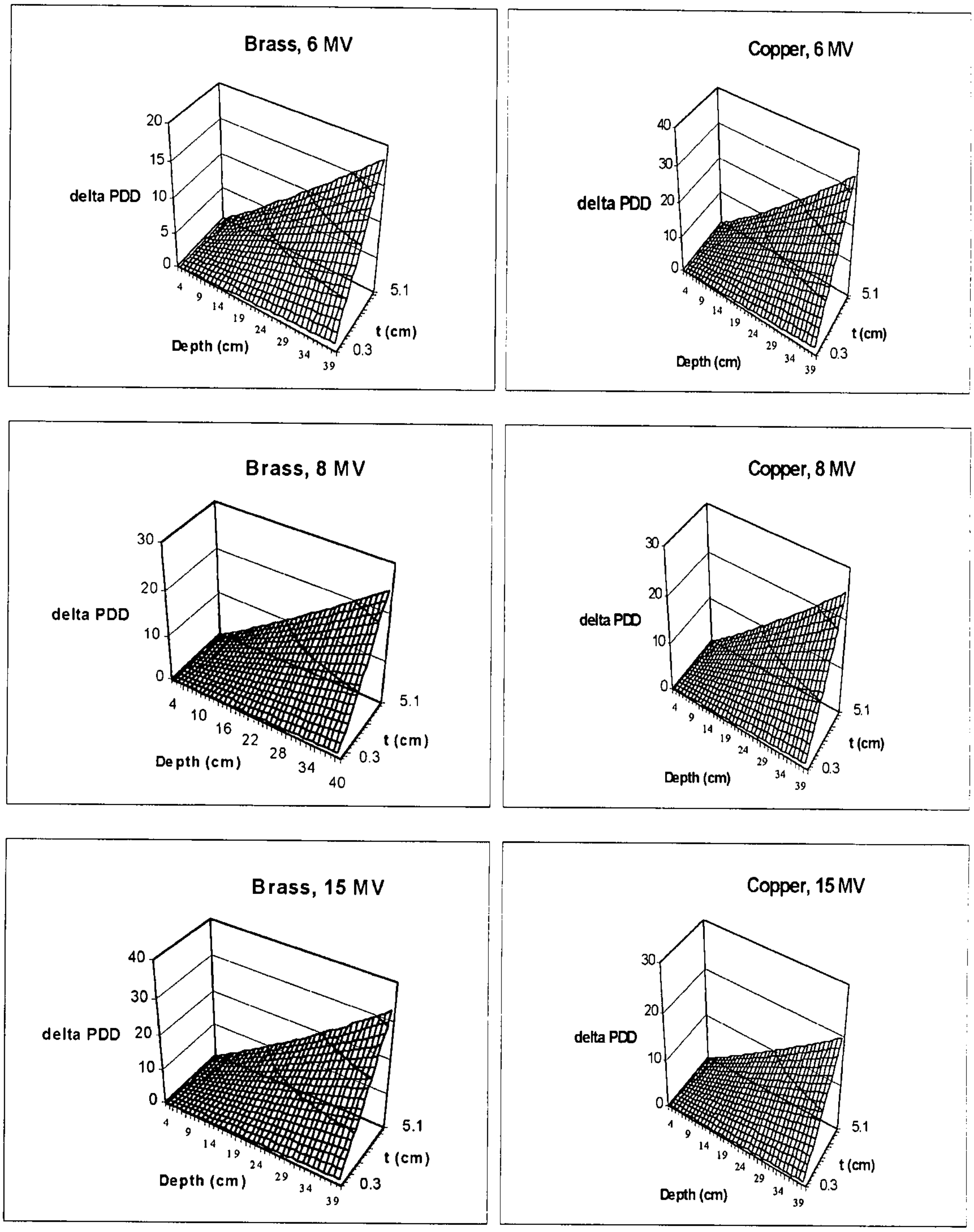

(c) (d)

Figure 2.5 c and d. The change in the PDD as calculated with equation 2.12 for brass and copper over a range of thicknesses and depths. μ_2 was obtained from table 2.4 for each material and energy.

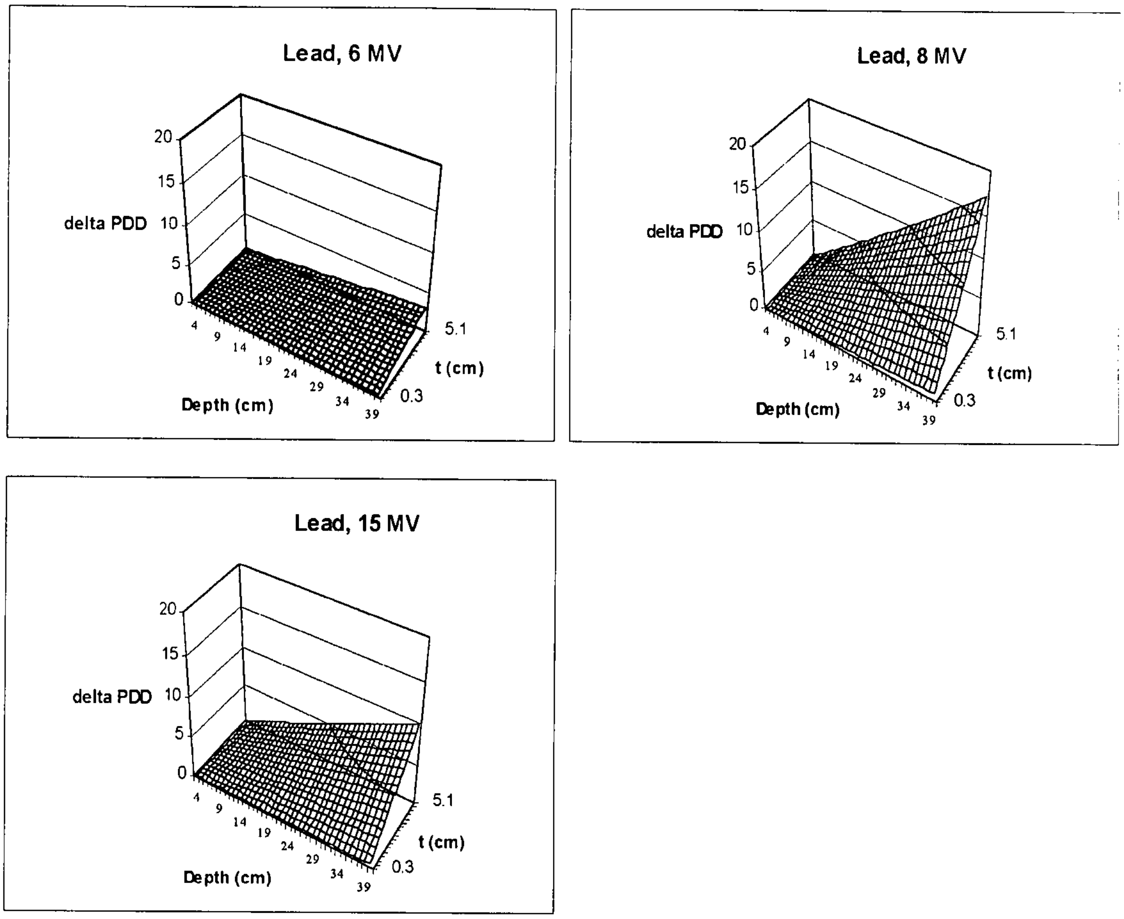

(e)

Figure 2.5 e. The change in the PDD as calculated with equation 2.12 for lead over a range of thicknesses and depths. μ_2 was obtained from table 2.4 for each energy.

The dependence of the EAC on beamlet field length S can also be analyzed. If the partial differential for the EAC with respect to field size in equation (2.3) is taken, the result is:

$$\frac{\partial \mu_{eff}}{\partial S} = -\frac{1}{3}\mu_0\mu_1 S^{\frac{-2}{3}} \qquad (2.13)$$

From equation (2.13) is seen that the rate of change in the EAC (labeled as μ_{eff}) with respect to the beamlet field length S is proportional to the product of μ_0 and μ_1.

Using equation (2.2), let the transmitted dose D as a function of depth z and absorber thickness t for a beamlet field length S be defined as:

$$D(z,t,S) = D(z,0,S)e^{-\mu_{eff}(z)t} \tag{2.14}$$

Insertion of (2.3) into (2.14) leads to:

$$D(z,t,S) = D(z,0,S)e^{-\left[\mu_0(1-\mu_1 S^{\frac{1}{3}})-\mu_2 z\right]t} \tag{2.15}$$

The transmitted dose of a reference field length S_{ref} would be

$$D(z,t,S_{ref}) = D(z,0,S_{ref})e^{-\left[\mu_0(1-\mu_1 S_{ref}^{\frac{1}{3}})-\mu_2 z\right]t} \tag{2.16}$$

The ratio of (2.15) and (2.16) is:

$$\frac{D(z,t,S)}{D(z,t,S_{ref})} = \frac{D(z,0,S)}{D(z,0,S_{ref})}e^{-\left[\mu_0\mu_1(S^{\frac{1}{3}}-S_{ref}^{\frac{1}{3}})\right]t} \tag{2.17}$$

In equation (2.17) the left side can be interpreted as an output factor for an attenuator or compensator (OF_c) since it is the ratio of the transmitted dose for field length S to that for a reference field length S_{ref}. The ratio on the right of (2.17) corresponds to the open beam dose ratio for a field length S to that for a field length S_{ref}. This can be interpreted as an output factor (OF_o) relative to S_{ref}. The quantity in the square brackets that form part of the exponent can be associated with $\Delta\mu_{eff}$ - the change in the EAC from field length S to the reference field length S_{ref}. Equation (2.17) can thus be written as:

$$\frac{OF_c}{OF_o} = e^{-\left[\mu_0\mu_1(S^{\frac{1}{3}}-S_{ref}^{\frac{1}{3}})\right]t} \tag{2.18}$$

In figure 2.6 a – e a set of plots of (OF_c/OF_o) are shown and is expressed as a percentage change relative to S_{ref} for a set of field lengths S and a range of thicknesses t. S_{ref} was chosen as 0.5 cm. Each graph corresponds to a compensator material at one beam energy. The thickness range for wax was set from 1 to 15 cm in 1 cm increments. For the other materials the thickness was set from 0.3 to 5.1 cm in increments of 0.3 cm.

Each plot of (OF_c/OF_o) was expressed in terms of the percentage change in its value for a field length S, relative to a beamlet with field length S_{ref}. Equation (2.18) relates the ratio of the transmitted dose to that for the open beams at two distinct beamlet sizes as a function of beamlet field length S. All graphs in figure 2.6 show that the output factor for the transmitted dose increases relative to that for the corresponding open beams. This implies that the output factor for an attenuated beam is larger than for the corresponding open beams at the relevant field sizes. In this case S_{ref} was chosen as the smallest beamlet field length. According to the evaluation of equation (2.18) the dose ratio between S and S_{ref} is higher for the transmitted beam since, apart from other factors, the scatter from the attenuator enhances the dose which is not present for the open beam case. This quantity varied from about 2 percent for aluminum to 30 percent for lead.

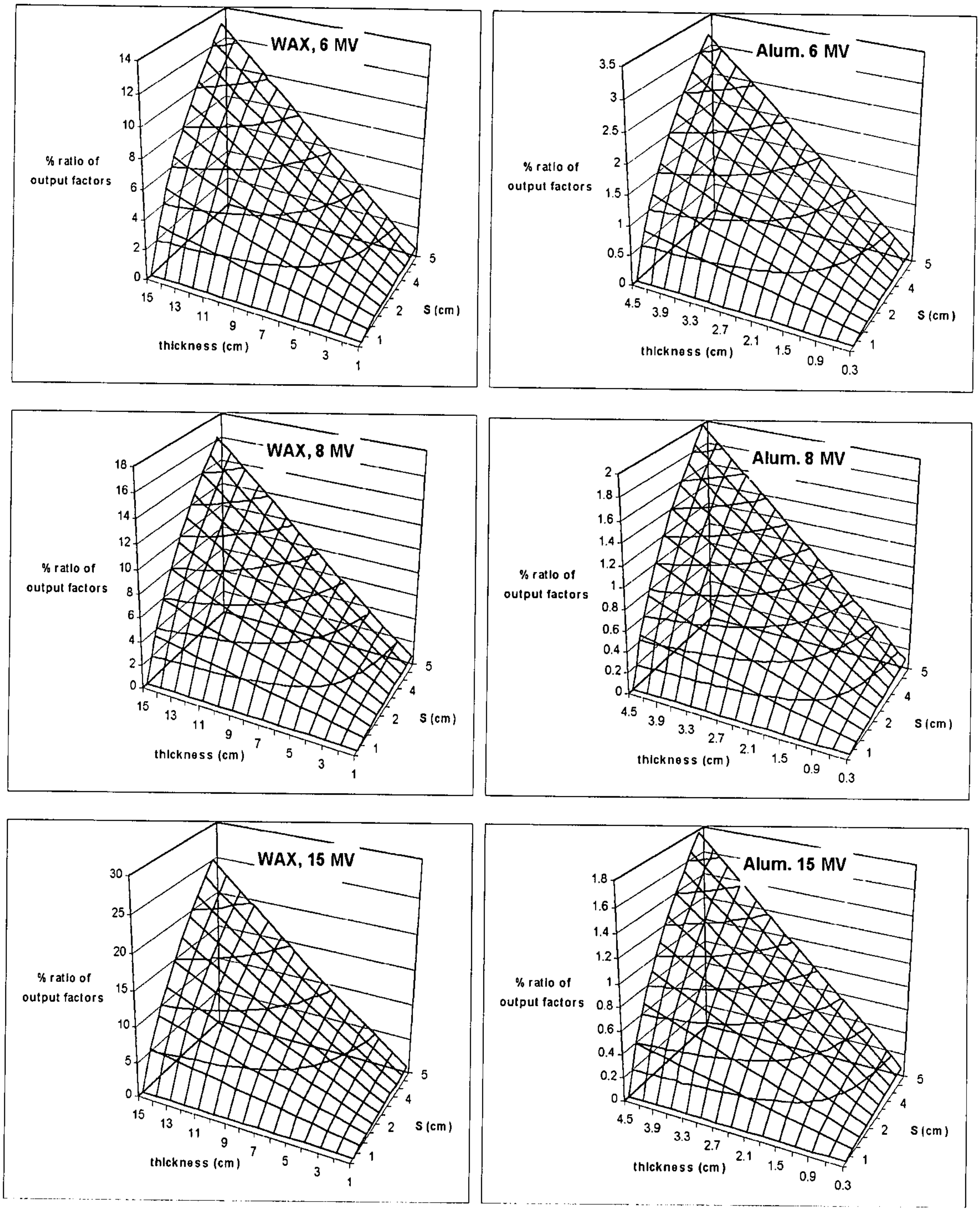

(a) (b)

Figure 2.6 a and b. Evaluation of equation 2.18 (expressed as a percentage change) for a fixed reference field (S_{ref} = 0.5 cm). The parameters μ_0 and μ_1 corresponding to wax and aluminum were obtained from table 2.4 for the relevant energies.

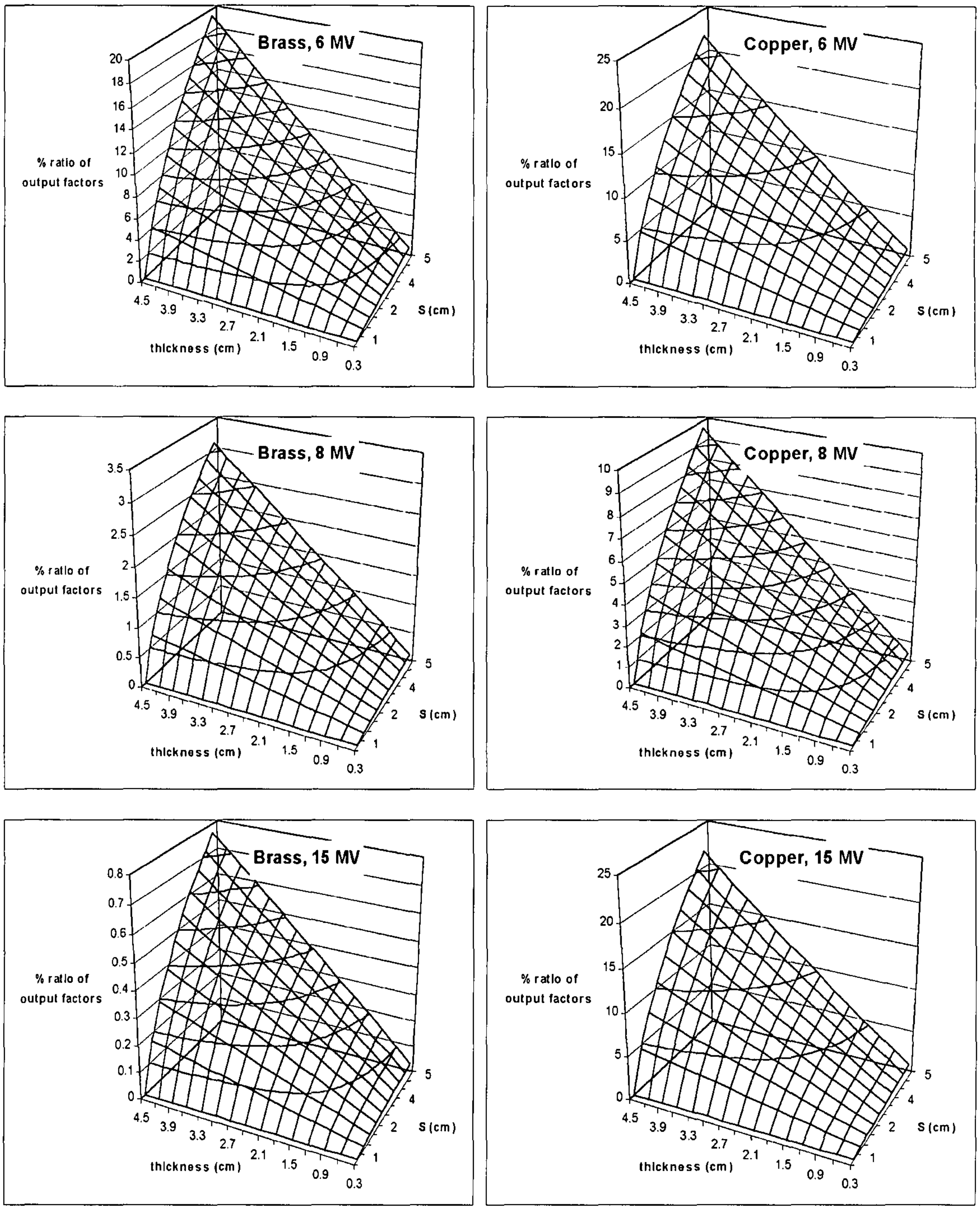

(c)

(d)

Figure 2.6 c and d. Evaluation of equation 2.18 (expressed as a percentage change) for a fixed reference field (S_{ref} = 0.5 cm). The parameters μ_0 and μ_1 corresponding to brass and copper were obtained from table 2.4 for the relevant energies.

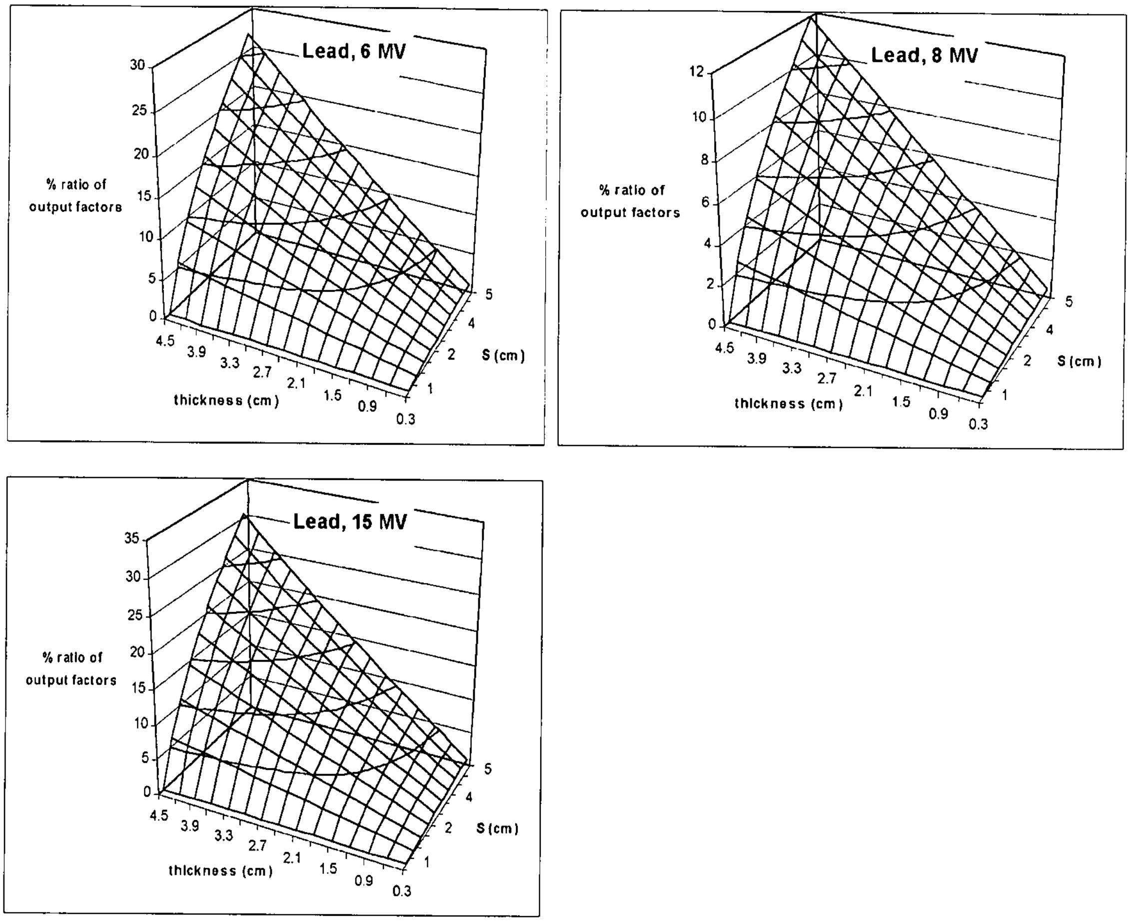

(e)

Figure 2.6 e. Evaluation of equation 2.18 (expressed as a percentage change) for a fixed reference field ($S_{ref} = 0.5$ cm). The parameters μ_0 and μ_1 corresponding to lead were obtained from table 2.4 for the relevant energies.

The parameters in table 2.4 was determined from the EACs in table 2.3 which, in turn, was evaluated at a depth of 4 cm in water. Qualitatively, the data in figure 2.6 suggests that the ratio of the output factors is high for wax, decrease for aluminum and increase from brass to copper to lead. Scatter and beam hardening from an attenuator can accomplish dose enhancement in a water phantom. Based on the data in figure 2.6 the scatter dose enhancement for wax is higher than for aluminum, probably due to relatively more scattered radiation that reach the water phantom. For brass, copper and lead, their respective electron densities increase, as well as their physical densities. This causes more scatter events per unit thickness as well as more efficient self-absorption of primary and scattered radiation. The result is an increase in beam quality that enhances the dose in the water phantom that causes an increase in the transmitted radiation (compensator) output factor, OF_c when compared to the open beam output factor, OF_o.

2.3.2 Effect of voxel size and compensator retractal distance

At this point a discussion of the effect of the voxel size used for the MC depth dose calculation on the accuracy of the results is in order. Tests have indicated that the depth dose data generated using voxels with the same lateral dimensions in the x and y directions, but reduced to 0.5 cm in the z direction gave absolute depth dose results that differed less than one percent compared to the original results with a voxel dimension of 1.0 cm in the z direction. These differences are related to the change in variance of the comparative depth dose data. The largest differences were found near the phantom (water) surface but the EAC results are based on smoothed depth dose data for depths greater than 4 cm. It is therefore not expected that the smaller voxel would influence the values of the effective attenuation coefficients appreciably. In this study all EAC data were derived for an absorber-to-skin-distance (ASD) or retractal distance of 33 cm (see figure 2.1). No investigation into the variation of these coefficients with retracting distance was made. The variation of the EAC as a function of retracting distance is well known[11,21].

2.3.3 Effect of flattening filter in real situations

The EACs were derived on the central axis (CAX). The values of these coefficients would change radically from the CAX in a real beam, since there is a change in the spectral properties of the beam partly due to the shape of the flattening filter and the angular distribution of bremstralung photons emerging from the target.[30, 31] Larson *et al.* [32] approximated the radial dependence of the effective attenuation coefficient for a lead filter with a linear function, $\mu(r) = 0.0539 + 0.0005(cm^{-1})$, for a 4MV beam. Bjärngard *et al.* [33] measured attenuation factors in water and found a quadratic dependence of the effective attenuation coefficient as a function of radius in water of the form: $\mu(r) = 0.0473(1 + 0.00033r^2)$. This relationship was found for a 6 MV open beam generated by a Philips SL75-5 linac. Thomas *et al.* [34, 35] measured the radial variation of beam quality for 8 MV x-rays in water for a tungsten alloy filter. They found a linear relationship for the effective attenuation coefficient expressed as a function of the azimuthal angle ϕ, between the CAX and the radial position on the surface of the water phantom. Their equation for the effective attenuation coefficient was $\mu(\phi) = 0.037 + 0.020(\varphi)$.

Apart from field size and to a lesser extent, depth dependencies, the EAC depends significantly on spectral changes introduced off-axis by flattening filters.

Others [16, 17] have also incorporated an attenuator thickness, t, dependence in their EAC parameterization equations that is absent from ours (equation 2.3), but used larger field sizes. Our study indicated an exponential decline in the absorbed dose as a function of absorber thickness over the field size range used. Larger fields from linacs would introduce radial spectral changes would that enhance the CAX dose and thus decrease the EAC. This could alter the simple exponential relationship found between dose and attenuator thickness (e.g. $T(x) = \exp(-\mu x)$, equation 2) to an expression $T(x) = \exp(-\mu x(1 - \eta x))$: the type used by Bjärngard et. al. [33] In this study scatter effects from compensator materials are studied and the sources used in MC simulations are of uniform intensity, with invariant energy spectra over the total field, and are non-divergent. Thus the derived EACs would apply for all fields used in this study.

2.4 Application of EACs in this study

The EAC values in this study were derived for small beamlets. This is in anticipation of their use in the design of compensators from a set of beamlet weights derived from an inverse planning system. The compensator is built up from elements corresponding to the individual beamlets. In regions where the dose gradient is large the elements used will have small dimensions. Each element corresponds to an identical beamlet size if it is assumed the beam is parallel. The usual practice when compensators are manufactured is to use broad beam EACs to try to account for compensator induced scatter. It would be incorrect to use the EACs derived here in this manner to manufacture a compensator without taking scatter effects also into account. This is the focus of the next Chapter where the evolution of pencil beams (PBs), which have traversed compensator materials of various thicknesses, is modeled.

2.5 Conclusion

In this study EACs were derived for three different x ray beam energies and a range of beamlet sizes. It was found that the EAC values decrease as a function of depth and x-ray beam energy and can be conveniently parameterized. Analysis of the percentage dose change with depth indicates that the depth dependency of the EAC should be taken into account. It was also found that the compensator output factor (OF_c) is higher than for the corresponding open fields (OF_0) and that it reaches a local minimum for aluminum and increases further as the physical density of the compensator material increases e.g. from brass to copper to lead. These EACs can also be used for compensator manufacturing since it takes beam hardening and the scatter properties of x rays in the beamlets directly into account and is based on absorbed dose values, rather than linear attenuation coefficients, which are based on the conversion of fluence to dose.

The results in this Chapter were derived for data that have been collected on the CAX in a DOSXYZ water phantom for a limited range of beamlet sizes. In practice, compensators cover fields that are larger than that of typical beamlet dimensions. If the EACs as derived in this Chapter were used in compensator manufacture, then this would only partially account for scatter effects in larger beams. If a compensator is approximated by a set of beamlets with different field sizes, then these EACs can be used to approximate the shape of the compensator, where each EAC corresponds to a certain beamlet size. This would then be a starting point for the construction of the compensator.

The use of an EAC is limited to the scaling (weighting) of the primary dose component that is transmitted through a compensator or other beam attenuator. It cannot account for compensator-induced scattered radiation that enhances the dose at the point of interest nor can it be used to determine the scatter characteristics of different compensator materials. In this study (see following chapters) a PB based superposition method was used to construct a compensator. In Chapter 3 it is shown how a PB can be modeled to take compensator scatter and beam hardening into account.

2.6 References

[1] F. Ellis, A. Feldman, and R. Oliver, " A compensator for variations in tissue thickness for high energy beams.", Br. J. Radiol. **32**, 421 (1959).

[2] F.M. Khan, V.C. Moore and D.J. Burns, " The Construction of compensators for Cobalt Teletherapy.", Radiology **96**, 187 - 192 (1970).

[3] P.M.K. Leung, J. Van Dyk, and J. Robins, " A method of large irregular field compensation.", B. J. Radiol. **47**, 805 – 810 (1974).

[4] D.M. Robinson and J.W. Scrimger, "Optimized tissue compensators", Med. Phys. **17**, 391 – 396 (1990)

[5] E. El-Khatib, E.B. Podgorsak and C. Pla, "Calculation of dose in homogeneous phantoms for partially attenuated photon beams", Med. Phys. **13**, 928 – 935 (1986).

[6] J.E. Marrs, A.R. Hounsell and J.M. Wilkinson, "The efficacy of lead shielding in megavoltage radiotherapy", Br.J.Radiol. **66**, 140 – 144 (1993).

[7] E. El-Khatib, E.B. Podgorsak and C. Pla, 'Calculation of dose in homogeneous phantoms for partially attenuated photon beams', Med. Phys. **15**, 145 – 150 (1988).

[8] E. Papiez and G. Froese, "The calculation of transmission through a photon beam attenuator using sector integration", Med. Phys. **17**, 281 – 286 (1990).

[9] M.E. Castellanos and J.C. Rosenwald, "Evaluation of the scatter field for high-energy photon beam attenuators", Phys. Med. Biol. **43**, 277 –290 (1998).

[10] S.J. Thomas and G. Bruce, "Skin dose near compensating filters in radiotherapy", Phys. Med. Biol. **33**, 703 – 710 (1988).

[11] P-H. Huang and B.E. Bjärngard, "Scattered photons produced by beam-modifying filters", Med. Phys. **13**, 57 - 63 (1986).

[12] J. Van Dyk, "Broad beam attenuation of cobalt-60 gamma rays and 6-, 18-, and 25 MV x rays by lead", Med.Phys. **13**, 105 – 110 (1986).

[13] A. Ahnesjö, L. Weber and P. Nilsson, "Modeling transmission and scatter for photon beam attenuators", Med. Phys. **22**, 1711 –1721 (1995).

[14] F.R. Bagne, N. Samsami, S.W. Hoke and D.G. Bronn, "A study of effective attenuation coefficient for calculating tissue compensator thickness", Med. Phys. **17**, 117 - 121 (1990).

[15] E.C. McCullough, J. Gortney and C.R. Blackwell, "A depth dependance determination of the wedge transmission factor for 4 – 10 MV photon beams", Med. Phys. **15**, 621 – 626 (1988).

[16] A.L. Boyer, " Compensating filters for high energy x rays.", Med. Phys. **9**, 429 – 433 (1988).

[17] K.J. Weeks, B.A. Fraass, and K.M. Hutchins, " Gypsum mixtures for compensator construction.", Med. Phys. **15**, 410 – 414 (1988).

[18] V.R. Arora and K.J. Weeks, " Characterization of gypsum attenuators for radiotherapy dose modification.", Med. Phys. **21**, 77 – 81 (1994).

[19] C-M. Ma, P. Reckwerdt, M. Holmes, D.W.O. Rogers and B. Geiser, 'DOSXYZ Users Manual', National Research Council of Canada (NRC, Ottowa), (1995).

[20] B.E. Bjärngard, J.-S. Tsai, and R.K. Rice, "Attenuation in Very Narrow Photon Beams", Radiation Research **118**, 195 – 200 (1989).

[21] W. Sewchand, N. Bautro and R.M. Scott, "Basic data on tissue-equivalent compensators for 4-MV X-rays", Int. J. Radiat. Oncol. Biol. Phys. **6**, 327 – 332 (1980).

[22] K.P. Mandal, D.H. Baxter and P. Ray, "Thin lead sheets as tissue compensators for larger field irradiation", Int. J. Radiat. Oncol. Biol. Phys. **6**, 513 – 517 (1980).

[23] A. Djordevich, D.J. Bonham, E.M.A. Hussein, J.W. Andrew and M.E. Hale, "Optimal design of radiation compensators", Med. Phys. **17**, 397 – 404 (1990).

[24] J.S. Li, T. Pawlicki, J.Deng, S.B. Jiang, E. Mok and C-M Ma, "Validation of a Monte Carlo dose calculation tool for radiotherapy treatment planning", Phys. Med. Biol. **45**, 2969 – 2985 (2000).

[25] S.X. Chang, T.J. Cullip and K. M. Deschesne, "Intensity modulation delivery techniques: 'Step & shoot' MLC auto-sequence versus the use of a modulator", Med. Phys. **27**, 948 – 959 (2000).

[26] W.R. Nelson, H. Hirayama and D.W.O. Rogers, The EGS4 Code System SLAC-Report-265, Stanford Linear Accelerator Center (1985).

[27] D.W.O. Rogers, B.A. Faddegon, G.X. Ding, C-M. Ma, J. We and T.R. Mackie, "BEAM: A Monte Carlo code to simulate radiotherapy treatment units.", Med. Phys. **22**, 503 – 525 (1995).

[28] C.-M. Ma and D.W.O. Rogers, ‘BEAMDP Users Manual’, National Research Council of Canada. Report PIRS-0509B (NRC, Ottawa), (1995).

[29] J.H. Hubbell and S.M. Seltzer, ‘Tables of X-ray Mass Attenuation Coefficients and Mass Energy-Absorption Coefficients 1 keV to 20 MeV for Elements Z = 1 to 92 and 48 Additional Substances of Dosimetric Interest.’ NISTIR 5632 (1995).

[30] W.H. Hanson, and L.W. Berkley, “Off-axis beam quality change in linear accelerator x-ray beams.”, Med. Phys. **7**, 145 – 146 (1980).

[31] R. Mohan, C. Chui, and L. Lidofsky, “Energy and angular distributions from medical linear accelerators.’, Med. Phys. **12**, 592 – 597 (1985).

[32] R.D. Larsen, L.H. Brown, and B.E. Bjärngard, “ Calculations for beam-flattening filters for high-energy x-ray machines.”, Med. Phys. **5**, 215 – 220 (1978).

[33] B.E. Bjärngard and H. Shackford, “ Attenuation in high-energy x-ray beams.”, Med. Phys. **21**, 1069 – 1073 (1994).

[34] S.J. Thomas and R.L. Thomas, “ A beam generation algorithm for linear accelerators with independent collimators.”, Phys. Med. Biol. **35**, 325 – 332 (1990).

[35] S.J. Thomas, “ A computer-calculated tissue compensator system.”, Br.J.Radiol. **58**, 665 – 668 (1993).

[36] F.C.P. du Plessis and C.A. Willemse,’ Monte Carlo calculation of effective attenuation coefficients for various compensator materials’, Med. Phys. **30**, 2537 – 2544 (2003).

CHAPTER 3

Modeling scatter and beam hardening for a pencil beam after traversing a semi-infinite slab of compensator material

3 Preface

In Chapter 2 effective attenuation coefficients (EAC) were calculated using Monte Carlo methods. Their properties were analyzed and their values could be conveniently parameterized. If a compensator field is decomposed into a set of beamlets, then the derived EACs can only account for the scatter properties for each beamlet size. Their contribution in terms of scatter at other parts of the field is not accounted for at the point of interest. In practice a broad beam EAC is used for this purpose, where each beamlet is weighted by this EAC. This Chapter focuses on how to include scatter and beam hardening from a pencil beam model so that the derived EACs can be used to give a reasonable first approximation of the compensator shape.

3.1 Introduction

Pencil beam (PB) based dose calculation algorithms can be used to calculate dose distributions for IMRT purposes. Intensity modulation can be achieved using multileaf collimators (MLC), dynamic jaws [1], wedges, masks [2] or compensators. Beams are usually decomposed into a set of beamlets to correspond with a MLC setting or compensator shape. When dose optimization is performed all the beamlets in a treatment beam are initially considered to be open and of uniform intensity. Changing the weight of a beamlet implies that the dose contribution of that part of the field is altered. Thus in practice that part of the beam should be shielded for part of the radiation time using a MLC or partially attenuated using a compensator/modulator over the whole beam-on time. If the MLC is considered as a device that absorbs the beam to a large extent i.e. relatively low transmission [3, 4], then beamlet weighting can be regarded as a partial contribution of the dose delivered by the open beamlet in terms of the total treatment time, although transmission corrections are crucial for relative dose calculations.[5] In the case of the compensator/modulator the beamlet dose modulation is achieved by attenuating the energy fluence so that the dose contribution is effectively weighted. This inherently introduces spectral changes in the beamlet that alters its in-phantom scatter and beam penetration properties. It also produces a compensator-scatter background, [6] since a compensator is designed to transmit radiation and thus would produce significant scattered radiation.

For treatment optimization purposes the beamlets should be adapted to take beam modulator scatter into account. Beamlets can be modeled using MC methods [7] or pencil beams [8 - 13] or a combination of both methods in optimized treatment planning.[14] In this study the evolution of 6, 8 and 15 MV poly-energetic pencil beams (PBs) was investigated after having traversed sets of attenuators with different thicknesses. The attenuators consisted of wax, aluminum, brass, copper, and lead. When 3D PB dose calculations are performed the energy fluence at the point of entry in the patient model must be known. Photons can originate from various components in the accelerator, such as scatter from the jaws, beam modulators and flattening filter [15 - 17] and leakage through the collimators.[18] Some authors have treated the problem of scatter and spectral changes in the fluence by analytical models [15 - 17] that correct for the primary and scatter fractions of the energy fluence emanating from the flattening filter, collimator and a modulator e.g. a wedge or compensator. Others have used a Compton first-scatter based method to calculate the scatter fluence from a beam-modifying absorber [19], approximations for second order scatter [20] and semi-empirical methods that include sector integration.[21 - 23] Weber *et al.* [24] have applied an analytical method [15] in conjunction with a k_μ -matrix to account for off-axis beam changing characteristics and beam modulator penetration properties mainly due to spectral changes in the beam leading to more lower energy components in the poly-energetic photon beam. In the current study an empirical method is presented on how a PB can be modified to include the beam hardening and scatter effects of the above-mentioned absorber materials. The primary objective is to attempt to model compensator-induced scatter and beam hardening changes in a PB model. Scatter from the other components of an accelerator [25] is included in the energy spectra for the pencil beams used in this study and thus only the compensator material thickness was varied.

3.2 Methods

The EGSnrc [26] based DOSRZnrc MC code was used to derive sets of poly energetic PBs for energies of 6, 8 and 15 MV. For each energy, PBs were derived for the pencil source of photons traversing thicknesses t = 0, 1.0, 2.0, 3.0, and 5.0 cm of a semi-infinite compensator material slab. The attenuators consisted of wax, aluminum, brass, copper, and lead. PBs derived with no absorber in its path will be referred to as open PBs. The DOSRZnrc code was chosen since pencil beams display cylindrical symmetry in homogeneous phantoms, such as water, allowing one to take advantage of the variance reduction possible when dose is scored in annuli. The spectral characteristics of these beams were based on the Philips SL74/14N, SL75-5 and SL-25 linac series. The spectral data were obtained by using the EGS4 [27] based BEAM [28] MC simulation code to model the accelerator. The output beam was scored in a phase space file (PSF) and was analyzed with the BEAMDP [29] code. The PSF contained all the photons emerging from the accelerator model i.e. primary as well as scattered photons from the radiation head. The energy spectrum included all the photons in the PSF and was subsequently used as the energy spectrum for the pencil beam source, which was directed from the front (parallel to the Z-direction), perpendicular to the XY plane of a modeled water phantom, with incidence at the origin, using the DOSRZnrc code.

The various scatter components in the accelerator was not modeled in great detail, since the focus of this study was to evaluate the evolution of PB dose deposition after penetrating a beam modulator. The dimensions of the cylindrical water phantom were 18.4 cm radially with a height of 40 cm. It was subdivided into 46 annuli each with a thickness of 0.4 cm. In the z-direction it consisted of 20 slabs with a thickness of 0.20 cm followed by 36 slabs, each of a thickness of 1.0 cm.

The set of pencil beams was derived using 200 million histories for each with an ECUT value of 0.700 MeV and a PCUT value of 0.010 MeV. Each pencil beam dose distribution was normalized to its own maximum dose on the PB axis.

To study the effect of absorbers on the PB dose distributions a model was constructed based on the enhancement of the open PB relative dose in the radial and depth dimensions due to scatter and beam hardening caused by the absorbers. This model enables one to account for the effect of an absorber by modifying the dose profile of an open PB at any arbitrary depth and radial distance in the water phantom.

The PB model was first validated by comparing the modified open PB relative dose profiles with MC derived profiles for attenuated pencil beams. As a final validation, percentage depth dose curves calculated with the open, modified open and attenuated PBs were compared.

3.3 Results and Discussion

The DOSXYZ code can be used to calculate a PB in cartesian coordinates, which are more convenient for 3D dose modeling since CT-based patient models are constructed in cartesian coordinates.[30] Pencil beams can also be determined from basic data.[31] For the purpose of this study PBs were generated using the cylindrical geometry of the DOSRZnrc MC code since it allows one to achieve variance reduction by scoring the particles in annuli rather than in the much smaller rectilinear voxels in cartesian coordinates. It also allows the PB (energy fraction deposited per unit mass) to be described accurately by using a well established analytical equation:[16, 18]

$$P_o(r,z) = \frac{A(z)\exp(-B(z)r)}{r} + \frac{C(z)\exp(-D(z)r)}{r} \qquad 3.1$$

where A(z) to D(z) are the fitting parameters at each depth (z) in the phantom. The second term can be regarded as the scatter component and the first term is assumed to be the primary energy imparted although the degree of precision might not be high.[18] Because we were only concerned with modeling the change in the relative dose distributions caused by the introduction of absorbers, no attempt was made to fit equation 3.1 to the open PBs, and thus to obtain the fitting parameters A - D.

Due to the finite size of the annuli and the large radial dose gradient near the PB axis, effective radii were assigned to the annuli using the formalism of Wang *et al.*[32] They used the formula:

$$r_n = \left[(n+0.5) + \frac{1}{12(n+0.5)} \right] \Delta r \qquad 3.2$$

where n is the annulus index with values n = (0, 1, 2, ..., n) and Δr is the annulus width. The cross section of the incident x ray pencil beam coincided with the cross section of the central annulus since it leads to the best accuracy in the parameterization when the effective radii according to equation 3.2 is used. For index n = 0 the radius would correspond to 0.66 Δr instead of the value 0.5 Δr that defines the geometric center of the first annulus.

In this study the depth in the EGSnrc water phantom is defined as z, and the attenuator thickness as t.

3.3.1 Relative pencil beam dose profiles vs. compensator thickness

Figure 3.1, left column, shows a set of normalized PB profiles for 6 MV, after each one has traversed different thicknesses of the absorber material indicated. *Each PB dose profile was normalized to its own dose maximum found along the PB central axis.* It will be hereafter referred to as the relative dose and indicated as $P_{t,med}^{(n)}(r,z)$ with t and med indicating the thickness and material of the absorber and (n) indicating that it is normalized. The unnormalized dose will be indicated as $P_{t,med}$ and is related to $P_{t,med}^{(n)}$ through: $P_{t,med}^{(n)} = \frac{P_{t,med}}{\left(P_{t,med}\right)_{\max}}$

where $\left(P_{t,med}\right)_{\max}$ indicates the maximum dose on the PB central axis.

The profiles in figure 3.1 are for a depth of 10 cm in the EGSnrc water phantom. Figures 3.2 and 3.3 show similar data calculated for 8 and 15 MV beam energies. At each energy the individually normalized dose profiles for different thicknesses t (left column in figures 3.1, 3.2 and 3.3) diverge from each other as a function of radial distance. This can be understood from the following: The role of an ideal compensator material is to absorb a fraction of the beam. For a real compensator in narrow beam geometry and scatter free conditions the intensity of the beam should decline exponentially at the measuring point on the CAX. The photons in the beam traversing a real compensator are a) either absorbed e.g. in photoelectric or pair production events or b) scattered coherently and incoherently. For the photon energies used here the incoherent (Compton) scatter process would dominate. A significant number of photons would be scattered out of the incoming PB to deposit/transfer their energy at off-axis regions in a phantom. Compared to an unattenuated (open) PB, the relative scattered dose would be enhanced when the PB is partially absorbed.

The right hand columns of figures 3.1, 3.2 and 3.3 show plots of $P_{t,med}^{(n)}$ as a function of the absorber thickness, t, for chosen radial positions of 1, 5, 10, 15 and 18 cm. The data is shown on a semi-logarithmic scale to better resolve the different plots on the same graph. On each plot is shown a number which represents the correlation coefficient, R^2. From these values it is clear that there exists an approximate linear relation between $P_{t,med}^{(n)}$ and t, although on the semi logarithmic scale the lines appear curved.

The data are presented in terms of relative dose in order to see more clearly how the PB profiles change when it traverses a material of known thickness. In principle a single unattenuated PB could then be adjusted to account for its penetration through a material of known thickness. This principle could then be applied very conveniently to model the dose under an arbitrary compensator of known composition and thickness. There is no need to generate a large number of PBs, using MC methods, for every conceivable thickness of the compensator material in order to include beam hardening and scatter. This linear relationship between relative scattered dose vs. compensator thickness was found to apply to all energies and materials used in this study, ranging from wax with the lowest density up to lead with most probably the highest density compensator that can be manufactured.

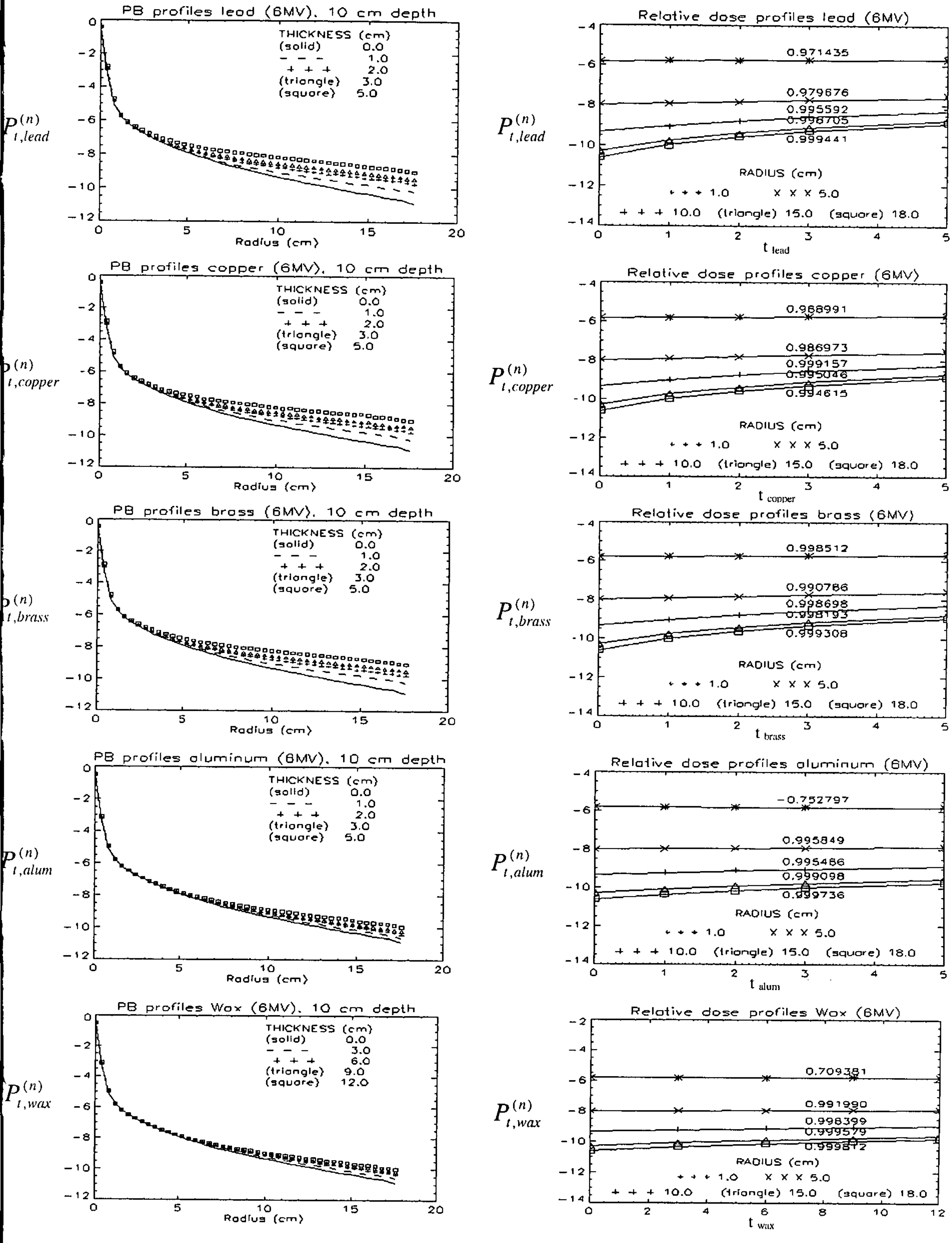

Figure 3.1. Left: A set of 6 MV PB dose profiles in the EGSnrc water phantom after traversing different thicknesses of compensator materials (0, 0.5, 1.0, 2.0, 3.0 and 5.0 cm). Right: relative dose vs. absorber thickness at radii of 1, 5, 10, 15 and 18 cm.

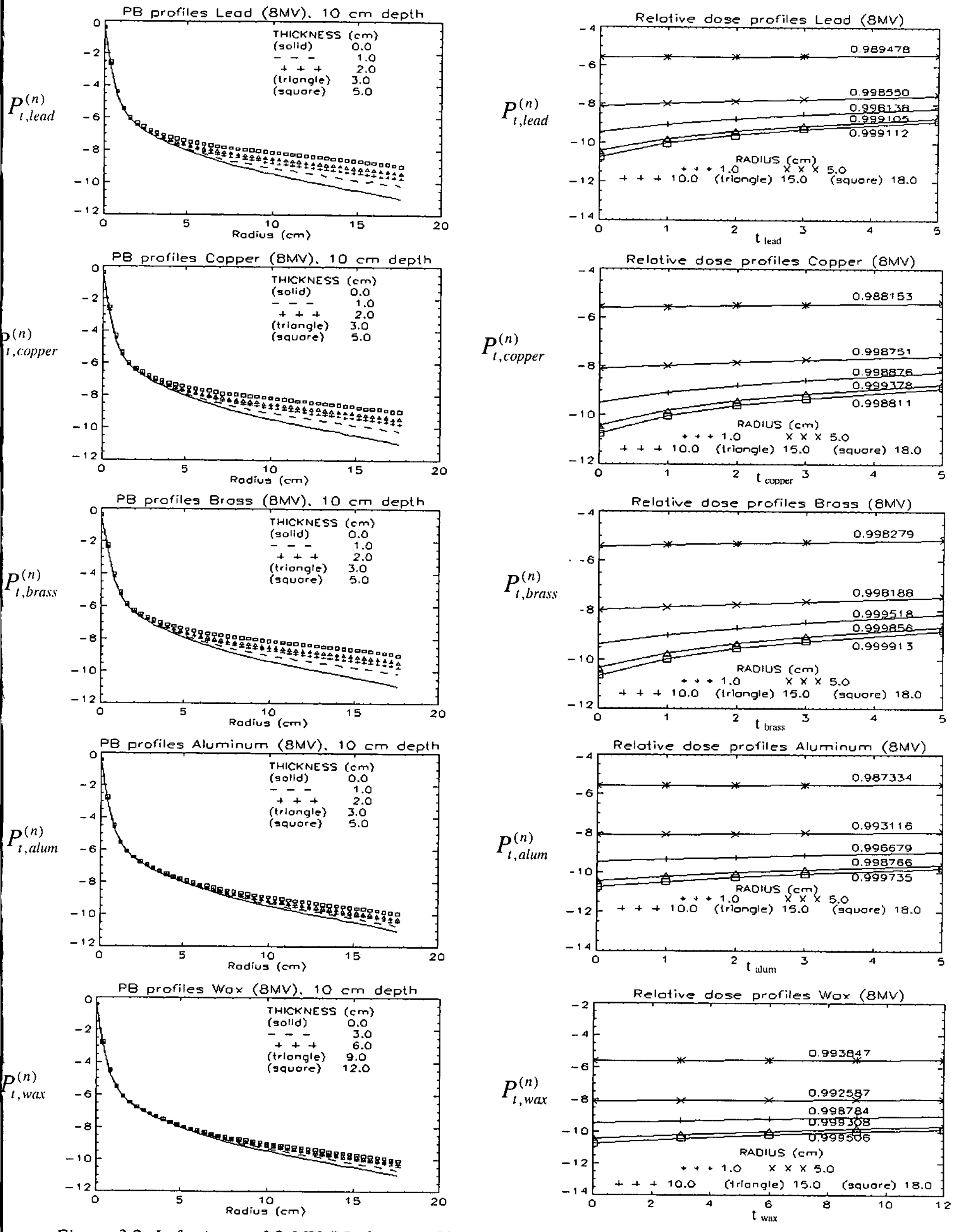

Figure 3.2. Left: A set of 8 MV PB dose profiles in the EGSnrc water phantom after traversing different thicknesses of compensator materials (0, 0.5, 1.0, 2.0, 3.0 and 5.0 cm). Right: relative dose vs. absorber thickness at radii of 1, 5, 10, 15 and 18 cm.

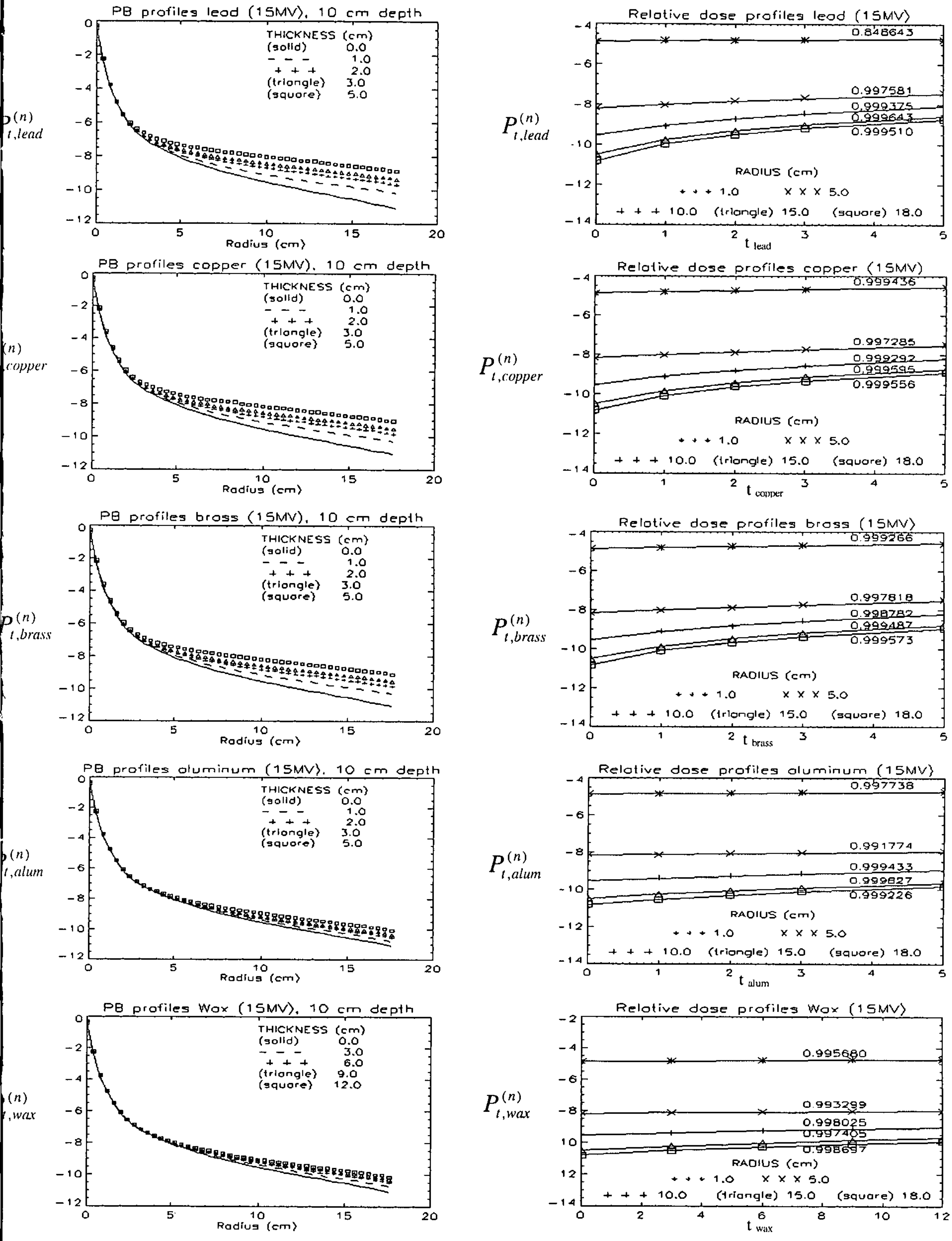

Figure 3.3. Left: A set of 6 MV PB dose profiles in the EGSnrc water phantom after traversing different thicknesses of compensator materials (0, 0.5, 1.0, 2.0, 3.0 and 5.0 cm). Right: relative dose vs. absorber thickness at radii of 1, 5, 10, 15 and 18 cm.

The physical and electron density range of materials (see table 2.2, Chapter 2) are such that it is most probable that all compensator materials would exhibit such a linear relation between relative scatter and absorber thickness, at least over the beam energies used in this study.

A note on fluence profiles

For the beam energies under consideration, the absorbed dose would be strongly related to the photon fluence. In figure 3.4 the relative photon fluence from an 8 MV photon beam is shown for the photons traversing a set of brass slabs each having a thickness (t) of 1.0, 3.0 and 5.0 cm when a PB is traversing it. This relative fluence is at the top plane of the EGSnrc cylindrical water phantom.

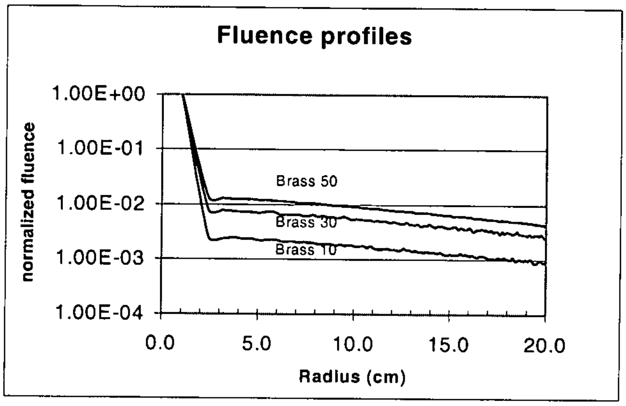

Figure 3.4. A set of normalized fluence profiles shown for an 8 MV PB in the plane 33 cm below infinite brass slabs of thickness 1.0, 3.0 and 5.0 cm. This planar distance corresponds to that of the surface of the EGSnrc water phantom. Normalization values taken on the beam axis. (Thickness values in the figure are in mm units).

Figure 3.4 shows the relative off-axis fluence for an increase in the thickness of the brass absorber. The normalization values were taken in the central annulus, which explains why the scatter component for thicker absorbers appears to be higher. In a region located at an off-axis position (r), the relative number of scattered photons reaching it would increase as the absorber thickness (t) increases. The increase in the fluence (as seen as increased dose in figures 3.1 – 3.3) would manifest itself into a relative increase in the off-axis dose.

The data in figure 3.4 were obtained from a set of BEAM (EGS4) MC simulations to collect the respective phase-space files. The BEAMDP code was used for analyzing the photon fluence of the PB after traversing the shown thicknesses of brass.

3.3.2 Modeling relative scatter dose and beam hardening

In the previous section it was established that the relative scatter dose is approximately linearly related to the thickness of the compensator material. A program was written in IDL to calculate the slopes $P^{(n)}_{t,med}$ of the straight lines fitting the data ($P^{(n)}_{t,med}$ vs. t) at each depth, z, and radial position, r, of the bins used in the water phantom. A sample of these data are plotted (solid lines) in the graphs in the left-hand column in figures 3.5, 3.6 and 3.7. The plots are for four arbitrary chosen depths (z) of 0.2, 2.0, 7.0 and 17 cm respectively. (Note: In these plots the raw data are shown connected by straight line segments to improve the visual appearance only. The symbols represent fitted functions that were derived as described hereunder. It was found that this way of representing the data was easier to interpret than the more conventional way of showing the data as symbols and the fitted functions as lines).

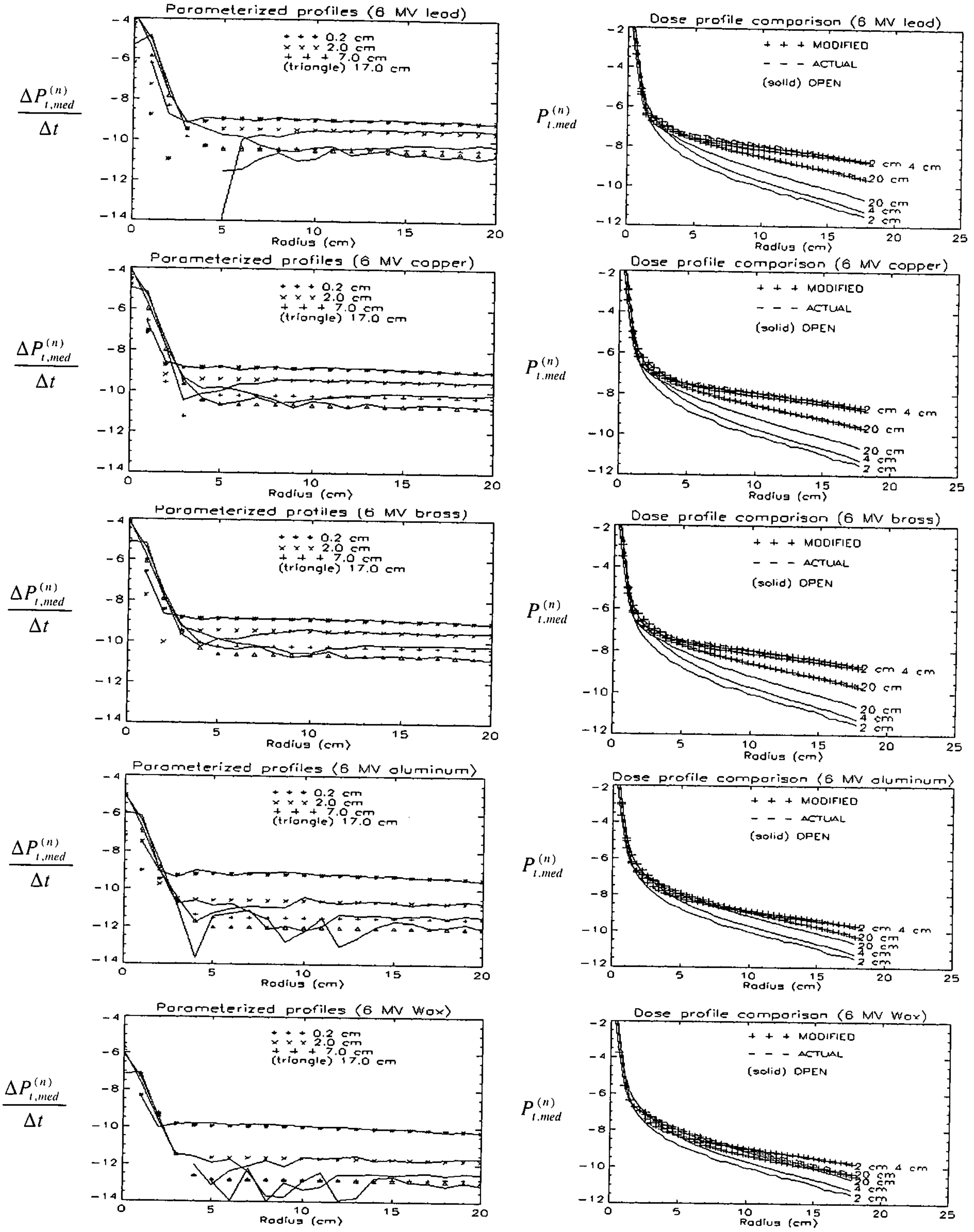

Figure 3.5 . Left: The change in the relative dose (6 MV) per unit absorber thickness A Gausian function was fitted beyond 5 cm radius. Another function was fitted to the data points near the PB axis. Right: Recalculated dose profiles at 2, 4 and 20 cm depth are compared to the actual profiles $p^{(n)}_{t,med}$

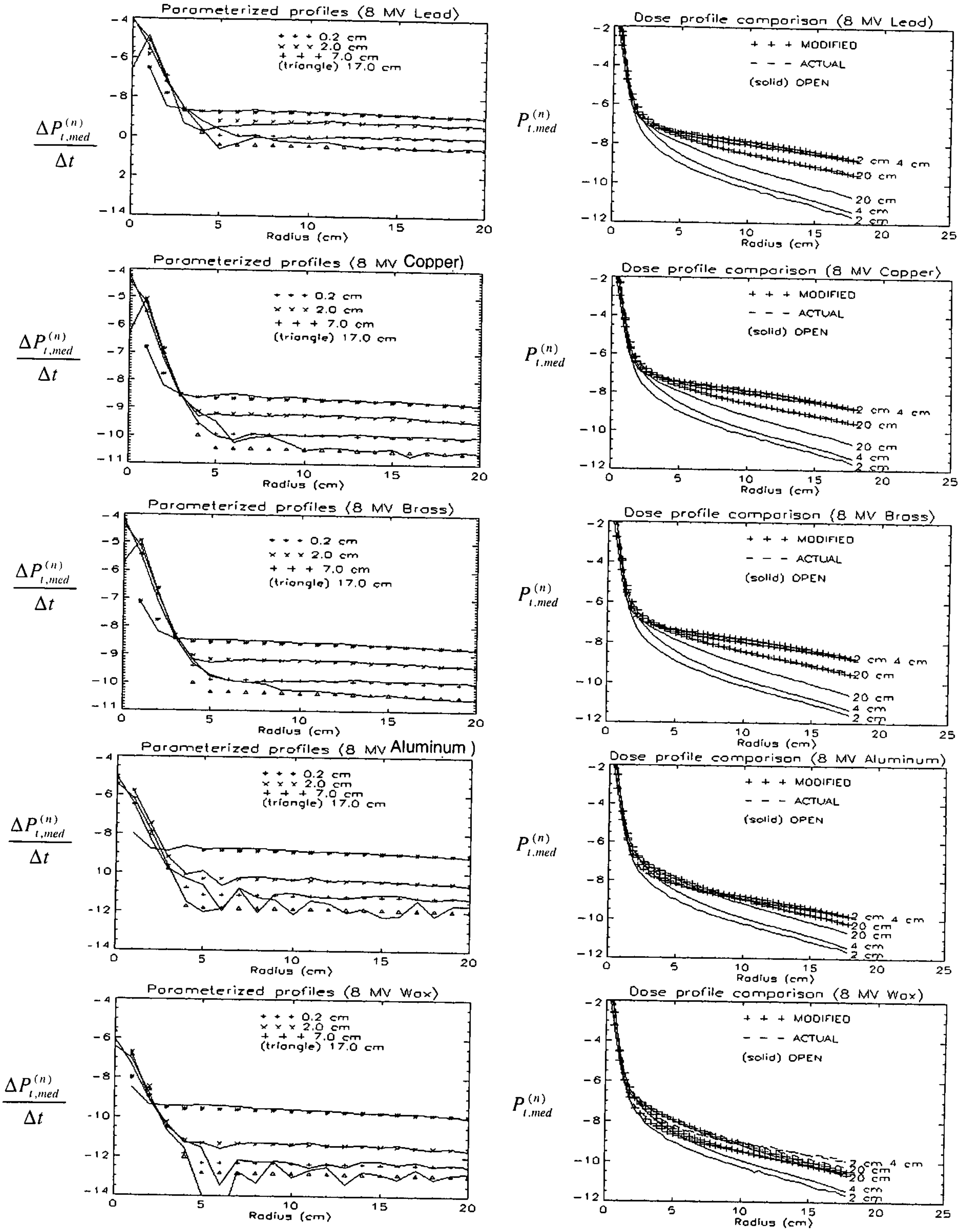

Figure 3.6 . Left: The change in the relative dose (8 MV) per unit absorber thickness A Gausian function was fitted beyond 5 cm radius. Another function was fitted to the data points near the PB axis. Right: Recalculated dose profiles at 2, 4 and 20 cm depth are compared to the actual profiles $p^{(n)}_{t,med}$

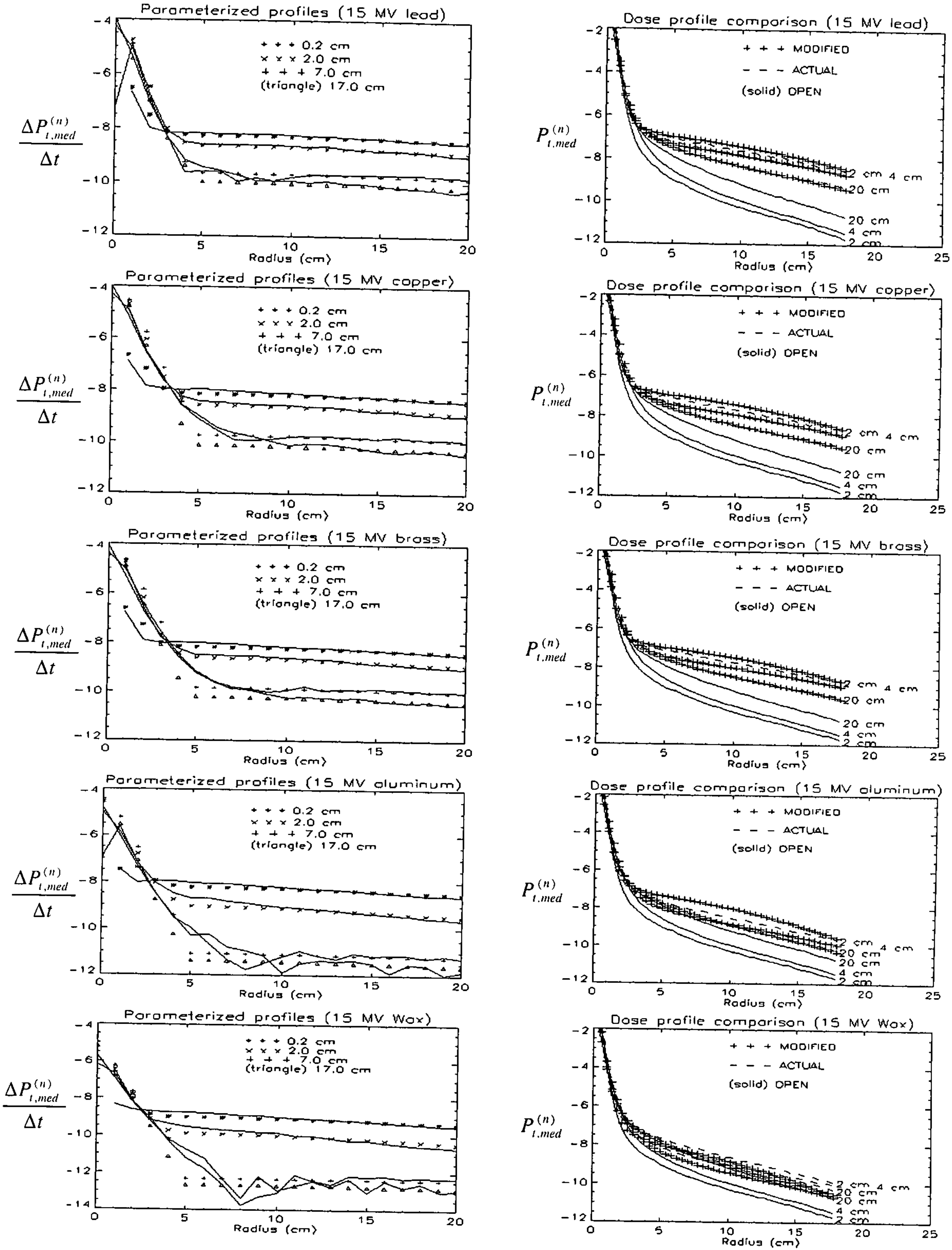

Figure 3.7 . Left: The change in the relative dose (15 MV) per unit absorber thickness A Gausian function was fitted beyond 5 cm radius. Another function was fitted to the data points near the PB axis. Right: Recalculated dose profiles at 2, 4 and 20 cm depth are compared to the actual profiles $p_{t,med}^{(n)}$

The slopes $\frac{\Delta P_t^{(n)}}{\Delta t}$ indicate the rate of change in the relative dose per unit absorber thickness. In all cases the slope values are relatively larger near the PB axis (CAX) and then decrease relative fast until a radial distance is reached where the further change with off-axis distance (radius) is relatively slow. The transition radius where this occurs is about 2 cm for depths near the surface but increases to about 4 cm at 17 cm depth for a 6 MV PB. For 8 MV and 15 MV the corresponding radii are 3 cm to 5 cm and 3 cm to 7 cm respectively. The dose profile in the region beyond the transition radius is considered to be caused by scattered radiation from the absorber material. In this study it is assumed that the slope profile in this scatter region has a gaussian shape for all energies and materials. Gaussian functions were fitted to the slope profiles from the transition radii to the maximum radius and has the form indicated by equation 3.3:

$$\alpha(r,z) = a_1(z)\exp(-a_2(z)r^2) \qquad 3.3$$

Where r is the radial distance and $a_1(z)$ and $a_2(z)$ are the fitting parameters that are functions of depth, as well as energy and compensator material. The parameters for the fitting functions were determined as follows: At each depth (z) two data points were chosen at random on the raw data of $P_{t,med}^{(n)}$ vs. radius on condition that they lay beyond a radius of 5 cm and spaced at least 25 annuli widths apart. (This spacing allowed for better conformance between the raw data and the fitted gaussian function). The two points were needed to solve for the two parameters in equation 3.3. This process was repeated 44 times, each time yielding a value for each parameter. The final value for each fitting parameter was defined as the average of the 44 calculated values. The fitted values are shown as symbols in figures 3.5 – 3.7, left columns.

The next step in the fitting procedure was to subtract the gaussian function from the original slopes over the total radius range. In theory if we had a perfect fit this should only leave non-zero values in the region between the PB axis and the transition radius. All residue slope values beyond the transition radius were set to zero. The remaining slope residues were fitted by the function represented in equation 3.4:

$$\beta(r,z) = b_1(z)(r - b_2(z))\exp(-b_3(z)r) \qquad 3.4$$

Where r is the radial distance and $b_1(z)$, $b_2(z)$ and $b_3(z)$ are fitting parameters which are functions of depth, as well as energy and compensator material.

The function β was chosen since it can model the rather complicated slope residue near the PB axis. For example, inspection of figure 3.7 shows for the case of, say, aluminum that the slope profile at 0.2 cm is nearly linear. This indicates exponential behaviour. On the same graph the slope profile at 7 cm depth starts off at a local minimum value, rises to a maximum and then declines. The function of the form in equation 3.4 was suitable to model these types of profile variations. The fitting of these functions were done in a similar way as was done to fit the slope points with the gaussian function.

Equation 3.3 represents the relative scatter enhancement while equation 3.4 represents the dose alteration on the PB axis due to different in-phantom scatter and beam hardening properties from the filtered PB. Figure 3.8 shows the relative dose enhancement caused by beam hardening and scatter for different brass absorbers at 8 MV. These curves were obtained by subtracting the open PB relative dose profile $P_0^{(n)}$ from the absorber modified PB relative dose profiles $P_{t,med}^{(n)}$. The modified pencil beam profiles were obtained for brass absorbers with the indicated thicknesses.

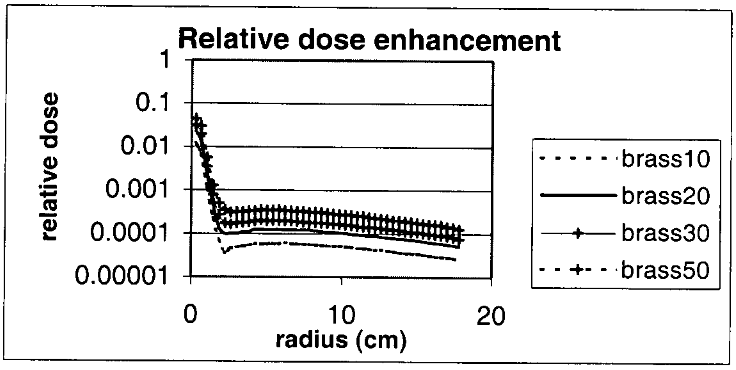

Figure 3.8. The dose enhancement relative to an open PB ($P_{t,brass}^{(n)} - P_0^{(n)}$) for a set of PBs after traversing a set of infinite brass slabs of thickness 1.0, 2.0, 3.0 and 5.0 cm. (I.e. the 5.0 cm thickness is represented by the legend brass50). The relative scatter contribution can be observed beyond 2 cm. Near the PB axis the scatter contribution is masked by beam hardening effects.

Near the PB axis the dose enhancement is due to beam hardening that is super-imposed on the scatter contribution of the brass absorber. Further away (beyond 5 cm from the PB axis) it is due to increased scatter contributions from the brass absorbers. The beam hardening effect causes a larger dose perturbation than the scatter from the absorber and should be taken into account in compensator modeling. The method of modeling compensators proposed here is to use the open PB and then to adjust it for beam hardening and scatter effects corresponding to the thickness of the compensator at the point of entry of the PB. In this study the open PB is modified by the addition of two terms.

The linear relation between the relative dose $P_{t,med}^{(n)}$ and absorber material thickness (t) can be used to determine the change in the PB dose profile for a given attenuator thickness using a PB model for an open unattenuated pencil beam $P_0^{(n)}$. The intercepts on the ordinate-axis of the lines in the graphs on the right in figures 3.1, 3.2 and 3.3 are equivalent to the relative dose for the open PB. The perturbation to the relative dose due to the presence of an attenuator is now modeled as:

$$\mathrm{P}_{\mathrm{t,med}}^{(n)}(\mathrm{r,z}) = P_0^{(n)}(\mathrm{r,z}) + \alpha(r,z)\mathrm{t} + \beta(r,z)\mathrm{t} \qquad 3.5$$

where α(r,z) and β(r,z) are obtained from equations 3.3 and 3.4. $P_{t,med}^{(n)}(r,z)$ is the scatter and beam hardening corrected relative dose at radial distance, r, and $P_0^{(n)}(r,z)$ is the relative dose without any absorber present at the same radial distance thus that for an open PB. The attenuator itself lowers the total (unnormalized) dose contribution due to absorption. We assume as a first approximation that $(P_{t,med})_{\max} = (P_0)_{\max}\exp(-\mu_{eff}(z)t)$ with $\mu_{eff}(z)$ the EAC for the smallest field/beamlet size derived in Chapter 2. The unnormalized dose will then be given by $P_{t,med} = P_{t,med}^{(n)}(P_{t,med})_{\max}$ and thus:

$$P_{t,med} = P_{t,med}^{(n)}(P_0)_{\max}\exp(-\mu_{eff}(z)t) \qquad 3.6$$

This is an approximation because $(P_0)_{\max}$ and $(P_{t,med})_{\max}$ do not necessarily occur at the same depth (z).

The dose profile modeling scheme as outlined in equations 3.3, 3.4 and 3.5 was tested and the results are shown in the right-hand column in figures 3.5, 3.6 and 3.7. In each graph the solid line indicates the dose profile for the open PB at 2, 4 and 20 cm depth in the EGSnrc water phantom. For the corresponding depths the dose profiles are also shown for the PB after traversing 5 cm of absorber material and is shown as dotted lines. The profiles shown for wax were obtained for the open PB after traversing 12 cm of wax. The modified open PB dose profiles, using equations 3.3 to 3.5 are shown as '+ + +'-symbols after setting t = 12.0 cm for wax and 5.0 cm for the rest of the materials. In figures 3.5 and 3.6 the agreement between the real hardened PB data (dotted lines) and the modified open PB profiles are in excellent agreement. For the 15 MV case the correspondence of the dose profiles is not as accurate near the surface (2 cm label). This can be correlated with the accuracy of the fits of the slopes in the opposite graphs (left column). For the 15 MV case the fits are not as accurate. In the left hand graphs the slope data appear to be quite noisy at depths indicated at 7 and 17 cm for most materials at the studied energies. An interesting feature here is that these slopes $\frac{\Delta P_{t,med}}{\Delta t}$ decrease with increasing depth (z). Thus the effect of the absorber material thickness on the relative dose profile decreases as the depth increases.

As a final validation of the dose profile modification scheme relative depth dose data were derived for circular fields with diameters of 10 and 20 cm using the open PB at each energy and modifying it as if it has traversed 5 cm of compensator material (12 cm for wax). These data are shown in figures 3.9, 3.10 and 3.11. In each graph the solid line represents the relative depth dose curve derived from the open PB, the broken line that from the real attenuated PB and the '+ + +' – symbols the curve obtained from the modified open PB. The depth dose data were calculated by using the cylindrical PB and utilizing the reciprocity theorem i.e. for a 10 cm circular field the dose in each annulus were summed up to a radius of 5 cm. The sum of the dose values in each annulus would yield the dose on the central PB axis. In general the correspondence between the depth doses obtained with the modified open PB and those obtained with the real PB is within a margin of 1 percent. The data for aluminum is somewhat less accurate. The relative depth dose curves for the 20 cm diameter circular field derived with the modified PB is closer to that derived with the open PB and in some cases, e.g. wax at all investigated beam energies, the large field size modified PB depth dose curves are very close to the open PB derived depth doses. For nearly all the other cases the correspondence between the open PB derived and the modified PB derived depth dose curves lie within 2 to 3 percent at depths less than 10 cm. For the 10 cm circular field the deviation of the open PB derived depth dose and the real and modified PB derived depth dose curves is more apparent. The increase in in-phantom scatter with field size thus reduces the effect of the changing PB profiles, i.e. more dose is deposited due to in-phantom scatter on the CAX, which in turn counters the effects of beam hardening on the CAX. For smaller fields CAX beam hardening would be more pronounced and the modified PB derived depth dose would deviate substantially from the open PB derived depth dose. This can be substantiated if the deviation of the depth dose curves is observed at all energies as a function of the material type. For wax, with its atomic number of 5.7 and physical density of 0.9 g/cm^3 the deviation is less and as the material density and atomic number increases this deviation is more pronounced. Higher atomic number and density materials will filter the PB to a higher degree. This would result in an increase in the relative dose as a function of depth, due to spectral changes in the beam that increases its penetration ability. The smaller field results in less scattered photons in the phantom that could counter this effect on the CAX.

An encouraging aspect of this dose profile modification scheme is that although the match of the slope profiles in figures 3.5, 3.6 and 3.7 at larger depths is not very accurate, it still yields reasonably accurate depth dose curves. The variance on the slope data can thus be smoothed out with the described fitting procedure. This is most apparent for wax and aluminum data at the larger depths in figures 3.5, 3.6 and 3.7. As an example the graph of lead at 6 MV (figure 3.5) shows an extreme deviation between the real $\frac{\Delta P_{t,med}}{\Delta t}$ profiles and the fitted $\frac{\Delta P_{t,med}}{\Delta t}$ profiles. However the resulting depth dose curves show agreement within 2 percent of the real filtered PB derived data (figure 3.8). Relatively larger statistical variance on the lead filtered PB at 6 MV might have caused this effect and could, when improved, lead to more accurate results. As a cautious generalization it seems that the dose profile modeling scheme should also be applicable for other compensator materials over the energies studied, since the depth dose curves for the worst cases such as wax and lead could be modeled successfully.

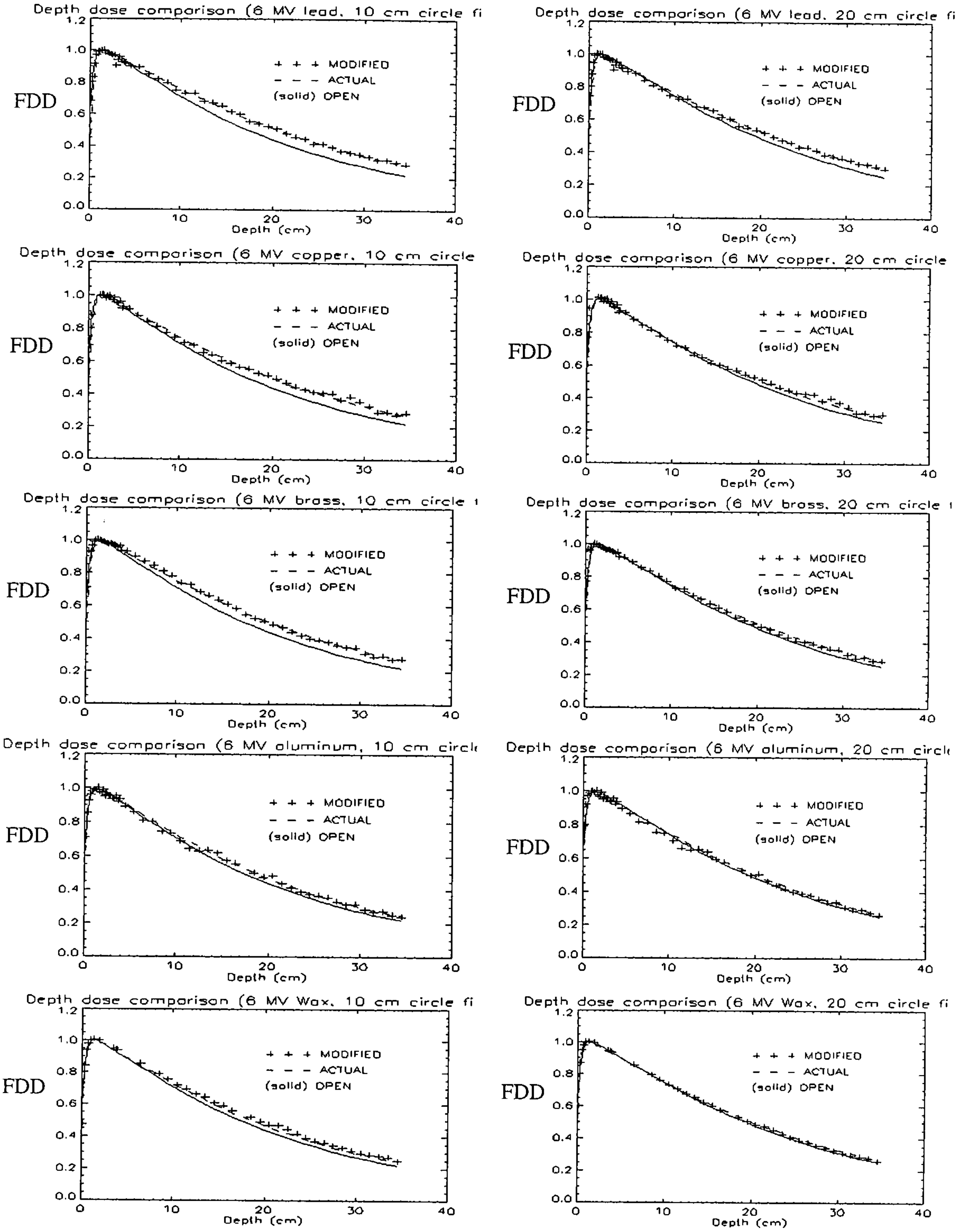

Figure 3.9. Fractional depth dose curves at 6 MV. The solid line represents the FDD curve derived from the open PB. The broken line that derived from a PB filtered by 5 cm compensator material. The symbols indicate the FDD curve calculated from the modified PB data. left: 10 cm diameter circle field, and right: 20 cm diameter circle field.

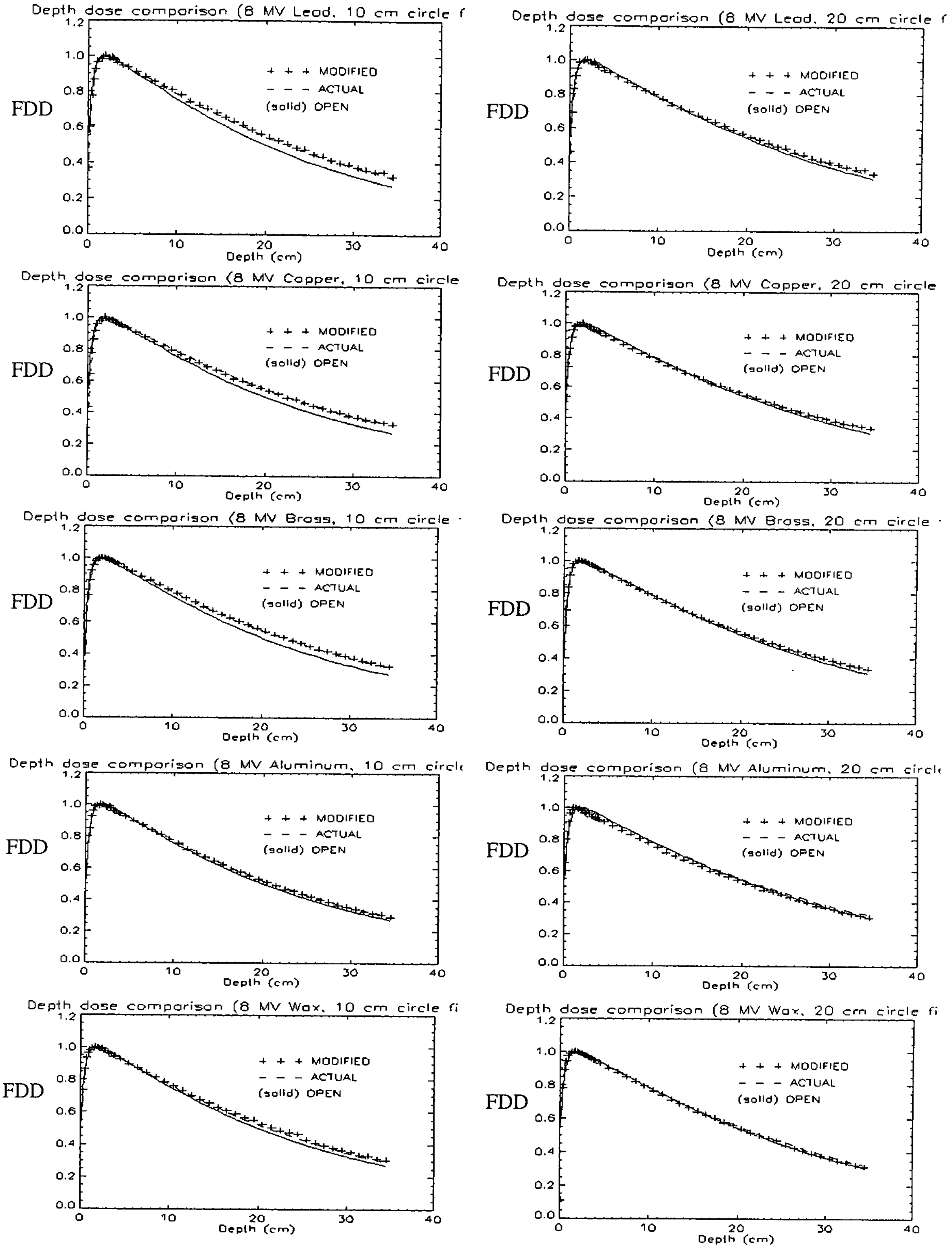

Figure 3.10. Fractional depth dose curves at 8 MV. The solid line represents the FDD curve derived from the open PB. The broken line that derived from a PB filtered by 5 cm compensator material. The symbols indicate the FDD curve calculated from the modified PB data. left: 10 cm diameter circle field, and right: 20 cm diameter circle field.

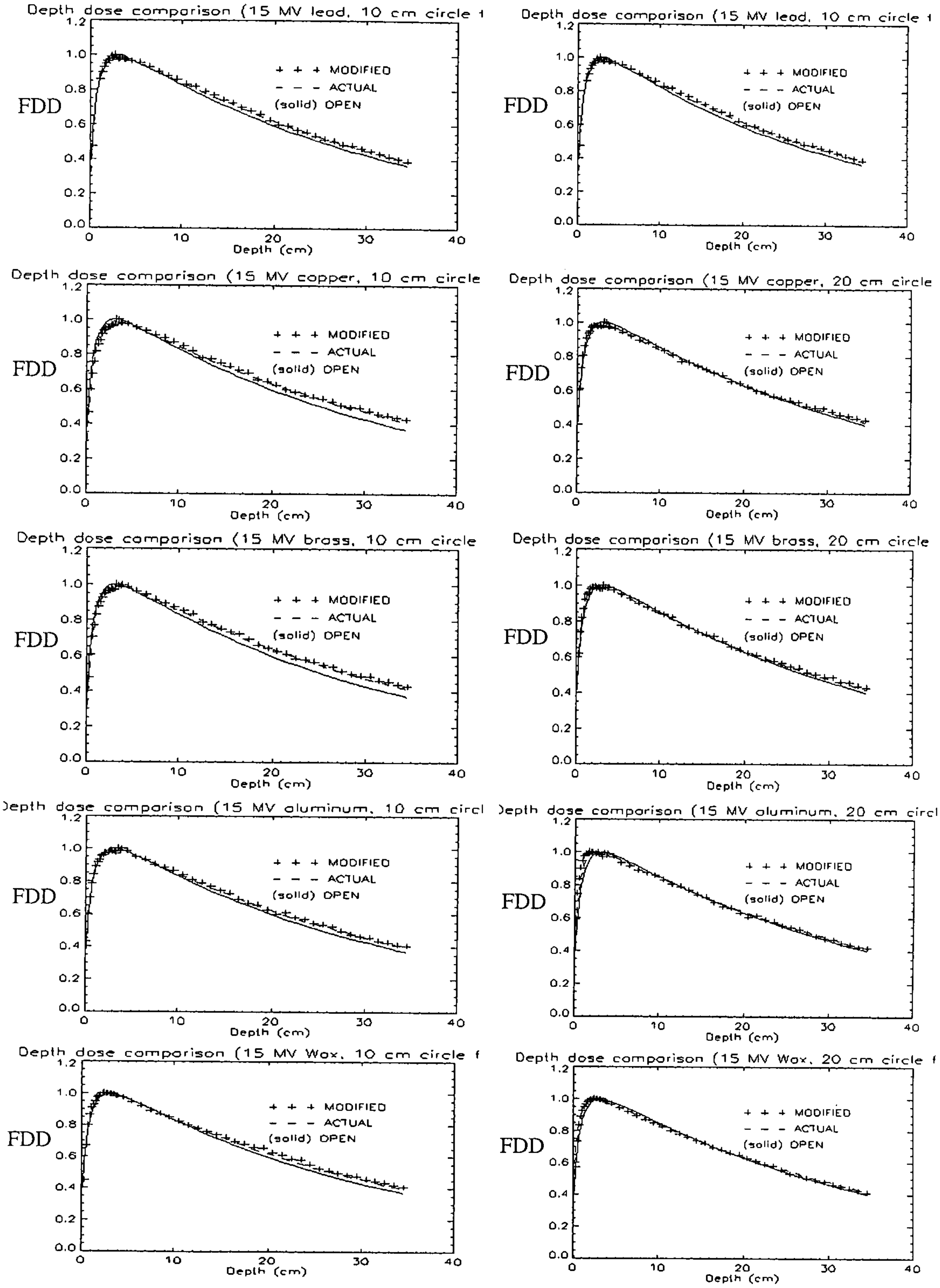

Figure 3.11. Fractional depth dose curves at15 MV. The solid line represents the FDD curve derived from the open PB. The broken line that derived from a PB filtered by 5 cm compensator material. The symbols indicate the FDD curve calculated from the modified PB data. left: 10 cm diameter circle field, and right: 20 cm diameter circle field.

3.4 The depth dependence of α

The parameters α(r,z) and β(r,z) in equation 3.5 are determined through the fitting parameters {a} and {b} in equations 3.3 and 3.4. The latter are functions of depth for each energy and material. A code was written in the IDL language to produce these parameters for the materials used in this study. As input, five normalized PB arrays are used, one open and four after traversing 1, 2, 3 and 5 cm of the compensator material (for wax, t = 0, 3, 6, 9 and 12 cm).

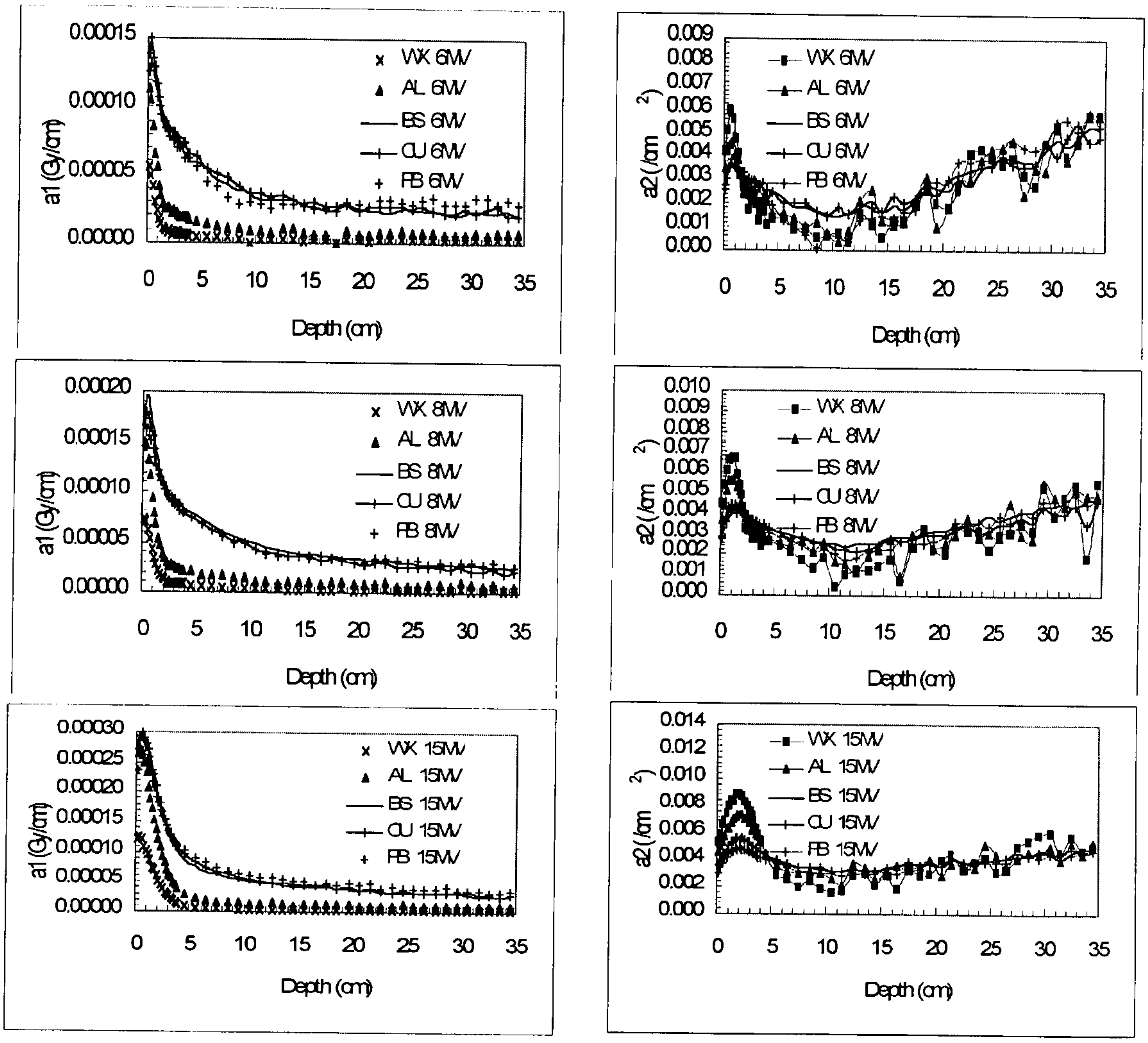

Figure 3.12. The fitting parameters a_1 (left column) and a_2 (right column) in equation 3.3 as a function of depth. The top pair of graphs are for 6 MV PB energy, middle, 8 MV and bottom, 15 MV.

The parameters α and β are derived as output from this code. This code can be viewed as a pre-processor code that calculates the relevant parameters for routine use in the modeling of compensator shapes. Graphs of these parameters are shown in figure 3.12 and 13.

In figure 3.12, left, parameter a_1 represents the rate of change with absorber thickness of the scattered radiation on the CAX, relative to that of the open PB. Parameter a_2 represents its variation in the off-axis direction (figure 3.12, right). The value of parameter a_1 decreases as a function of depth for all PB energies and for all materials. Parameter a_1 has the smallest value for wax, followed by aluminum, for all energies. The values for brass, copper and lead are similar and are distinctly different from both aluminum and wax. The rate of change of the relative dose per unit absorber thickness is large near the surface, decreasing fast initially and then more gradually as a function of depth. This 'cross over' depth is defined as the transition depth and is a function of energy. For wax, for example, this radius is about 1, 2 and 4 cm for 6, 8 and 15 MV respectively.

Two factors could explain the behavior of a_1 with depth namely: A) The increased number of scattered particles from the absorbers reaching the water phantom, which includes electrons and low energy photons, due to less efficient filtering by low atomic number and -density materials. B) Beam filtration that increases with density and atomic number. Thus wax and aluminum would cause a significant number of electrons and low energy photons to reach the surface of the water phantom. This causes a_1 to decline rapidly as a function of depth, due to electrons and low energy photons that deposit most of their energy near the water surface. $\frac{\Delta P_{t,med}}{\Delta t}$ would vary more rapidly near the water surface where the number of low energy particles can be reduced significantly as the absorber thickness is increased. Wax and aluminum do not filter the beam as efficiently as brass, copper and lead. The presence of charged particles such as electrons (and some positrons) near the water surface would explain why the $\frac{\Delta P_{t,med}}{\Delta t}$ is high for all materials at the water surface. This distinction between wax and aluminum compared to other materials might be linked to their electron densities. Wax and aluminum have distinctly lower electron densities compared to the other materials. If table 2.2 in Chapter 2 is considered, and the product of density and Z/A (mass electron density) is taken the following electron densities (/cm^3) are obtained: Wax (0.67), aluminum (1.30), brass (3.87), copper (4.07) and lead (4.50). Since Compton interactions dominate at the studied PB energies, the electron density would play a significant role in the number of photon interactions that would take place per unit absorber thickness. From a depth of 10 cm at all energies, a_l varies weakly as a function of depth. This might be due to the fact that all charged particles entering the water are completely stopped here and interactions beyond this depth considered as pure photon interactions. Careful inspection shows a_l still decreases slightly as a function of depth due to increased in-phantom scatter as the PB diverges as a function of depth in water. An interesting observation is that the values for a_l are smaller at 6 MV compared to 8 and 15 MV PB energies. This suggests that the rate of change in the scatter dose as a function of absorber thickness is less for 6 MV, compared to the other energies. This can be ascribed to the fact that more in-phantom scatter would occur for 6 MV than for 8 or 15 MV. This scatter counters the effect of radiation absorption as a function of thicker material. The influence of the absorber material would have a more pronounced effect at higher PB energies where in-phantom scatter would be less.

Due to the regularity of the parameter a_l with depth, for each material and energy, it was found that it could be conveniently parameterized as a function of depth with the equation:

$$a_l(z, med, E) = c_1 \exp(-c_2 z^2) + \frac{c_3 \tanh(c_4 z)}{\sqrt{c_5 z}} \qquad 3.7$$

where $c_1 - c_5$ are fitting parameters, and z indicates the depth. The indices ‘med’ and ‘E’ indicate that these fitting parameters are dependent on the medium and the PB energy (E).

Table 3.1 shows these fitting parameters.

Table 3.1. Fitting parameters $\{c_i\}$ for parameter a_1 in equation 3.3 as fitted by equation 3.7.

Material	Energy (MV)	c_1 (Gy/cm)	c_2 (cm^{-2})	c_3 (Gy/cm)	c_4 (cm^{-1})	c_5 (cm^{-1})
Wax	6	0.00005	1.30	0.000011	1.0	1.0
	8	0.00007	1.10	0.000014	1.5	1.0
	15	0.00009	0.18	0.000015	10.0	0.9
Aluminum	6	0.00010	1.30	0.000035	1.0	1.0
	8	0.00014	1.10	0.000041	1.0	1.0
	15	0.00025	0.23	0.000045	1.0	1.0
Brass	6	0.00010	1.30	0.000120	0.8	1.0
	8	0.00013	1.30	0.000155	1.0	1.0
	15	0.00018	0.19	0.000170	1.0	1.0
Copper	6	0.00010	1.30	0.000120	1.0	1.0
	8	0.00012	0.80	0.000090	1.0	0.4
	15	0.00020	0.18	0.000250	0.8	2.0
Lead	6	0.00010	1.30	0.000550	0.7	20.0
	8	0.00009	1.00	0.000090	1.0	0.4
	15	0.00016	0.30	0.000200	0.8	0.9

Parameter a_2 in figure 3.12, right column, is shown for each energy, next to similar graphs for parameter a_1 in the left column. The data are sensitive to noise in the original PB dose arrays which is reflected in the oscillations in the graphs. Parameter a_2 determines how fast parameter a_1 would 'decay' as a function of off-axis position, or in other words a_2 determines the curvature of the gaussian function α. On the CAX α is at a maximum. At positions located off-axially the rate of change decreases, since more scattered radiation from the PB on the CAX and photons introduced by the compensator will deposit their energy at these locations. This can be regarded as increasing in-phantom scatter regions that reduce the change in α.

The variation of parameter a_2 with depth has certain characteristics. At each energy a_2 builds up to a local maximum at about 0.5, 1 and 2 cm depth. This corresponds roughly to the D_{max} positions at the respective energies of 6, 8 and 15 MV respectively. At roughly 10 cm depth, the curves have a broad minimum and then rise approximately linearly to maximum values of 0.006, 0.005 and 0.004 cm^{-2} at the respective energies of 6, 8 and 15

MV. Beyond a depth of 10 cm a_2 is approximately the same for all material at a specific energy, if the noisy character of the data is taken into account. Careful inspection of the graphs for a_2 reveals that the materials copper and brass have again very similar parameters at the respective energies. Data for wax tend to be smaller after the build-up region. There is greater variability in the graphs for wax and aluminum than for the other materials. At 1.5, 2 and 4 cm depth for 6, 8 and 15 MV respectively, the values of a_2 seems to converge for all materials.

From the surface, a_2 increases up to the D_{max} positions. Here the gaussian shape of α has the highest curvature. Electrons and low energy photons reach the surface of the water phantom from the attenuators/absorbers. They give rise to many scatter events near the phantom surface. At larger depths some are already absorbed in water and there are relatively less scatter. Thus a_2 would increase. For brass, copper and lead the more effective filtration of the beam would reduce the relative number of electrons and low energy photons that reach the phantom surface. Thus a_2 would be smaller than for wax and aluminum. From its maximum value, a_2 declines with increasing depth due to increased in-phantom scatter, before increasing beyond 10 cm depth.

For each material and energy it was found that parameter a_2 could be parameterized as a function of depth with the equation:

$$a_2(z, med, E) = e_1 z \exp(-e_2 z) + e_3 z + e_4 \qquad 3.8$$

where e_1 – e_4 are fitting parameters, and z indicates the depth. The indices 'med' and 'E' indicate that these fitting parameters are dependent on the medium and the PB energy (E).

Table 3.2 shows these fitting parameters.

Table 3.2. Fitting parameters $\{e_i\}$ for parameter a_2 in equation 3.3 as fitted by equation 3.8.

Material	Energy (MV)	e_1 (cm^{-3})	e_2 (cm^{-1})	e_3 (cm^{-3})	e_4 (cm^{-2})
Wax	6	0.156	0.70	0.00014	0.0005
	8	0.019	1.10	0.00011	0.0003
	15	0.0135	0.60	0.00016	0.0002
Aluminum	6	0.009	0.59	0.00010	0.0015
	8	0.015	1.10	0.00011	0.0007
	15	0.0095	0.60	0.00010	0.0014
Brass	6	0.0047	0.55	0.00008	0.0022
	8	0.0052	0.60	0.00011	0.0010
	15	0.0051	0.60	0.000017	0.0023
Copper	6	0.0045	0.55	0.00007	0.0023
	8	0.0044	0.57	0.00008	0.0014
	15	0.0041	0.50	0.000075	0.0022
Lead	6	0.0037	0.51	0.000075	0.0020
	8	0.0055	0.52	0.000135	0.0002
		0.50	0.000085	0.0018	

3.5 The depth dependence of β

In figure 3.13 a and b the fitting parameters {b} are shown. These parameters were derived from the residue dose per unit absorber thickness (β) profiles, after subtracting the assumed gaussian shaped α profiles from the total $\frac{\Delta P_{t,med}}{\Delta t}$ profiles. Figure 3.8 illustrates the relative dose enhancement for 8 MV photons after traversing certain thicknesses of brass. It can be observed that the dose follows a gaussian pattern beyond a radius of 3 cm. α also followed a gaussian pattern as discussed. The region from the PB axis to a radius of 3 cm shows a sharp increase in the relative dose (figure 3.8). The $\frac{\Delta P_{t,med}}{\Delta t}$ also increased as shown for all the cases in figures 3.5, 3.6 and 3.7. Equation 3.4 was used to model these trends. The data are plotted rather than shown as tables.

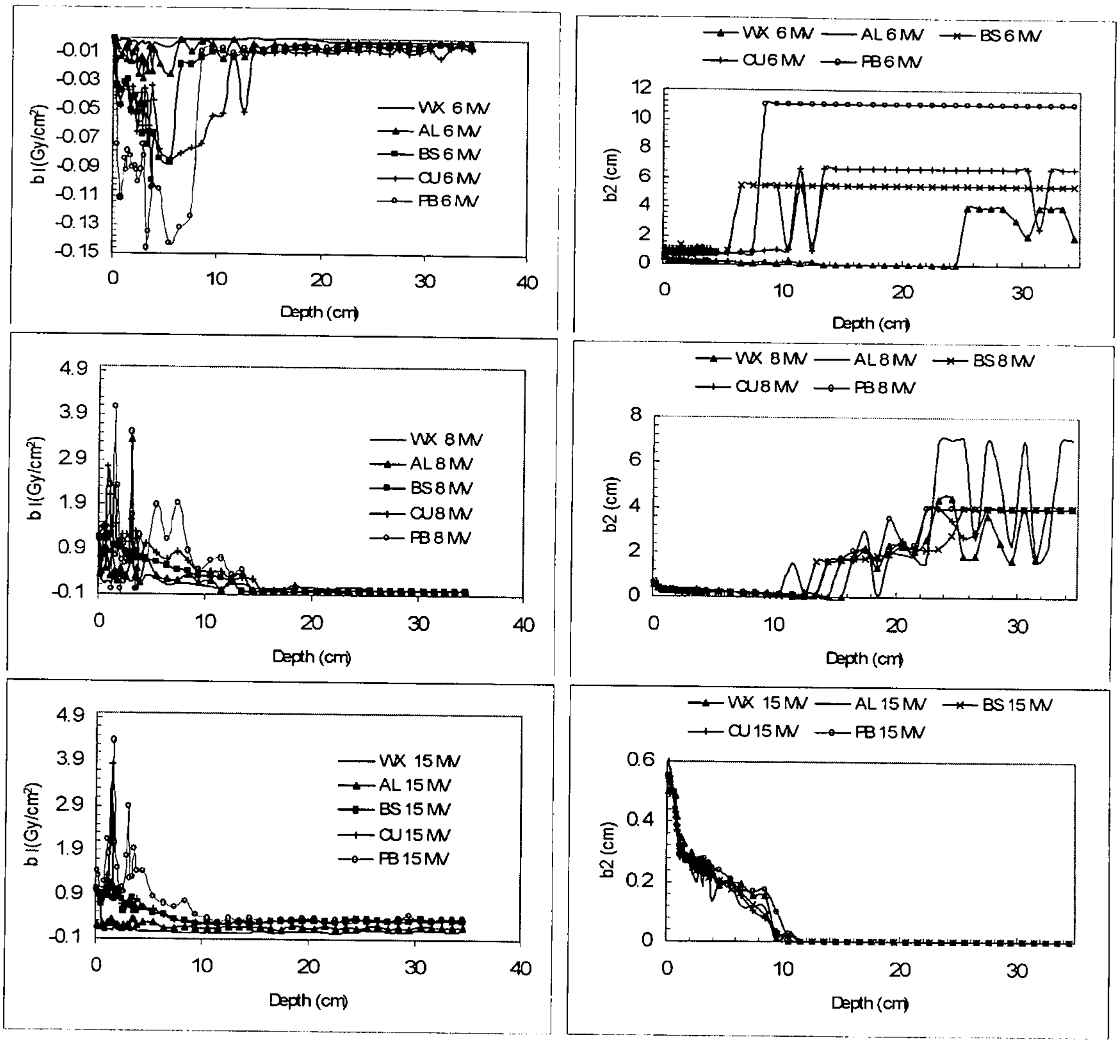

Figure 3.13 a. Fitting parameters for the indicated materials, b1 (left column) and b2 (right column) for equation 3.4 for 6 MV (top), 8 MV (middle) and 15 MV (bottom).

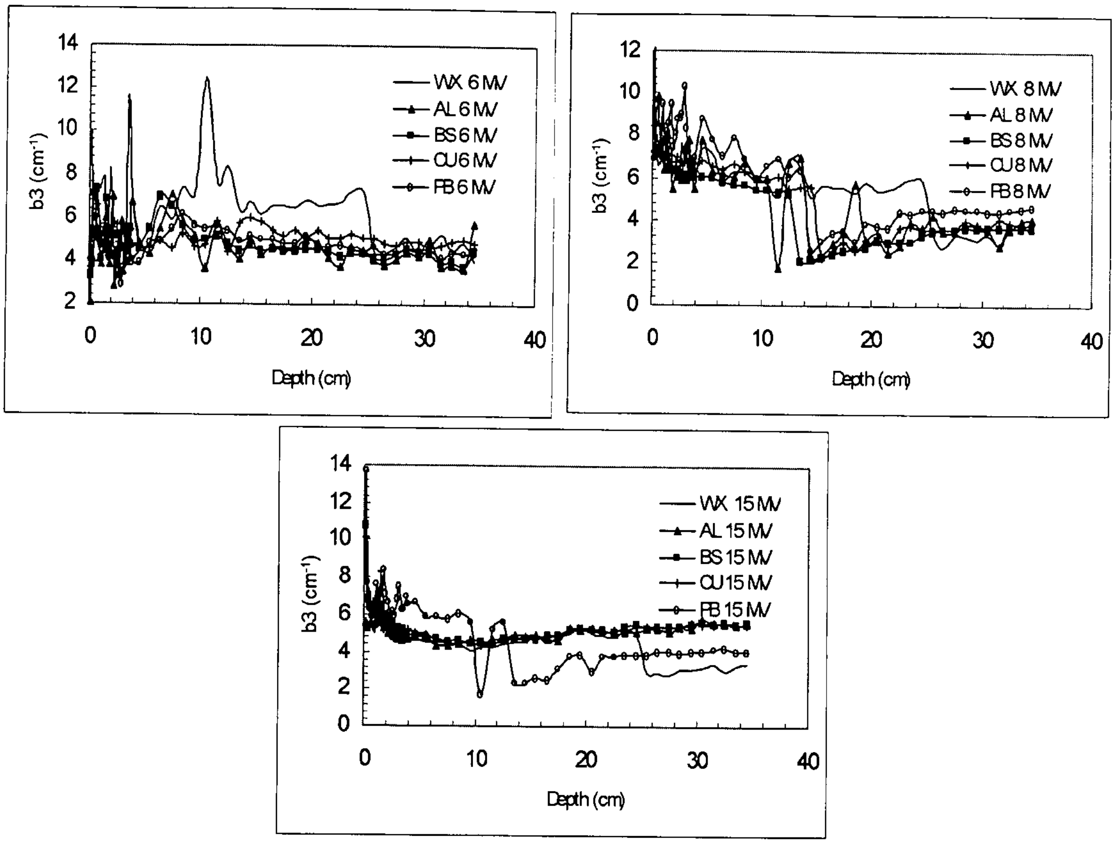

Figure 3.13 b. Fitting parameters (b3) for the indicated materials, 6 MV (top left), 8 MV (top right) and 15 MV (bottom).

In equation 3.4, parameter b_1 indicates the amplitude of β on the PB axis. If negative, it indicates that the dose should decline relative to the open PB as the absorber thickness is increased. For 6 MV this is the case. Beam hardening is most prominent for the 6 MV PB, compared to 8 and 15 MV, where the values for b_1 are positive. The higher degree of filtering at the lower energy increases the penetration depth of the photons. This results in relatively less dose being imparted in the central voxels in the PB because the energy is now spread out over a larger depth interval. The higher the degree of filtration, the more negative the values at 6 MV would then have to be. Careful inspection of the top left graph in figure 3.13 confirms this e.g. for lead and copper at depths less than 10 cm. At larger depths, the increased scatter counters this beam hardening effect on the PB field size scale, leading to smaller absolute values for b_1. This is also evident at 8 and 15 MV. For 15 MV these values are about 0.5 compared to 0.1 at 8 MV and -0.01 at 6 MV. This shows that the filtered 15 MV PB has the largest beam penetration, compared to 8 and 6

MV, such that β is largest for 15 MV. Also less scatter is present on the PB axis that could counter β for 15 MV photons. For the case of 8 and 15 MV the effects at depths less than 10 cm are reversed, compared to 6 MV. The data range for 6 MV is, however much less, than for the higher energy cases. The absolute range for b_1 is of the order of 0.15 units at 6 MV, compared to roughly 4 units for 8 and 15 MV. Thus compared to the latter energies, 6 MV would produce no significant beam hardening effects when β is evaluated. α largely masks the effect for 6 MV. The higher beam energies exhibit a relative increase in β in the 3 – 10 cm depth range. This can be ascribed to a larger dose buildup depth as the filtered beam energy increases. As expected β should be the highest for lead, followed by brass and copper.

Equation 3.4 can model off-axis maximum values for β. The example for 15 MV shows this (bottom right) in figure 3.13 a. Here scattered photons near the surface cause a local maximum at off axis positions, this effect changes as the depth is increased. At depths larger than 10 cm the increased scatter causes a shift in the local maximum value that now lies on or very close to the PB axis. Here β behaves exponentially where $b2 \approx 0$. The data for 6 and 8 MV behaves 'spurious' and might be due to relatively large noise on the data. In conjunction with this, parameter b_3 indicates the decay rate of equation 3.4. For all cases shown in figure 3.13 b they indicate a value of b_3 roughly around 5 units. This indicates that equation 3.4 decays very rapidly as a function of off-axis distance and show the lateral influence of beam hardening effects of the PB.

3.6 Dose calculations for real compensators using the modified PBs

The open PB dose profile can be adjusted at an arbitrary depth to take beam hardening and scatter into account. In order to use these equations in compensator dose calculations, the following steps would be performed:

a) Determine the depth (z) of the plane at which the dose should be modulated.
b) Use the open PB dose profile at depth (z) as the basis for dose calculations
c) Calculate the value for α from equation 3.3 and β from equation 3.4, using the parameters for a_1, a_2, b_1, b_2 and b_3 as shown for the desired compensator material.

d) If the PB traverses a compensator of thickness, t, then alter its dose profile using equation 3.5 with the correct values for α and β at depth, z, as found in c).

e) Scale this PB dose profile at depth, z, with the effective attenuation coefficient as indicated in equation 3.6.

f) Calculate the dose distribution in the plane of interest located at depth, z for the modified PB at the relevant entrance site.

g) Repeat this whole process (d – f) for all entrance positions of the PBs covering the field area, using the corresponding compensator thickness, t, for each entrance position.

The modified PB at depth z is thus calculated from:

$$P_{t,med}(r,z) = \{P_0(r,z) + [a_1 \exp(-a_2 r^2) + b_1 (r - b_2) \exp(-b_3 r)]t\} \exp(-u_{eff}(z)t) \qquad 3.9$$

The effect of electron density of the compensator material on scatter and beam hardening was not studied since it falls outside the scope of this study.

3.4 Conclusion

In this study it was found that the relative dose for a set of normalized PBs, after traversing various thicknesses of wax, aluminum, brass, copper and lead, was linear in the material thickness as expressed by equation 3.4. The slopes of the lines of relative dose vs. absorber thickness were defined as $\frac{\Delta P_{t,med}}{\Delta t}$ and could be decomposed into a scatter part α and a beam hardening part β. α could be modeled with a gaussian function and β with another function. Despite the noise on the parameters for these functions, they could successfully reproduce the normalized depth dose data when compared to depth dose curves produced by the actual filtered PBs for 5 cm of filtered material (wax = 12 cm) for 10 and 20 cm circle fields. If a PB parameterization equation such as that of Ahnesjö *et al.*, (equation 3.1) is used to parameterize the dose profiles at each depth for a open PB, then it can be expanded as in equation 3.9 to include the effects of compensator materials. This approach can then be applied to compensators where a superposition method can be used to calculate the dose in water at a certain reference depth.

3.8 References

[1] S.V. Spirou and C.S. Chui, ‘Generation of arbitrary intensity-profiles by dynamic jaws or multileaf collimators’, Med. Phys. **21**, 1031 - 1041 (1994).

[2] S. Webb, ‘Intensity-modulated radiation therapy using only jaws and a mask’, Phys. Med. Biol. **47**, 257 - 275 (2002).

[3] J.H. Kung, G.T.Y. Chen and F.K. Kuchnir, “A monitor unit verification calculation in intensity modulated radiotherapy as a dosimetry quality assurance” Med. Phys. **27**, 2226 - 2230 (2000).

[4] M.R. Arnfield, J.V. Siebers, J.O. Kim, Q. Wu, P.J. Keall and R. Mohan, ” A method for determining multileaf collimator transmission and scatter for dynamic intensity modulated radiotherapy” Med. Phys. **27**, 2231 - 2241 (2000).

[5] J.D. Azcona, R.A.C. Siochi and I. Azinovic, “Quality assurance in IMRT: Importance of the transmission through the jaws for accurate calculation of absolute doses and relative distributions”, Med. Phys. **29**, 269 - 274 (2002).

[6] L. Wang, C-S Chui and M. Lovelock, ‘ A patient-specific Monte Carlo dose-calculation method for photon beams’, Med. Phys. **25**, 867 - 878 (1998).

[7] J.S. Li, T. Pawlicki, J.Deng, S.B. Jiang, E. Mok and C-M Ma, “Validation of a Monte Carlo dose calculation tool for radiotherapy treatment planning”, Phys. Med. Biol. **45**, 2969 - 2985 (2000).

[8] O.Z. Ostiapak, Y. Zhu and J. Van Dyk, “ Refinements of the finite-size pencil beam model of three-domensional photon dose calculation”, Med. Phys. **24**, 743 - 750 (1997).

[9] A. Boyer, L. Xing, C-M. Ma, B. Curran, R. Hill, A. Kania and A. Bleier, " Theoretical considerations of monitor unit calculations for intensity modulated beam treatment planning " Med. Phys. **26**, 187 - 195 (1999).

[10] B. Zackrisson, M. Arevärn and M. Karlsson, " Optimized MLC-beam arrangements for tangential breast irradiation", Radiotherapy and Oncology **54**, 209 - 212 (2000).

[11] L.Weber and F. Laursen, 'Dosimetric verification of modulated photon fields by means of compensators fo a kenel model' Radiotherapy and Oncology. **62**, 87 - 93 (2002).

[12] J.V. Siebers, M. Lauterbach, S. Tong, Q. Wu and R. Mohan, 'Reducing dose calculation time for accurate iterative IMRT planning', Med.Phys. **29**, 231 – 237 (2002).

[13] P.S. Basran, W. Ancbacher, G.C. Field and B.R. Murray, ' Evaluation of optimized compensators on a 3D planning system.', Med. Phys. **25**, 1837 – 1844 (1998).

[14] W. Laub, M. Alber, M. Birkner and F. Nüsslin, " Monte Carlo dose computation for IMRT optimization", Phys. Med. Biol. **45**, 1741 - 1754 (2000).

[15] A. Ahnesjö, L. Weber and P. Nilsson, " Modeling transmission and scatter for photon beam attenuators", Med. Phys. **22**, 1711 - 1721 (1995).

[16] A. Ahnesjö, ' Analytical modeling of photon scatter from flattening filters in photon therapy beams.', Med. Phys. **21**, 1227 – 1235 (1994).

[17] A. Ahnesjö, ' Colimator scatter in photon therapy beams.', Med. Phys. **22**, 267 – 278.

[18] A. Ahnesjö, M. Saxner, and A. Trepp, ' A pencil beam model for photon dose calculation.' Med. Phys. **19**, 263 – 273 (1991).

[19] M. K. Islam and J. Van Dyk, ' Effects of scatter generated by beam-modifying absorbers in megavoltage photon beams.', Med. Phys. **22**, 2075 – 2081 (1995).

[20] A. Ahnesjö and M.M. Aspradakis, " Dose calculations for external photon beams in radiotherapy", Phys. Med. Biol. **44**, R99 - R155 (1999).

[21] P-H. Huang, L.M. Chin and B.E. Bjärngard, ' Scattered photons produced by beam-modifying fitlers. ' Med. Phys. **13**, 57 – 63 (1986).

[22] E. Papiez and G. Froeze, ' The calculation of transmission through a photon beam attenuator using sector integration.' Med. Phys. **17**, 281 – 286 (1990).

[23] M.E. Castelanos and J.C. Rosenwald, ' Evaluation of the scatter field for high-energy photon beam attenuators.' Phys. Med. Biol. **43**, 277 - 290 (1998).

[24] L. Weber and F. Laursen, "Dosimetric verification of modulated photon fields by means of compensators for a kernel model', Radiotherapy and Oncology **62**, 87 – 93 (2001).

[25] E.L. Chaney and T.J. Cullip,'A Monte Carlo study of accelerator head scatter', Med. Phys. **21**, 1383 - 1390 (1994).

[26] I. Kawrakow, " Accurate condensed history simulation of electron trasport: I. EGSnrc, the new EGS4 version", Med. Phys. **27**, 485 - 498 (2000).

[27] W.R. Nelson, H. Hirayama and D.W.O. Rogers, The EGS4 Code System SLAC-Report-265, Stanford Linear Accelerator Center (1985).

[28] D.W.O. Rogers, B.A. Faddegon, G.X. Ding, C-M. Ma, J. We and T.R. Mackie, "BEAM: A Monte Carlo code to simulate radiotherapy treatment units.", Med. Phys. **22**, 503 – 525 (1995).

[29] C.-M. Ma and D.W.O. Rogers, 'BEAMDP Users Manual', National Research Council of Canada. Report PIRS-0509B (NRC, Ottawa), (1995).

[30] S. Rathee, B.A. McClean, and C. Field, "An improved method for rebinning kernels from cylindrical to cartesian coordinates", Med. Phys. **20**, 1343 – 1351 (1993).

[31] P. Storchi and E. Woudstra, "Calculation of the absorbed dose distribution due to irregularly shaped photon beams using pencil beam kernels derived from basic beam data", Phys. Med. Biol. **41**, 637 - 656 (1996).

[32] L. Wang and S.L. Jacques, "Optimized radial and angular positions in Monte Carlo modelling", Med. Phys. **21**, 1081 – 1083 (1994).

CHAPTER 4

Description and dosimetric evaluation of a pencil beam based compensator planning system for regular open fields

4 Preface

Chapter 2 described the generation and properties of effective attenuation coefficients (EACs). Chapter 3 described a method to model the relative scatter and beam hardening effects on pencil beams (PBs) transmitted through various thicknesses of attenuating/compensator materials. It was found that for each material and energy the relative scatter and beam hardening could be modeled by adding modifying functions to the normalized open PB dose profile. The next step is described in this Chapter and concerns itself with the development and benchmarking of an algorithm that incorporates the EAC, scatter and beam hardening in order to design compensators. Two topics are treated namely: a) The development of a fast rebinning algorithm and b) the testing of its performance against DOSXYZ, by the comparison of depth dose curves and dose profiles. These tests verified the rebinning algorithm.

4.1 Introduction

The compensator planning system (CPS) is described in this section. Its operation is based on the idea described in Chapter 3, namely that a open PB can be modified to include the effect of a) beam hardening and b) compensator induced scatter. By adding a suitable function to e.g. the well-known parameterization equation of Ahnesjö *et al.*,[1] describing the open PB, these effects can be included. Dose calculations using convolution/superposition methods are most conveniently performed in a Cartesian coordinate system and this requires the rebinning of the MC generated PBs from cylindrical to cartesian co-ordinates. Several models exist for the rebinning of PBs into cartesian co-ordinates, including the area overlap method[2] and a modified area overlap method[3] that involves linear interpolation between dose points and radial subdivisions of the overlapping area. A simplified rebinning model was developed here for the CPS which is much faster. The initial model was very simple and fast, but fine adjustments were needed in order to fit the depth dose curves derived with it to the original cylindrical PB generated depth dose curves. It is ultimately compared to DOSXYZ data for various field sizes in terms of a) Relative depth dose and b) beam profiles.

4.2 Description of the compensator planning system (CPS)

The CPS was developed to design models of compensators from the beamlet intensity maps produced by an inverse planning system with the ultimate goal of using these compensators for optimized IMRT. Its concept is described in the flow diagram below: An optimization code will provide a set of beamlet intensity maps for each field in the IMRT plan. Each map contains a 2D beam weight distribution. The beamlet weights (w_{ij}) are transformed into a map of compensator thicknesses by the CPS which, in-turn, provides a suitable output file for a local in-house built computer controlled compensator milling machine/cutter.

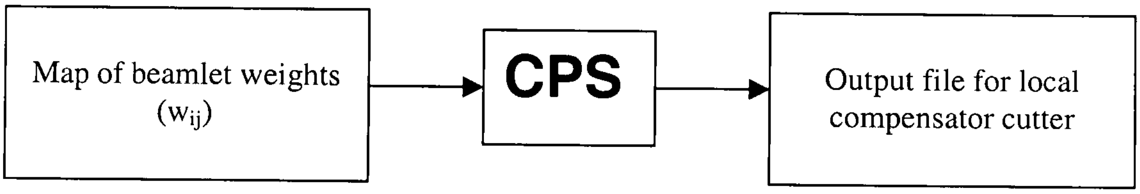

Figure 4.1. CPS designed as an interface between optimization output and input for compensator milling machine.

The operation of the CPS can be described with the aid of figure 4.2.

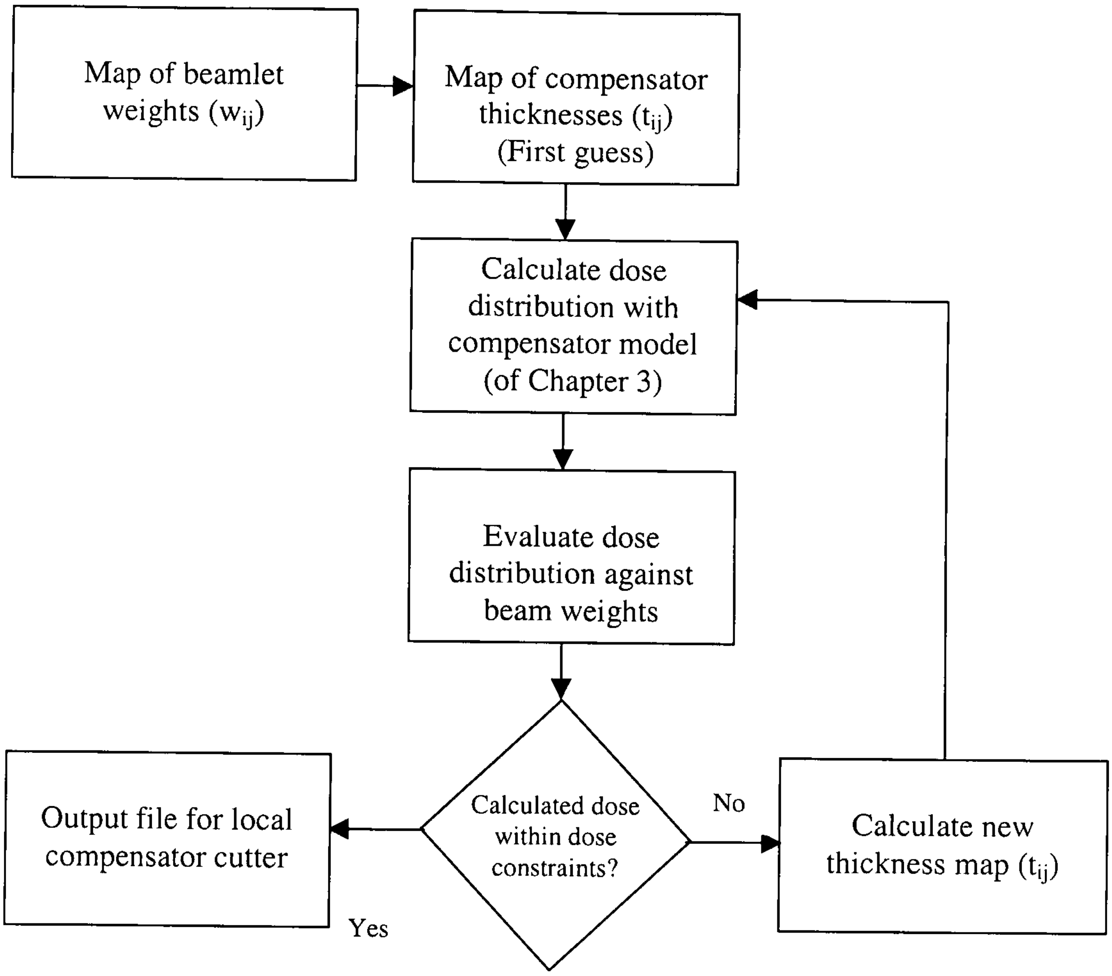

Figure 4.2. Flow chart of the CPS algorithm.

As mentioned, a set of maps containing the beamlet weights for each field in an IMRT plan is supplied by an optimization code. The object of such an optimization code is to adjust the relative weights of the beamlets in a determined number of beams so that the dose distribution is optimized. This optimization is guided by a suitable objective/cost function that has to be minimized. For example, this cost function could be design to assign a certain uniform dose to the tumor volume and at the same time constrain the maximum tolerable dose to critical structures/organs in the patient model. Optimization codes fall outside the scope of this study. Only the output results of such a code are needed in order to construct a suitable compensator to achieve the desired beam intensity modulation and the topic is not pursued any further.

The purpose of the CPS is to transform these maps of relative beamlet weights into compensator thickness maps (t_{ij}). This transformation is straight forward and is calculated with equation 4.1:

$$t_{ij} = \frac{\ln(w_{ij})}{\mu_{ij}} \qquad 4.1$$

where the indices (i,j) refer to the relative position of the beamlet in the particular beam. μ_{ij} indicates that the EAC depends on the size of the beamlet for a given beam energy and compensator material at index (i,j) in the field.

For beam the dose is then calculated as follows:

a) Start at the first location in the field and determine what the value of t_{11} is (equation 4.1).

b) For each this t-value, adjust the open PB to include the scatter and beam hardening using equation 3.5 in Chapter 3.

c) Rebin this PB into Cartesian co-ordinates.

d) Distribute this PB dose array in the current beam dose matrix (calculated in water).

e) Repeat steps b, c and d for all other locations in the field, accumulating the dose in each voxel of the current beam dose matrix.

The next step is to convert the beam weights (w_{ij}) into proper dose values (w_{ij} = 0.5 → 0.5 Gy or 50 % of dose maximum) and to compare the calculated compensated dose with the desired dose. This comparison would be done for a certain reference plane at depth, say 10 cm (where the beam weights have been produced).

The dose difference values at each location is then used to adjust the thickness of the compensator according to equation 4.2:

$$\delta t_{ij} = \frac{\ln\left(\frac{D_{ij}^{comp}}{D_{ij}^{desired}}\right)}{\mu_{ij}} \qquad 4.2$$

If the dose calculated under the compensator (D^{comp}) is too low, then δt_{ij} will be a negative number, and vice versa. After adjusting the thickness of each element of the compensator to $t'_{ij} = t_{ij} + \delta t_{ij}$ the dose is recalculated with the new thickness map (t'_{ij}), Equation 4.2 is based on a formalism of Shragge *et al.*, [4] where a similar formalism is used to optimize tissue compensators. The process is repeated (see figure 4.2) until the compensator delivers a dose distribution within a pre-determined error limit. A suitable output file is then produced for the compensator milling machine.

The rest of this section is devoted to the evaluation of the fast rebinning algorithm.

4.3 Methods

4.3.1 Rebinning a PB from cylindrical to Cartesian co-ordinates

Convolution/Superposition methods are preferably implemented using cartesian co-ordinates and the need for a fast rebinning algorithm was felt since the rebinning operation has to be performed in-line during the dose calculation.

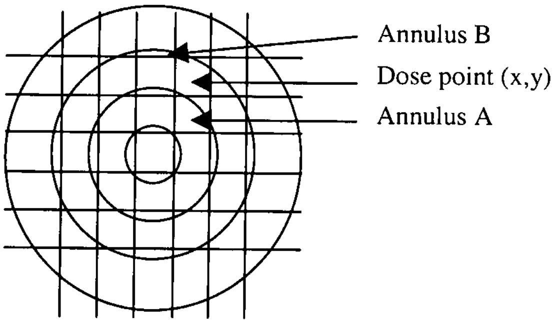

Figure 4.3. Cartesian grid superimposed on a cylindrical grid.

The rebinning process progresses as follows:

a) Each annulus has an effective radius, reff(i) (Chapter 3).

b) The geometric center of the dose point on the Cartesian grid is (x,y)

c) Construct radius $r = \sqrt{(x^2 + y^2)}$.

d) Determine between which two effective radii, e.g. reff(i) and reff(i+1) the radius, r, lies.

e) Interpolate the dose linearly between the corresponding annuli and assign the resulting dose to the dose point.

f) Do so over the first quadrant of the cartesian grid and use the symmetry properties of the Cartesian dose grid to reflect the dose values to the rest of the grid.

This method of rebinning is somewhat crude, but fast (approximately 50 times faster than an area overlap method). It is not as accurate as the other more computationally expensive methods, but the accuracy is regained in a further step of the procedure based upon the results of the matching of the normalized depth dose curves for a set of square fields to that of the corresponding normalized PB depth dose curves. During this step of the procedure the cartesian PB dose profiles at any given depth are scaled with a linear function, f, of compensator thickness that adjusts the dose values in the plane at that depth according to equation 4.3.

$$(D_{ijk})_{scaled} = (1 - f * k)D_{ijk} \qquad 4.3$$

Where k is the depth index and

$$f = a + bt \qquad 4.4$$

The values of function f, is small and depends to a certain degree on the field size.

The empirically determined parameters, a and b, describe the variation of constant f with field size. Table 4.1 shows these parameters and the field sizes for which they were derived.

Table 4.1 Parameters a and b for different field sizes:

Field size (S) (cm)	a	b
2	0.0000	-0.00000
3	0.0000	-0.00000
5	0.0000	-0.00000
10	0.0000	-0.00000
15	0.0020	-0.00020
20	0.0027	-0.00031
30	0.0027	-0.00031

Normalized depth dose comparison had shown relative dose discrepancies of up to 3% for fields from 15x15 cm^2 and larger. Applying the correction factor values in table 4.1 improved the match of depth dose curves at 6, 8 and 15 MV to within a fraction of one percent.

4.3.2 Testing the rebinning algorithm

The rebinning method was tested for three cases. Case I: Normalized depth dose data for 6, 8 and 15 MV beam models were calculated for a range of square open fields ranging from 2x2 cm^2 to 30x30 cm^2. These data were calculated with a), DOSXYZ b), cylindrical PBs using the reciprocity theorem and c) cartesian PBs using the superposition method. The respective data were compared to evaluate the shape of the depth dose curves. Case II: Normalized depth dose data were also calculated by adjusting the open PB to include the scatter and beam hardening for a 5 cm thick brass absorber. These data were compared to normalized depth dose data calculated with the corresponding cartesian PB and with depth dose data for an actual PB derived after traversing 5 cm of brass at 8 MV. Case III: Normalized dose profile data for 6, 8 and 15 MV were compared between the Cartesian PB (using the superposition dose calculation method) and DOSXYZ for a range of square beam sizes ranging from 2x2 cm^2 to 25x25 cm^2.

All test cases were performed for parallel beams in water. The DOSXYZ voxels had dimensions of 0.5x0.5 cm^2 in the xy-plane. Its depth increments corresponded to those used for the PB (see Chapter 3). The electron and photon energy cut-offs corresponded to that for the EGSnrc simulations during the generation of the PB data.

4.4 Results and Discussion

Normalized depth dose data for 6, 8 and 15 MV beam energies are shown for a range of field sizes in figures 4.4, 4.5 and 4.6. In each graph the PDD curve for the cylindrical PB was obtained using the reciprocity theorem for the corresponding circle field. The PDD curves for the Cartesian PB was obtained from superposition calculations over the field size of interest. The DOSXYZ generated PDD curves were obtained from full MC simulations over the field size of interest. The beam sources used the energy spectra as shown in figure 1.1 in Chapter 1. The deviations of the relative MC dose compared to the PB and Cartesian data are due to statistical variance on the MC data. It is more apparent for the larger fields, since many more histories are needed to obtain the same level of variance as e.g. the 2x2 cm^2 to 5x5cm^2 fields. The rebinning scheme could successfully reproduce depth dose data from the original cylindrical PB as derived in water. These depth dose data matched the DOSXYZ generated data. The PB can also be adjusted to include the effect of compensators e.g. scatter and beam hardening. Figure 4.7 illustrates the rebinning scheme to reproduce the relative depth dose curves for an 8 MV beam with a brass attenuator with a thickness of 5 cm. This PB has been derived from an EGSnrc MC simulation after the original photon beam has traversed 5 cm of brass. This serves a dual purpose namely to show that a), the open PB can be modified to include the effects of beam hardening and scatter for a 5 cm thick brass absorber and b), that the rebinning operation on this modified PB can reproduce the resulting relative depth dose curves for the field sizes shown.

As a final validation, sets of dose profiles for 6, 8 and 15 MV beams derived from the rebinned PBs with the superposition method are compared with dose profiles from DOSXYZ in figures 4.8, 4.9 and 4.10.

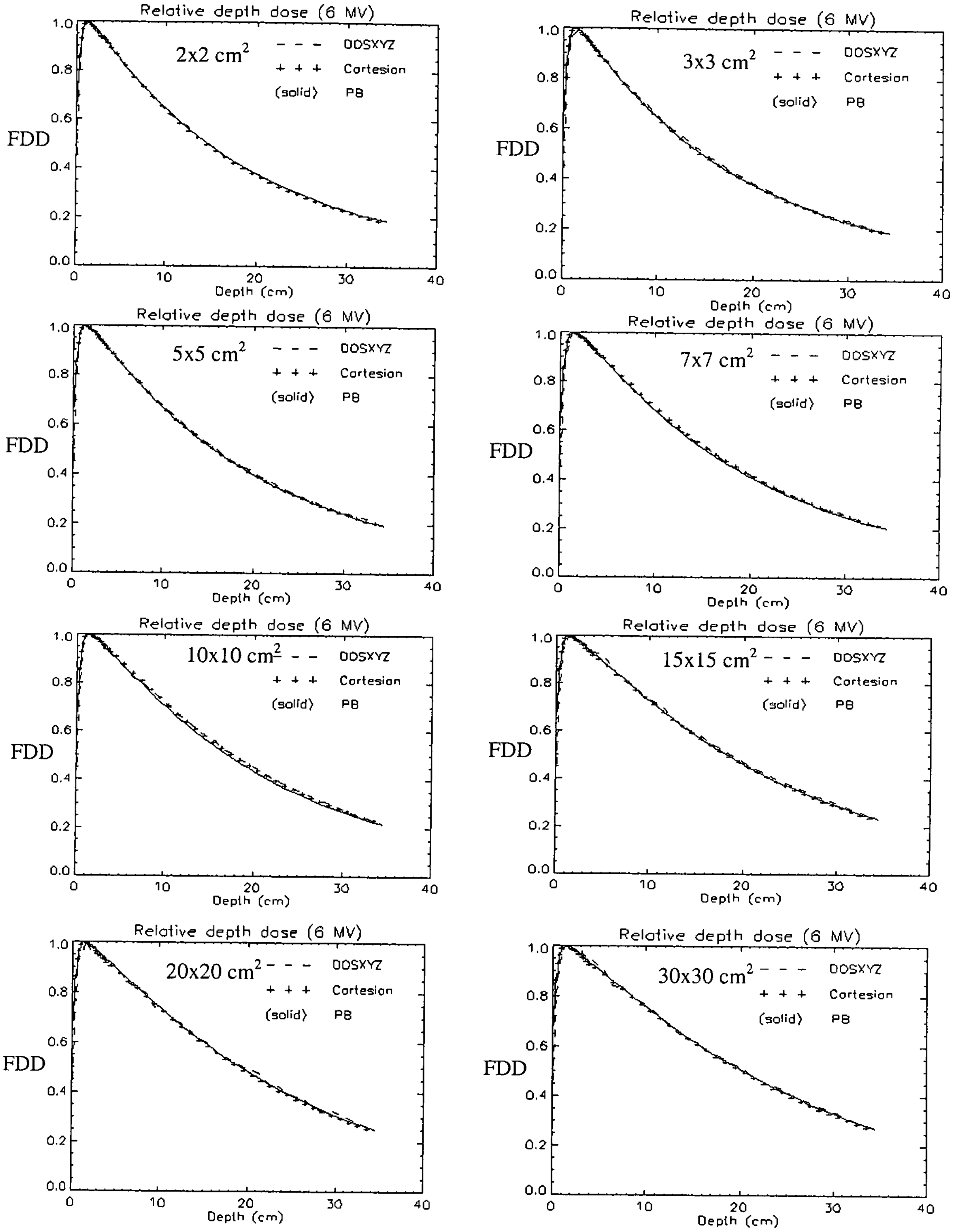

Figure 4.4: Comparative fractional depth dose curves for different field sizes at 6 MV. Curves are shown for DOSXYZ, cylindrical PB and Cartesian PB.

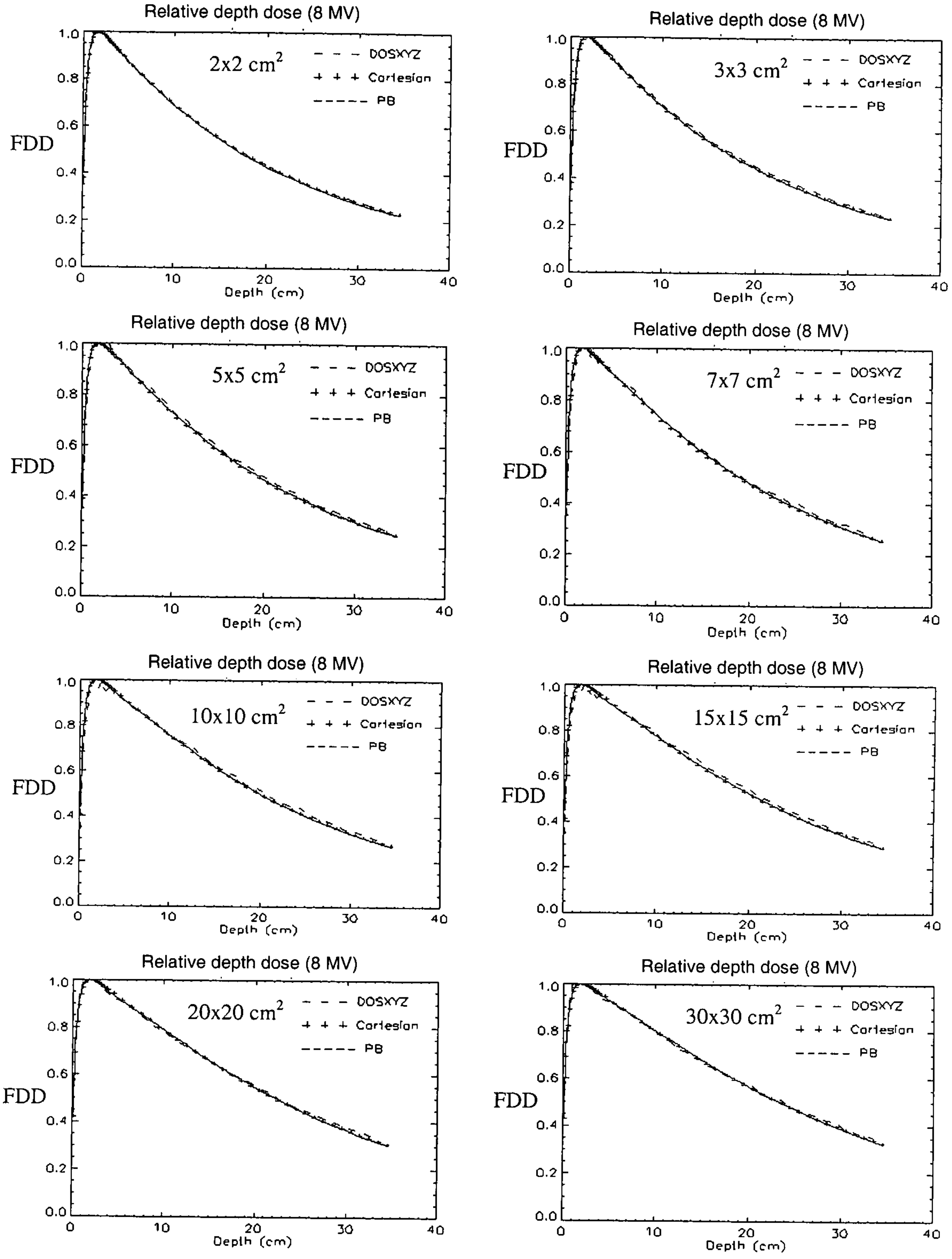

Figure 4.5 Comparative fractional depth dose curves for different field sizes at 8 MV. Curves are shown for DOSXYZ, cylindrical PB and Cartesian PB.

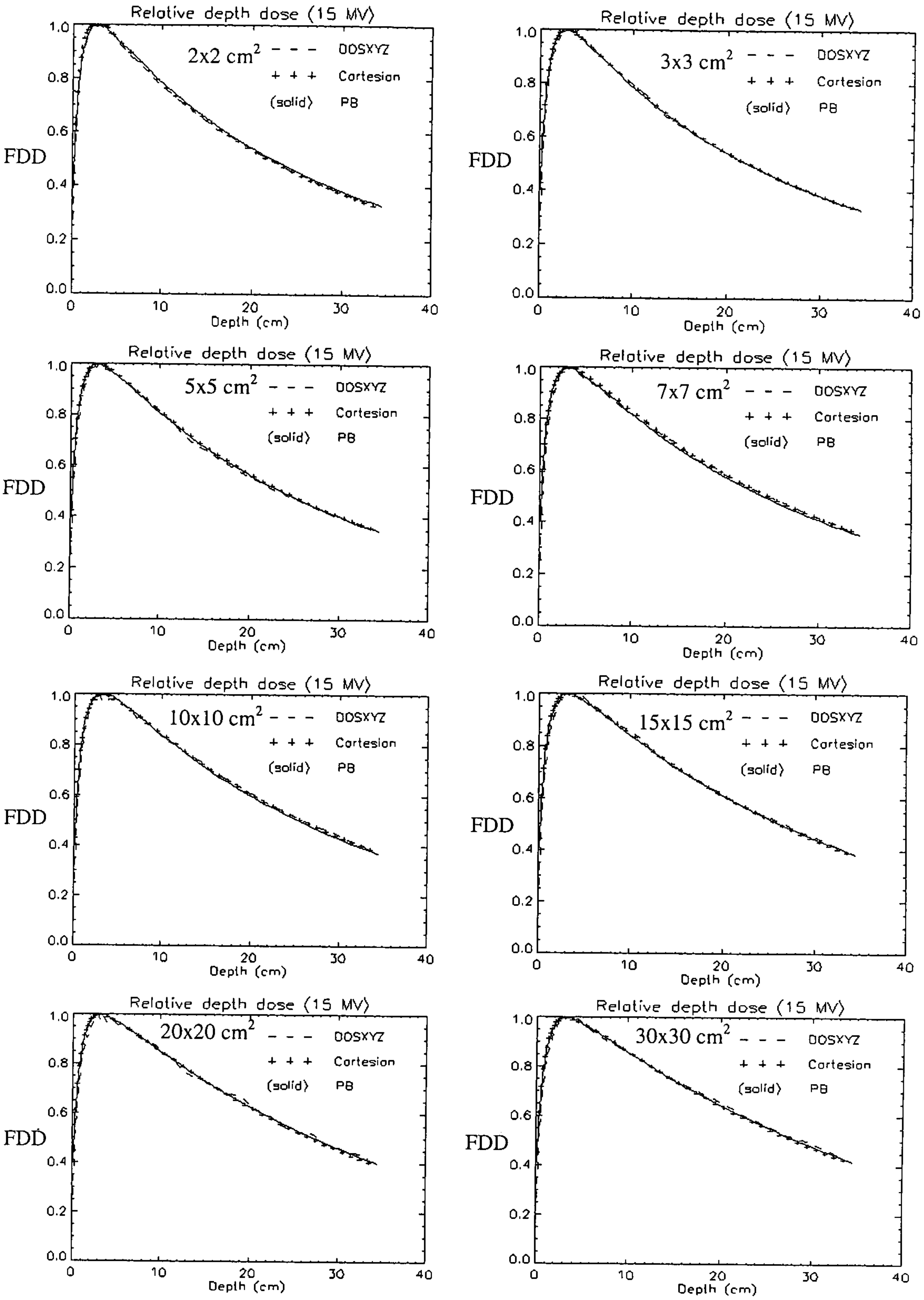

Figure 4.6: Comparative fractional depth dose curves for different field sizes at 15 MV. Curves are shown for DOSXYZ, cylindrical PB and Cartesian PB.

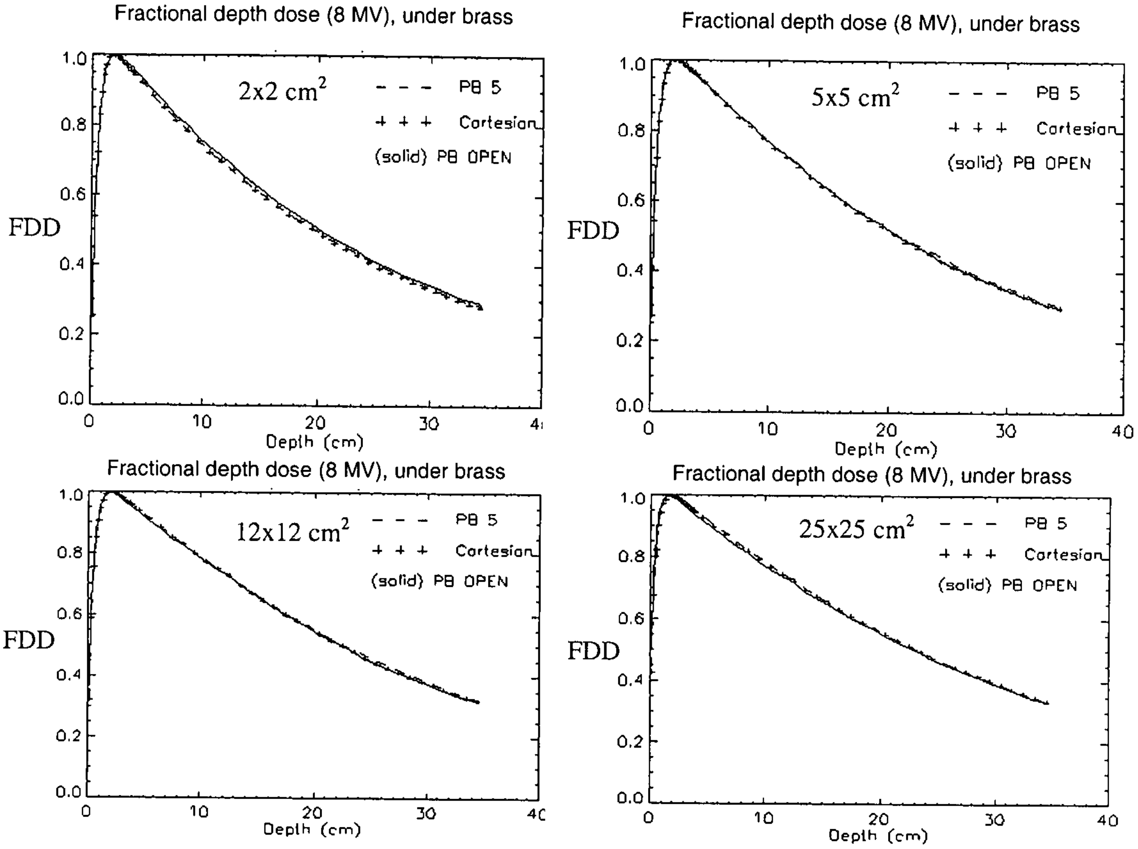

Figure 4.7: Comparative fractional depth dose curves for different field sizes at 8 MV under brass. The solid line: Fractional depth dose after cylindrical PB was adjusted for scatter and beam hardening for a 5 cm brass absorber. (+ + +) -line: The cartesian PB, rebinned from the cylindrical PB. (- - -) -line: The real attenuated PB after traversing 5 cm of brass.

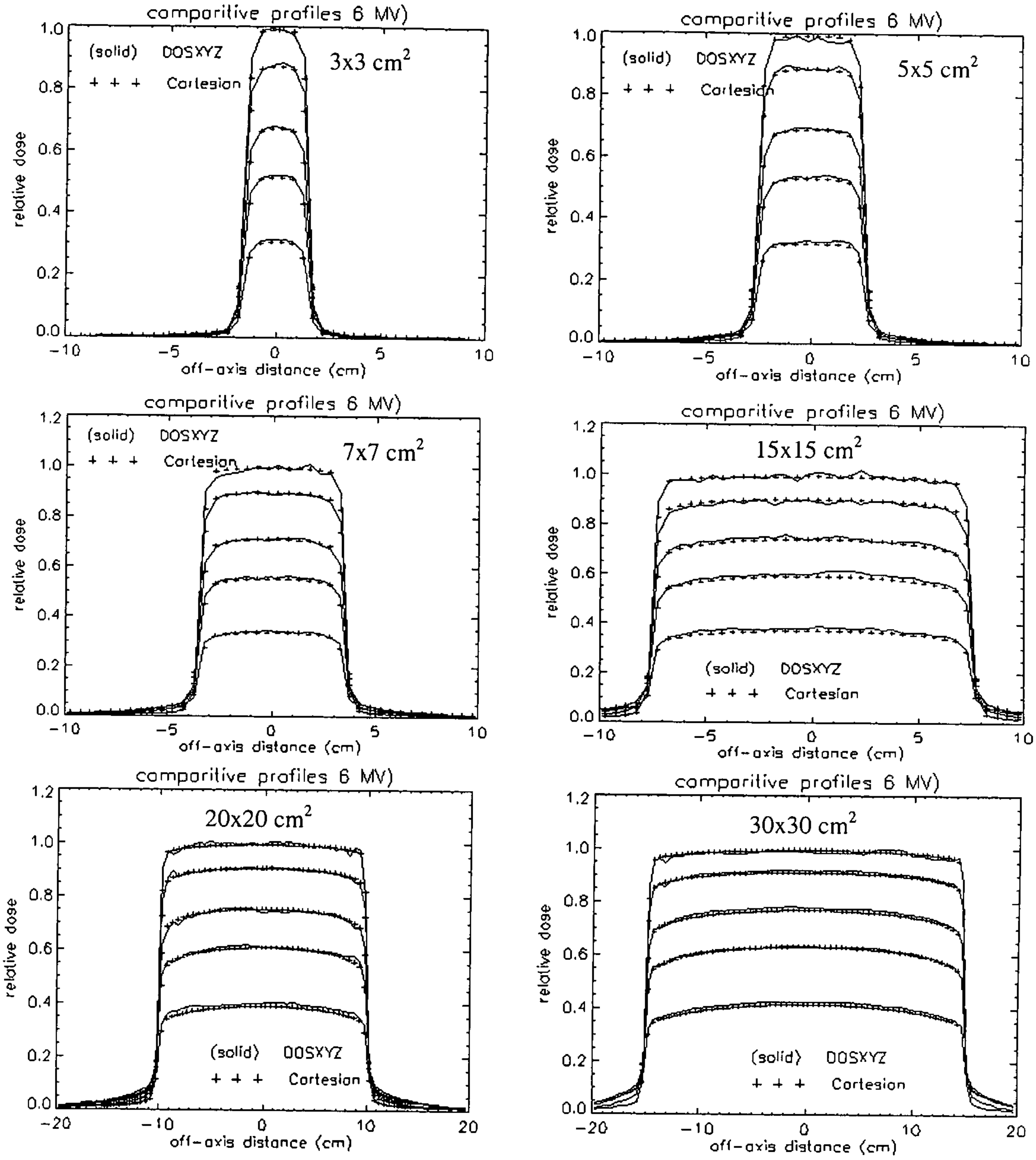

Figure 4.8. Comparison of dose profiles generated by a) DOSXYZ and b) Superposition of the cartesian PB over the indicated square field sizes for 6 MV.

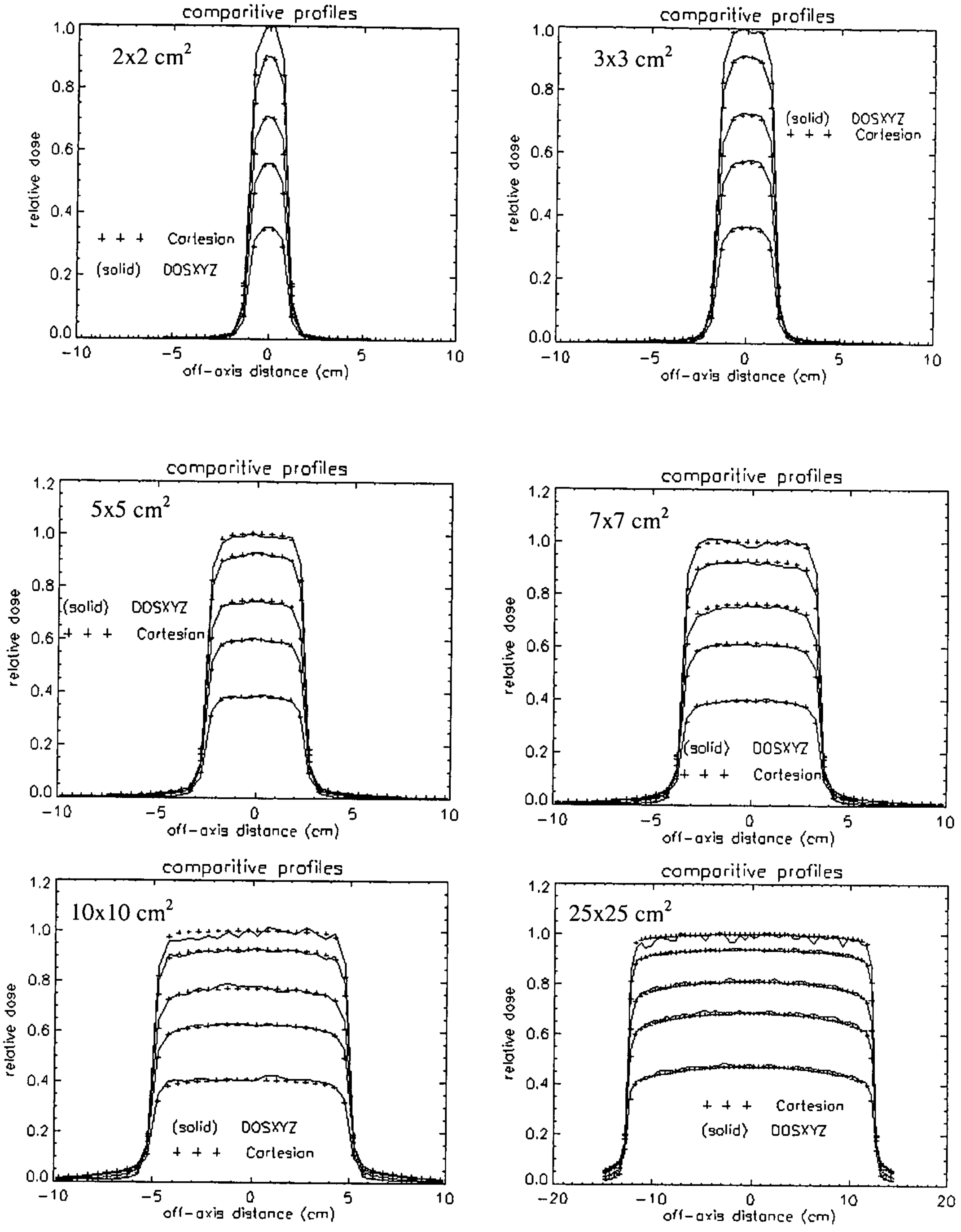

Figure 4.9. Comparison of dose profiles generated by a) DOSXYZ and b) Superposition of the cartesian PB over the indicated square field sizes for 8 MV.

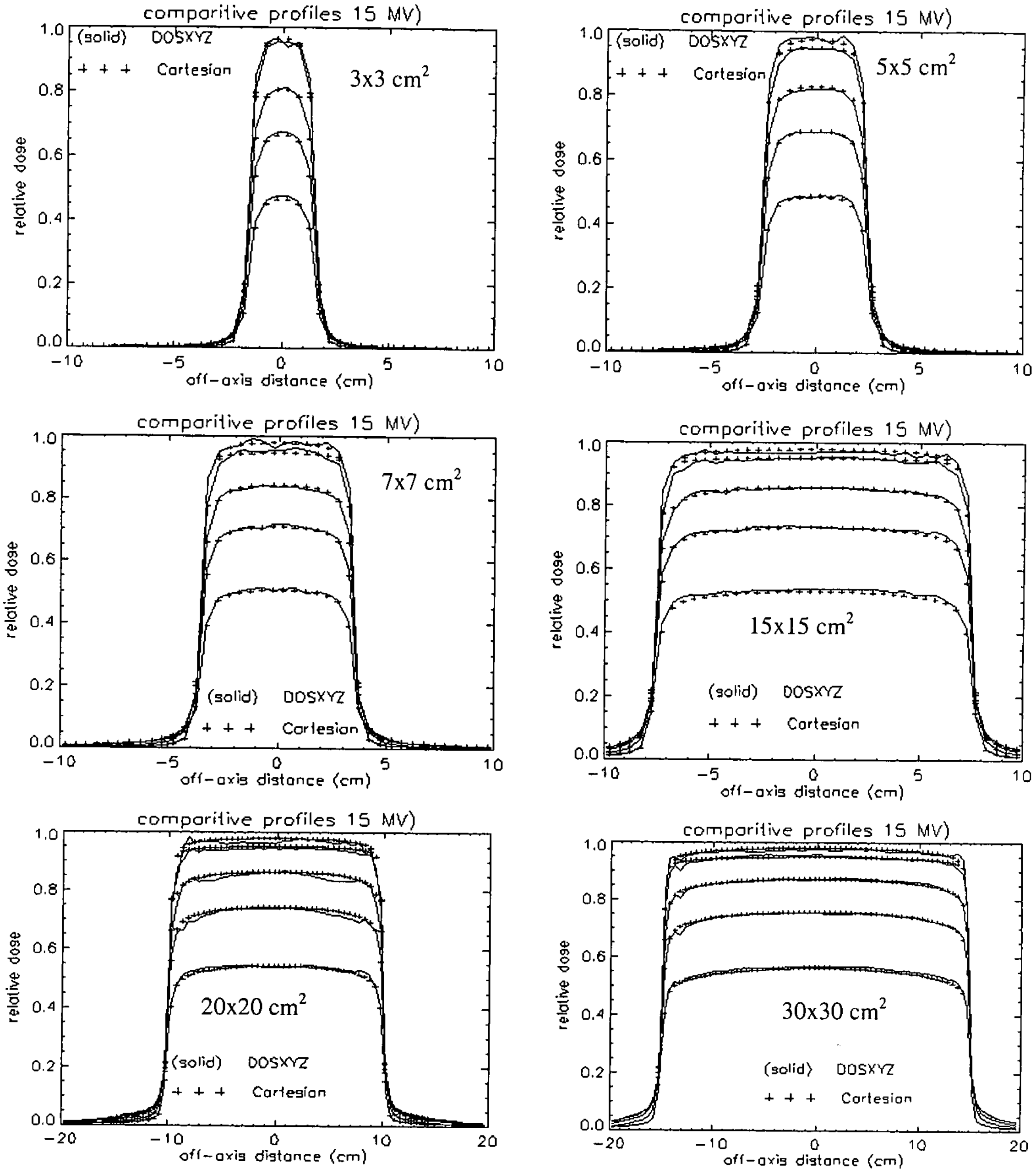

Figure 4.10. Comparison of dose profiles generated by a) DOSXYZ and b) Superposition of the cartesian PB over the indicated square field sizes for 15 MV.

The dose profiles for the smaller fields are in excellent agreement with the DOSXYZ results e.g. the 3x3 cm^2 and 5x5 cm^2 fields. For the larger fields the noise on the MC data have a significant influence on the comparison of the data especially near the surface. Encouraging, is the dose profiles in the penumbra regions that are in excellent agreement over the field sizes studied. At this stage only the relative dose curves were compared. The aim of this exercise was to show that the rebinning method, can with necessary small adjustments (factors in table 4.1) deliver satisfactory results when compared to voxel based MC codes such as DOSXYZ.

The 3-D dose distribution calculations data took in the order of 1.5 hours on a 1.4 GHz, Pentium III Intel Celeron machine for a field size of 30x30 cm^2, over 51 depth intervals. The voxel dimensions in the xy-plane was 0.5x0.5 cm^2 resulting in a total of 183600 voxels.

4.5 Conclusion

From these verification data it is evident that the compensator planning system, which employs a fast, accurate and simple rebinning algorithm, is capable of reproducing accurate relative depth dose values from cylindrical PBs that have been modified to include the effect of transmission through a brass material. It can match DOSXYZ water based dose profiles and agrees well even in the beam penumbra region. Based on this evidence this compensator planning system can be used to design compensators which will include the effects of beam hardening and relative scatter. The compensator shape is derived from a prescribed dose distribution in water. The next step is to evaluate the planning system performance on simple compensator models by comparing the dose distribution under the compensator model, that has been designed by the CPS, with the distribution obtained with a full DOSXYZ simulation, incorporating the compensator model. This is the focus of Chapter 5. The compensators derived with this planning system can ultimately be used in full MC calculations for IMRT purposes after incorporating some additional necessary features, such as beam divergence, into the model.

4.6 References

[1]A. Ahnesjö, M. Saxner, and A. Trepp, ‘ A pencil beam model for photon dose calculation.’ Med. Phys. **19**, 263 – 273 (1991).

[2] A. Eklöf, A. Ahnesjö, and A. Brahme, ‘ Photon beam energy deposition kernels for inverse Radiotherapy planning.’ Acta Oncol. **29**, 447 – 454 (1989).

[3] S. Rathee, B.A. Mclean, and C. Field, ‘ An improved method for rebinning kernels from cylindrical to Cartesian coordinates.’ Med. Phys. **20**, 1343 - 1351 (1993).

[4] P.C. Shragge, and M.S. Patterson, ‘ Improved method for the design of tissue compensators.’ Med. Phys. **8**, 885 – 891 (1981).

CHAPTER 5

Modeling dose distributions for simple compensators with a pencil beam based compensator planning system

5.1 Introduction

Compensators as an alternative to multileaf collimators can be used to modulate the energy fluence over the aperture of arbitrary shaped photon fields. In Chapter 3, a study was conducted aiming at characterizing scatter dose and beam hardening from slabs of compensator materials. It was found that the absorbed dose profiles of an open PB could be altered to include these effects as a linear function in material thickness. In Chapter 4 the CPS, using a simple, fast rebinning algorithm, was introduced and was benchmarked for open fields and a 5 cm thick brass slab against DOSXYZ. The rebinning test cases in that Chapter were mainly designed to verify depth dose curves and beam profiles for various field sizes at 6, 8 and 15 MV beam energies. In this Chapter a step wedge compensator will be used to verify the algorithm for a set of fields at 6, 8 and 15 MV beam energies for wax, aluminum, brass, copper and lead materials. The relative dose for each case will be compared with similar DOSXYZ MC simulations in a plane perpendicular to the beam axis located at a depth of 10 cm in water. A simple correction function is introduced to model side penetration through compensator elements. Finally, the ability of the CPS to design a compensator that can produce a step-like dose distribution is illustrated.

5.2 Methods

This study involved the analysis and comparison of 3D dose distributions, calculated in water, using the CPS and the DOSXYZ Monte Carlo (MC) code. The aim was to evaluate the performance of the algorithm developed in Chapter 3. The relative absorbed dose was calculated by the CPS using superposition of the PB dose distribution. This was done by three different methods: In the first method, a broad beam EAC was used to weigh the open PB. In the second method the same procedure is followed in combination with a correction function for side penetration. In the third method, the EACs are determined as in Chapter 2 and are then used together with the correction function for side penetration and with the PB corrected for scatter and beam hardening as described in Chapter 3.

5.2.1 DOSXYZ simulations

A rectangular water phantom with dimensions of 40x40x25 cm^3 was set up in the EGS4 based DOSXYZ MC code (figure 5.1). The voxel dimensions was set to 0.5x0.5 cm^2 in the xy-plane of the water phantom. In order to speed up the simulations the phantom contained only three 1 cm thick scoring planes in the z-direction centered at 4.5, 9.5 and 14.5 cm. An additional scoring plane 0.2 cm thick was centered at 1.9 cm depth. The following transport parameters were chosen: ECUT = 0.700 MeV, PCUT = 0.010 keV. PRESTA was invoked. Enough histories were chosen to reduce the statistical variance to less than about one percent through at least 80 percent of the field size volume in the phantom. The beam sources used the same energy spectra (6, 8 and 15 MV) as shown in Chapter 1, and were parallel with the CAX coinciding with the z-axis of the water phantom. Three sets of fields were used in a series of simulations that included square fields with side lengths of 5, 10 and 20 cm. For each field a set of five compensator materials were used as mentioned. The compensator shape was scaled according to field size. It was in the shape of a step wedge consisting of 5 steps. For a 10x10 cm^2 field each step was 2 cm wide and for a 5x5 cm^2 field, each step was set 1 cm wide etc. The thicknesses of the steps were 0, 1, 2, 3 and 6 cm. The compensator was included in the DOSXYZ geometry at a retractal distance of 33 cm from the water surface as shown in figure 5.1.

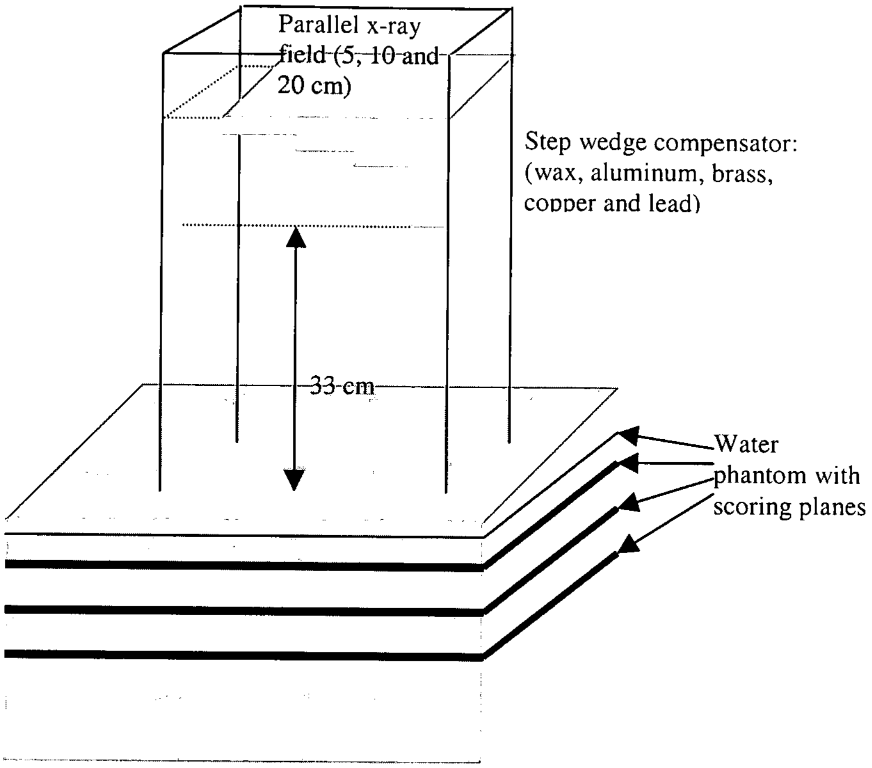

Figure 5.1. DOSXYZ water phantom with step wedge shaped compensator at 33 cm retractal distance.

The thickness of the water phantom was chosen as 25 cm to correlate with an average patient thickness.

5.2.2 CPS calculations

Dose calculations corresponding to the DOSXYZ cases, were performed with the compensator planning system (CPS). It was calculated in a water phantom for the same field sizes, beam energies and compensator materials as in the DOSXYZ MC simulations, using the three mentioned methods. The relative absorbed dose were then analyzed at the same plane depths as that for DOSXYZ. A typical calculation for a 20x20 cm^2 field took in the order of 12 minutes on a Pentium III, 1.0 GHz PC with the CPS: For methods one and two the broad beam EACs were determined as follows: For the 5x5 cm^2

field the broad beam EAC values were taken from Chapter 2 for the 5x5 cm^2 field at 10 cm depth. For the 10x10 cm^2 and 20x20 cm^2 fields broad beam EAC values were calculated with DOSXYZ at 10 cm depth in water. This was done for each compensator material and is shown in table 5.1. The geometry was a 40x40x40 cm^3 water phantom, with a single 0.5x0.5x1.0 cm^3 dose scoring voxel at a depth of 10 cm. Parallel beams were used with energy spectra corresponding to 6, 8 and 15 MV respectively. The transport control parameters (ECUT, PCUT etc.) were the same as those in Chapter 2. A dose ratio was used to calculate these broad beam EACs. The first was the dose with no absorber in the relevant beam and the second for a 1 cm thick slab of absorbing material, (for wax the thickness was 4.0 cm.) The dose compensation depth was chosen at 10 cm and the EAC was also calculated for this depth. This depth was chosen since this can be regarded as an average tumor depth. In relation to this, the dose in the planes centered on 4.5 and 14.5 cm depth would give an indication of the degree of compensation variation over this 10 cm thick 'tumor' volume for the EAC chosen at 10 cm depth.

5.3 Results and Discussion

The DOSXYZ calculated broad beam EAC values are shown in table 5.1. These values were used for the dose calculations with the CPS using methods 1 and 2.

Table 5.1 EAC values calculated from DOSXYZ simulations at 10 cm depth in water.

Field size		**10x10 cm^2**			**20x20 cm^2**	
Energy	**6 MV**	**8 MV**	**15 MV**	**6 MV**	**8 MV**	**15 MV**
wax	0.0298	0.0328	0.0256	0.0270	0.0328	0.0305
aluminum	0.111	0.101	0.085	0.105	0.111	0.095
brass	0.360	0.337	0.286	0.286	0.285	0.285
copper	0.338	0.336	0.303	0.296	0.291	0.315
lead	0.547	0.532	0.535	0.531	0.534	0.555

The method for obtaining these EACs is certainly not as accurate as the one used in Chapter 2. The aim here was to obtain a reasonable estimate for broad beam EACs at the indicated beam energies and field sizes in water. The relative dose profiles under the step shaped compensator were calculated for 5x5 cm^2, 10x10 cm^2 and 20x20 cm^2 fields. In figures 5.2 to 5.4 the relative dose profiles are shown on the left at depths of 2, 5, 10 and 15 cm for the first and third methods in comparison with the DOSXYZ simulated relative dose profiles. The graphs on the right show the local percentage difference between the relative dose profiles calculated by all three methods, and the DOSXYZ generated profiles as the reference data, at a single depth of 10 cm.

The broken line traces out the percentage differences for calculation method one where the open PB is used with the broad beam EAC. The triangles show the percentage difference for method 2, still using the broad beam EAC calculations, but now adjusted for side penetration through the compensator. The solid line shows the data obtained with the open PB after it was modified as in Chapter 3 (method 3) to include scatter and beam hardening, but also including the side penetration correction. This correction will now be discussed.

5.3.1 Relative dose profiles for 5x5 cm^2 fields

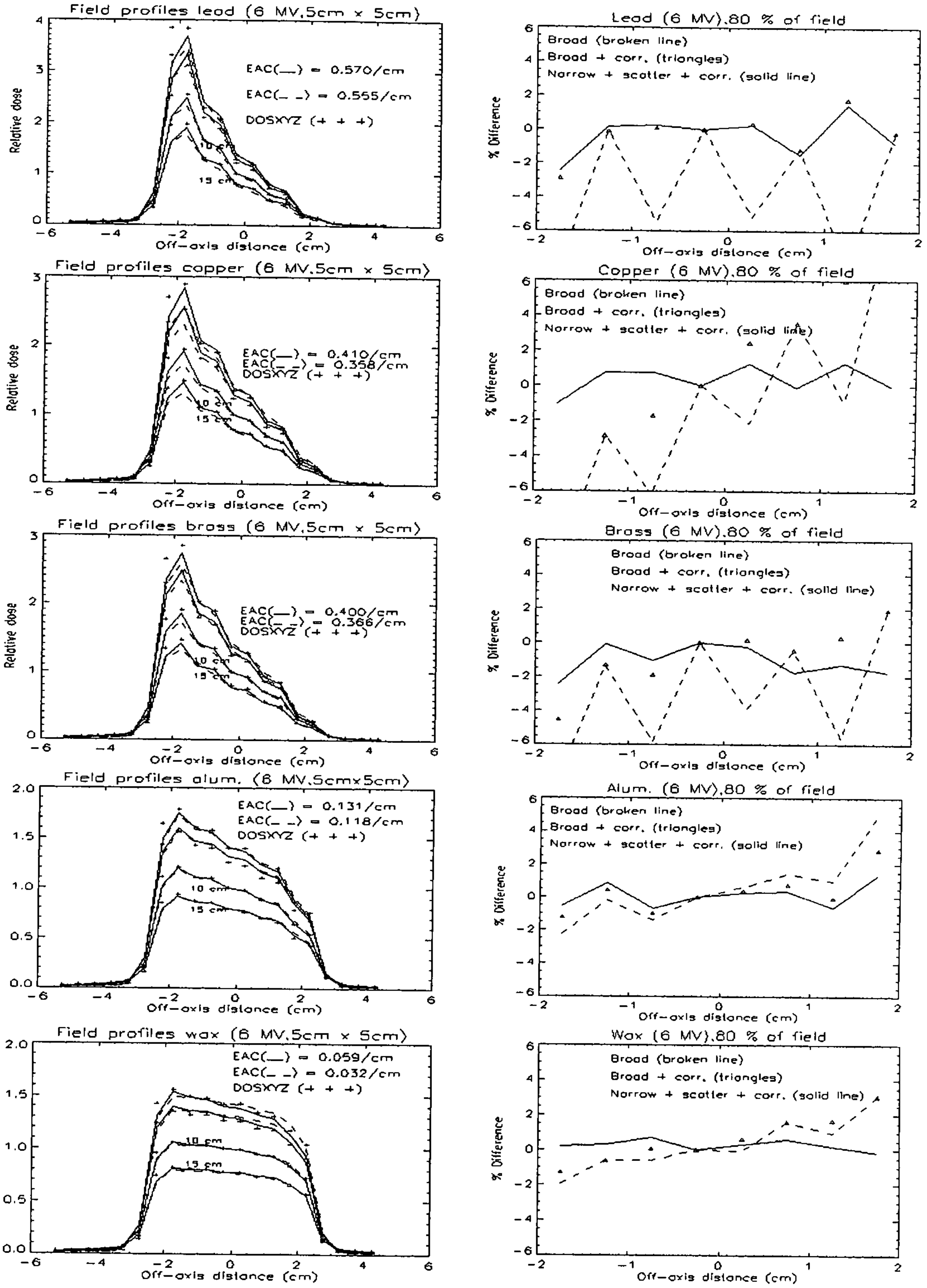

Figure 5.2a left: Relative dose profiles at 6 MV for method one (Solid line) and three (dashes) and DOSXYZ.(+ + +) Right: Local dose percentage difference between all three methods and DOSXYZ dose profile as standard, at a depth of 10 cm. The variance on the DOSXYZ data was between 0.3 and 0.5 percent.

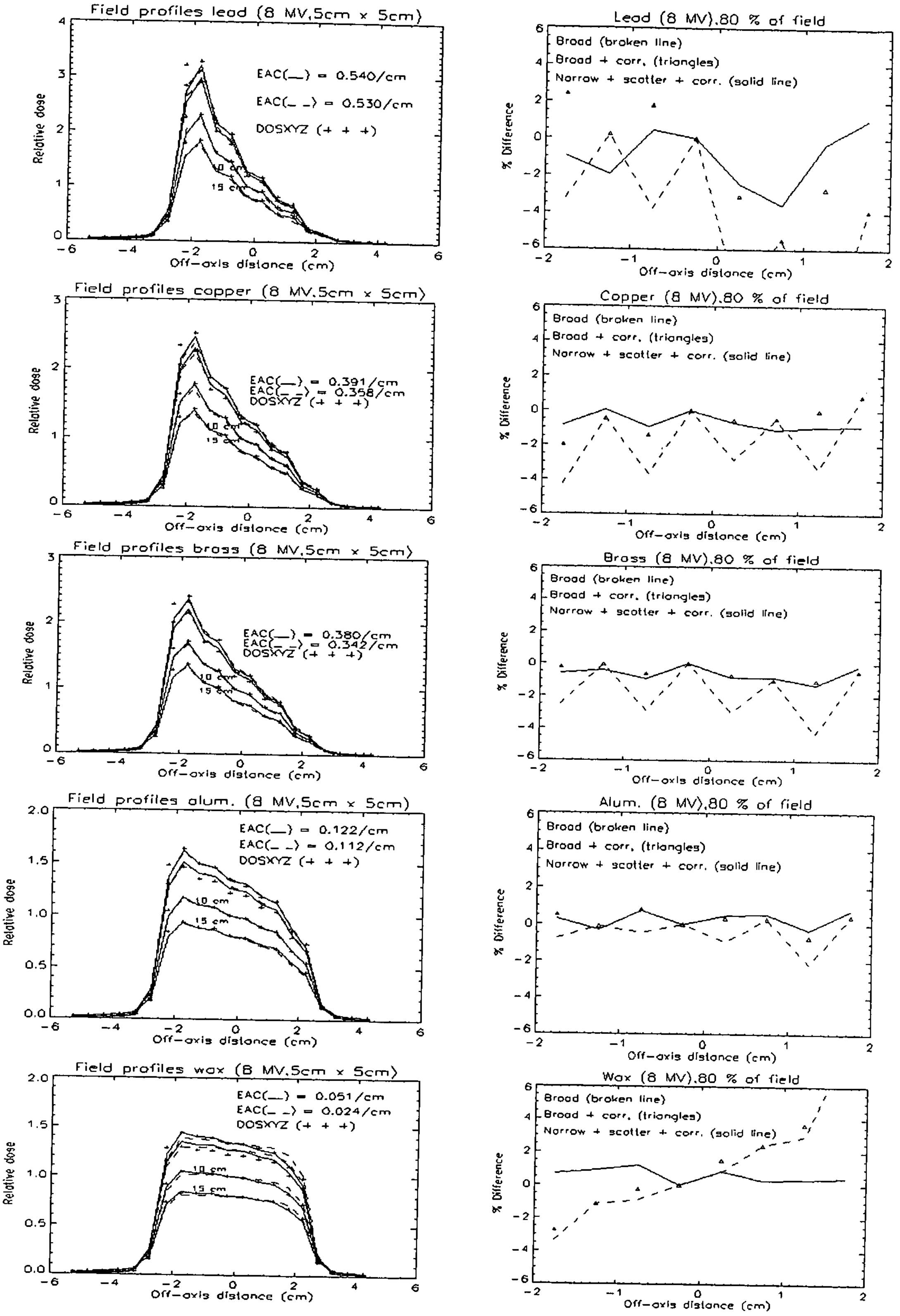

Figure 5.2b left: Relative dose profiles at 8 MV for method one (Solid line) and three (dashes) and DOSXYZ (+ + +) Right: Local dose percentage difference between all three methods and DOSXYZ dose profile as standard, at a depth of 10 cm. The variance on the DOSXYZ data was between 0.3 and 0.5 percent.

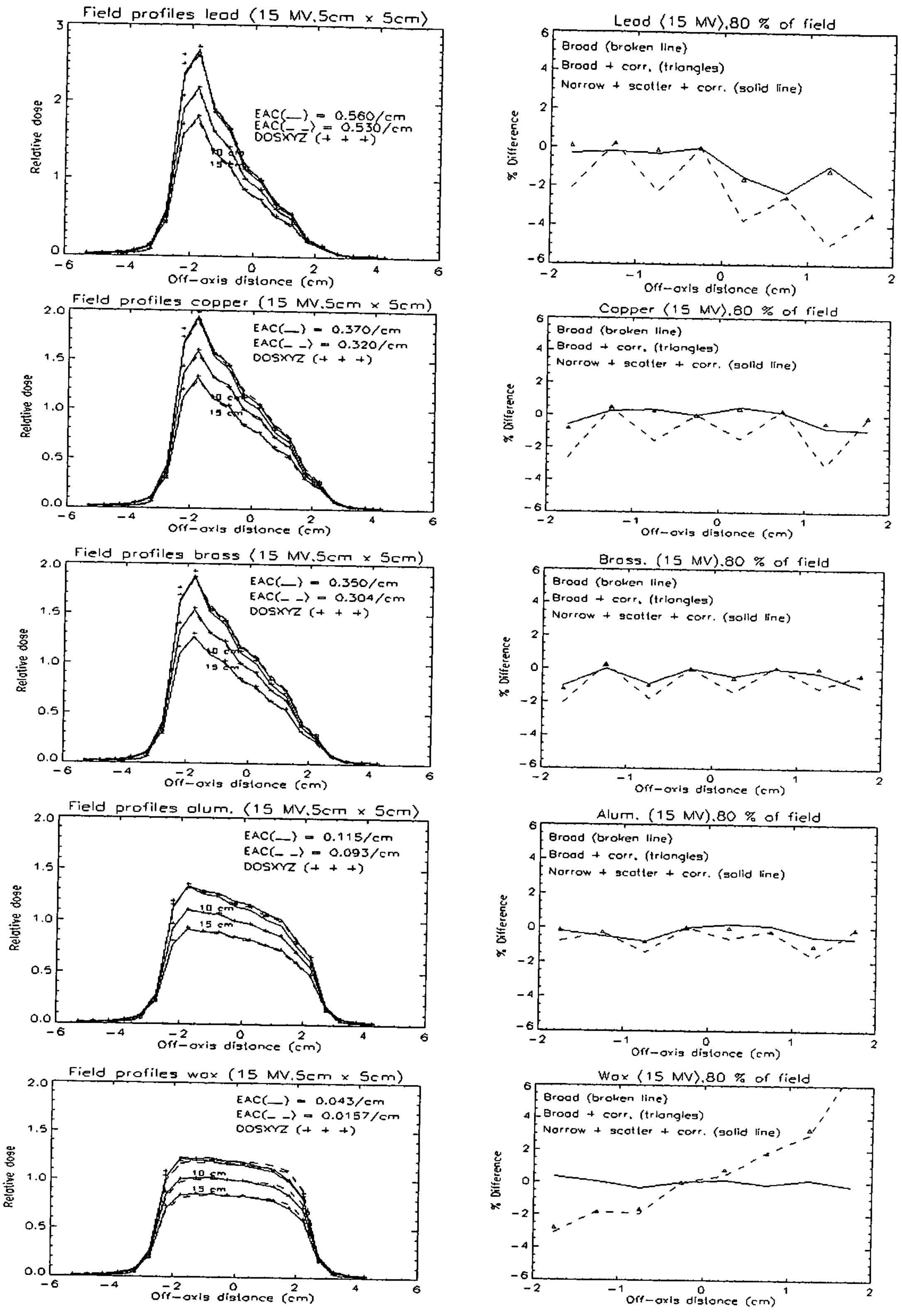

Figure 5.2c left: Relative dose profiles at 15 MV for method one (Solid line) and three (dashes) and DOSXYZ (+ + +) Right: Local dose percentage difference between all three methods and DOSXYZ dose profile as standard, at a depth of 10 cm. The variance on the DOSXYZ data was between 0.3 and 0.5 percent.

5.3.2 Relative dose profiles for 10x10 cm^2 fields

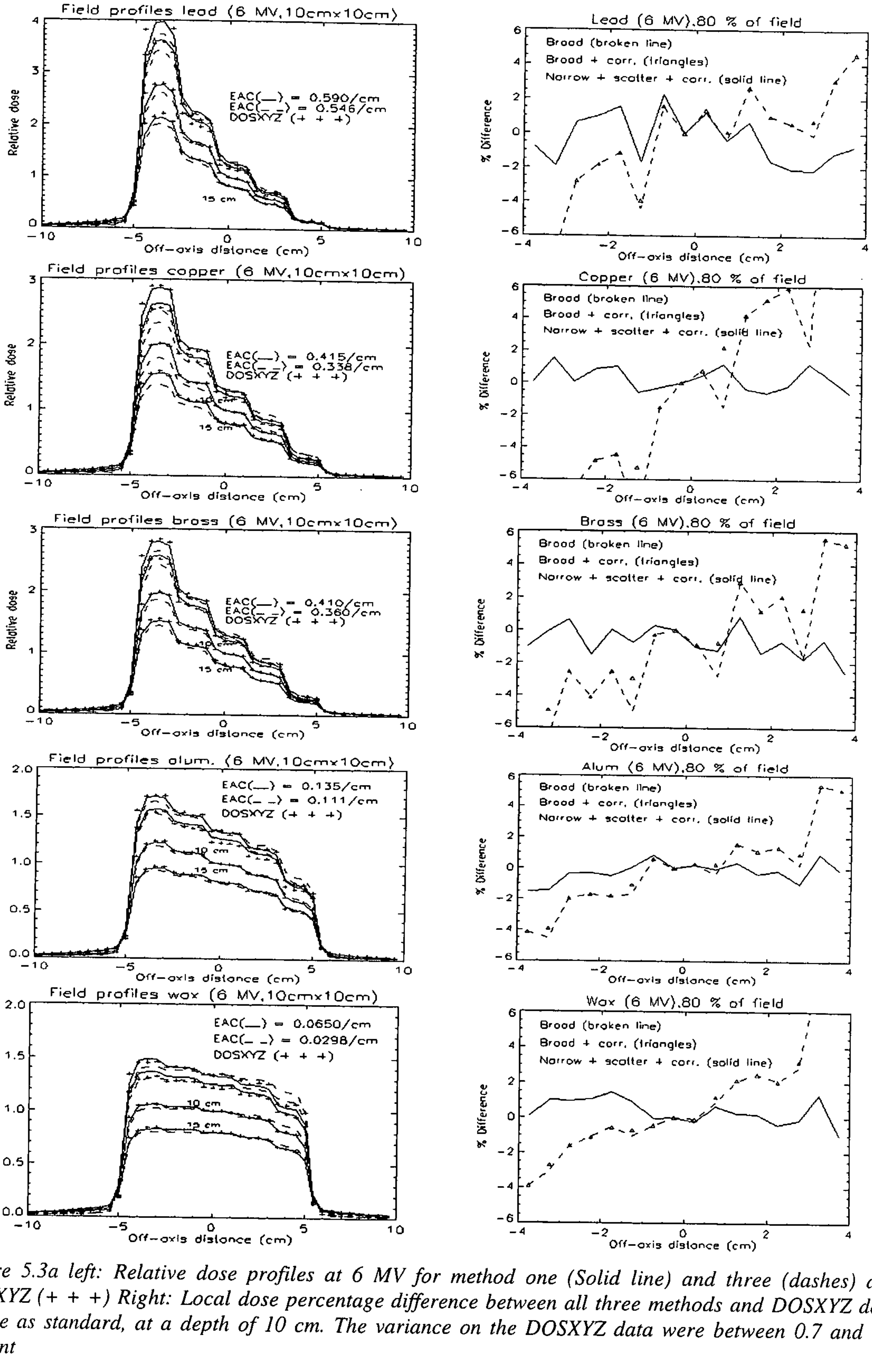

Figure 5.3a left: Relative dose profiles at 6 MV for method one (Solid line) and three (dashes) and DOSXYZ (+ + +) Right: Local dose percentage difference between all three methods and DOSXYZ dose profile as standard, at a depth of 10 cm. The variance on the DOSXYZ data were between 0.7 and 1.1 percent

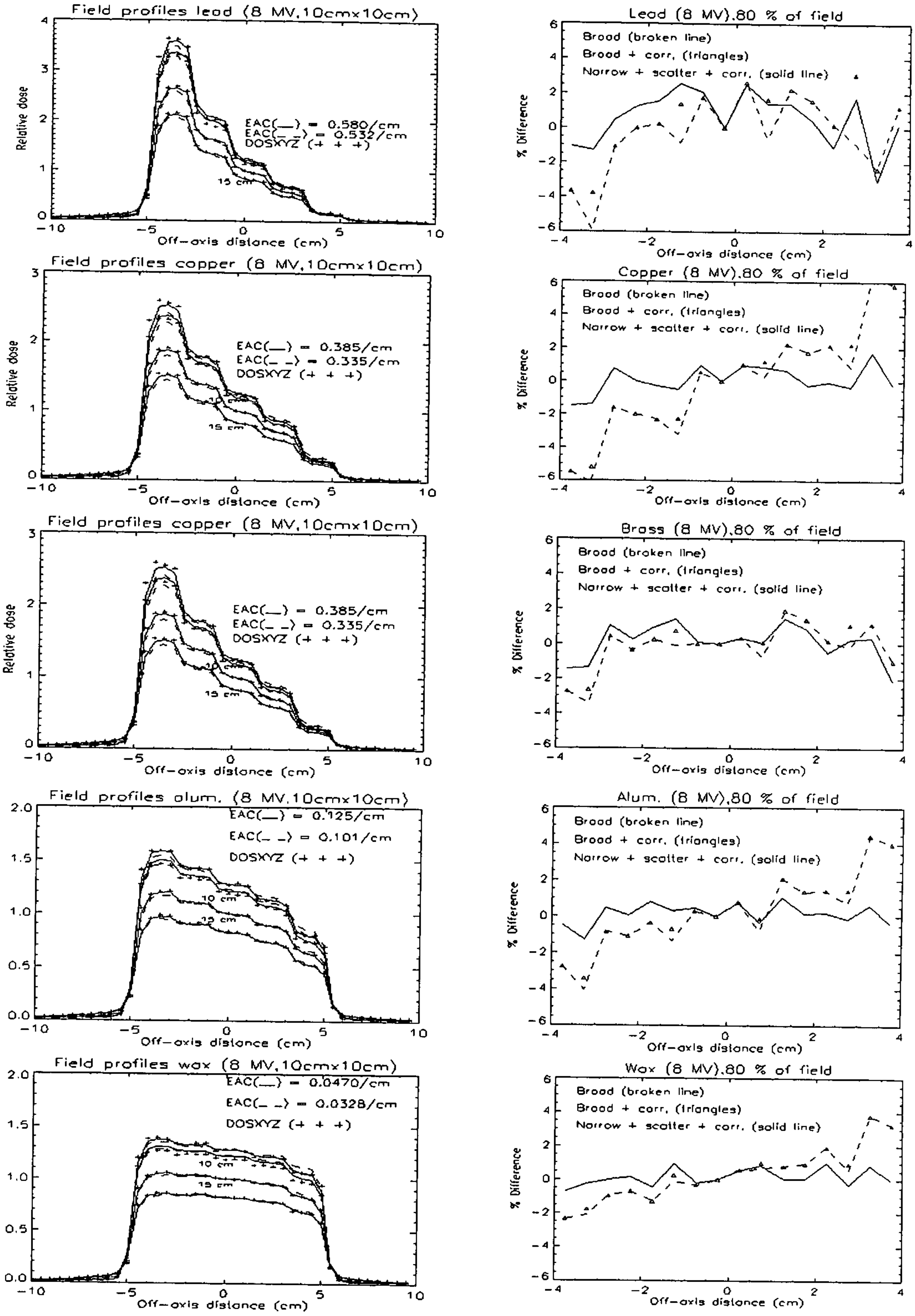

Figure 5.3b left: Relative dose profiles at 8 MV for method one (Solid line) and three (dashes) and DOSXYZ (+ + +) Right: Local dose percentage difference between all three methods and DOSXYZ dose profile as standard, at a depth of 10 cm. The variance on the DOSXYZ data were between 0.7 and 1.1 percent

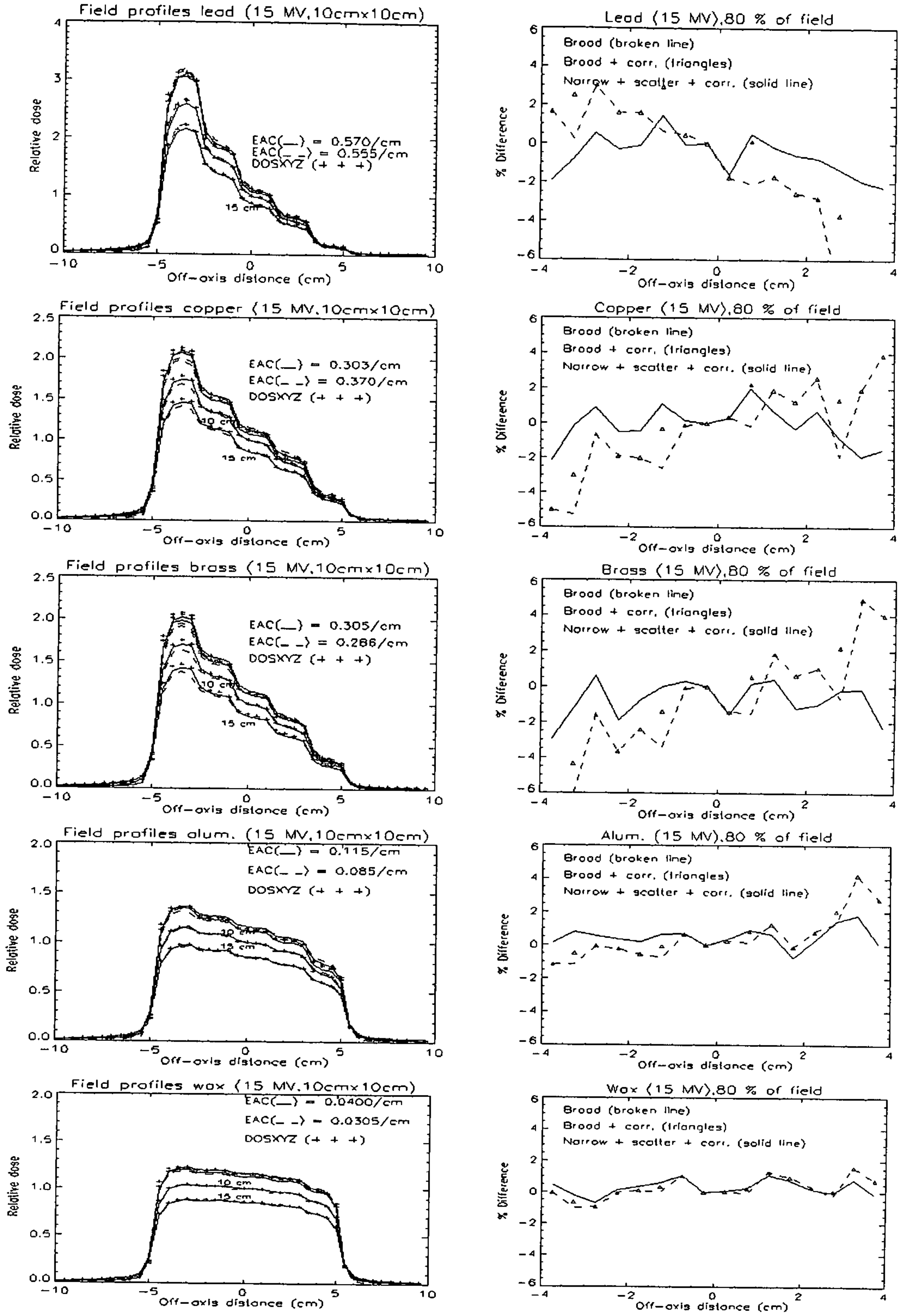

Figure 5.3c left: Relative dose profiles at 15 MV for method one (Solid line) and three (dashes) and DOSXYZ (+ + +) Right: Local dose percentage difference between all three methods and DOSXYZ dose profile as standard, at a depth of 10 cm. The variance on the DOSXYZ data were between 0.7 and 1.1 percent

5.3.3 Relative dose profiles for 20x20 cm^2 fields

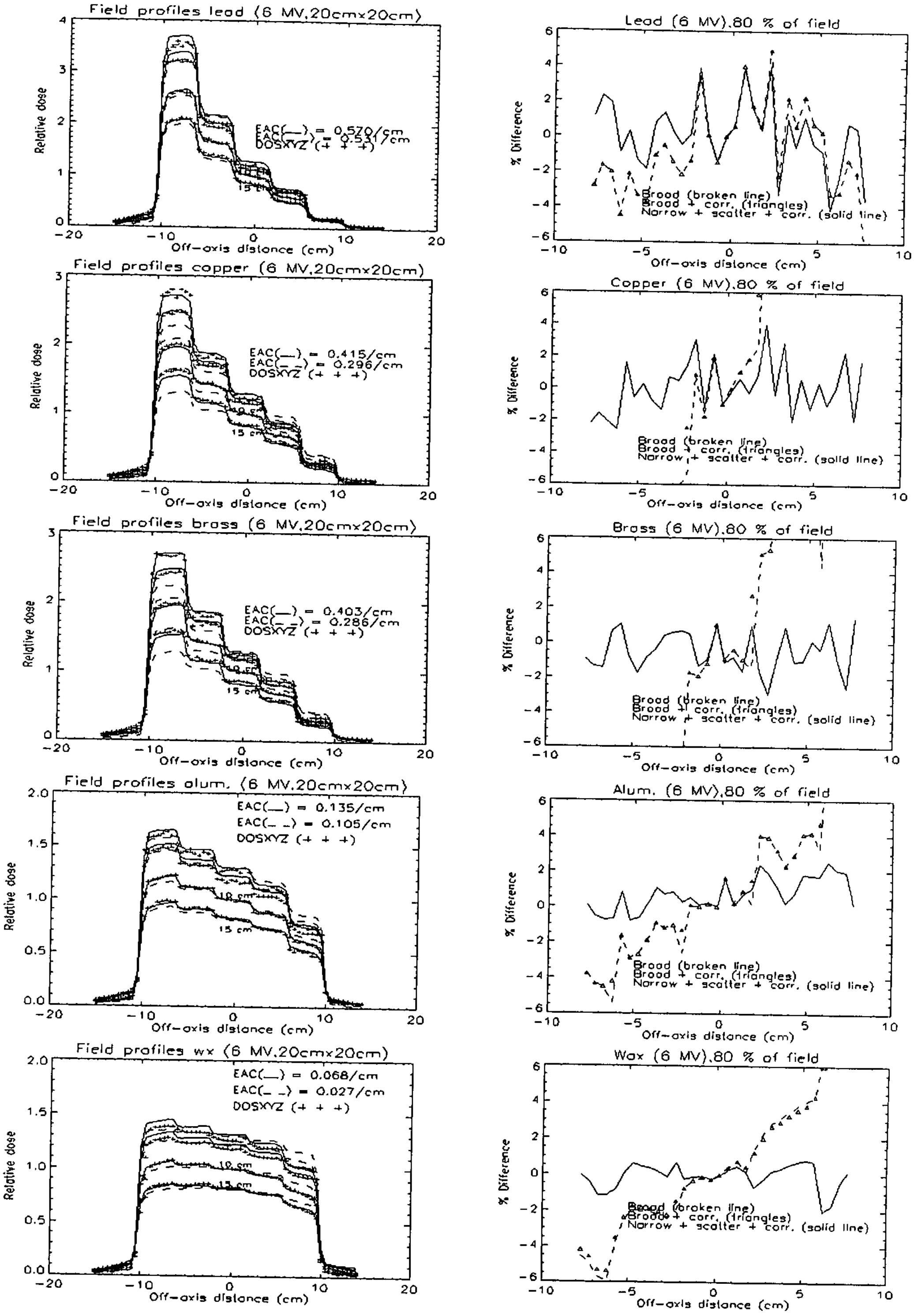

Figure 5.4a left: Relative dose profiles at 6 MV for method one (Solid line) and three (dashes) and DOSXYZ (+ + +) Right: Local dose percentage difference between all three methods and DOSXYZ dose profile as standard, at a depth of 10 cm. The variance on the DOSXYZ data were between 0.7 and 1.5 percent

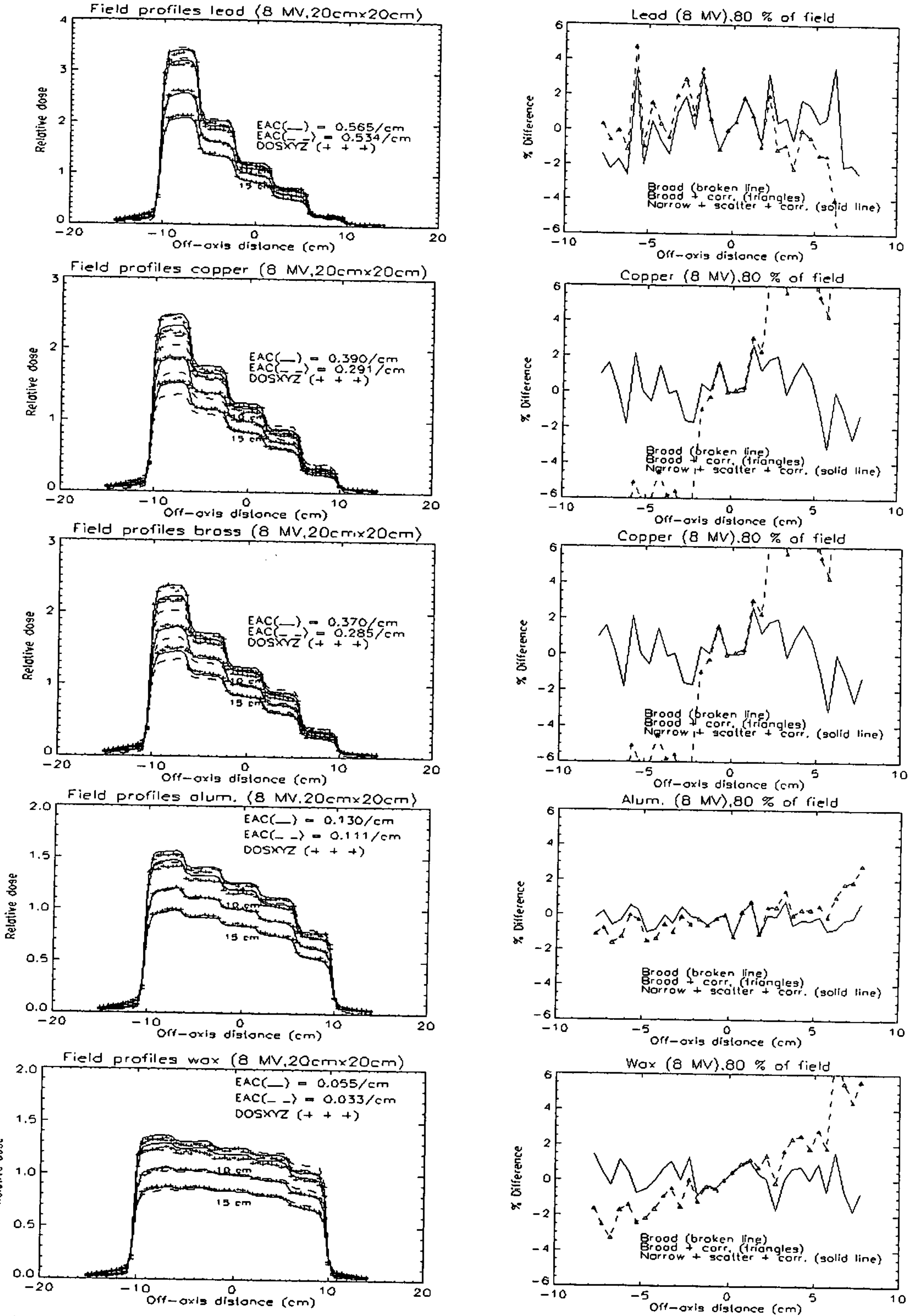

Figure 5.4b left: Relative dose profiles at 8 MV for method one (Solid line) and three (dashes) and DOSXYZ (+ + +) Right: Local dose percentage difference between all three methods and DOSXYZ dose profile as standard, at a depth of 10 cm. The variance on the DOSXYZ data were between 0.7 and 1.5 percent

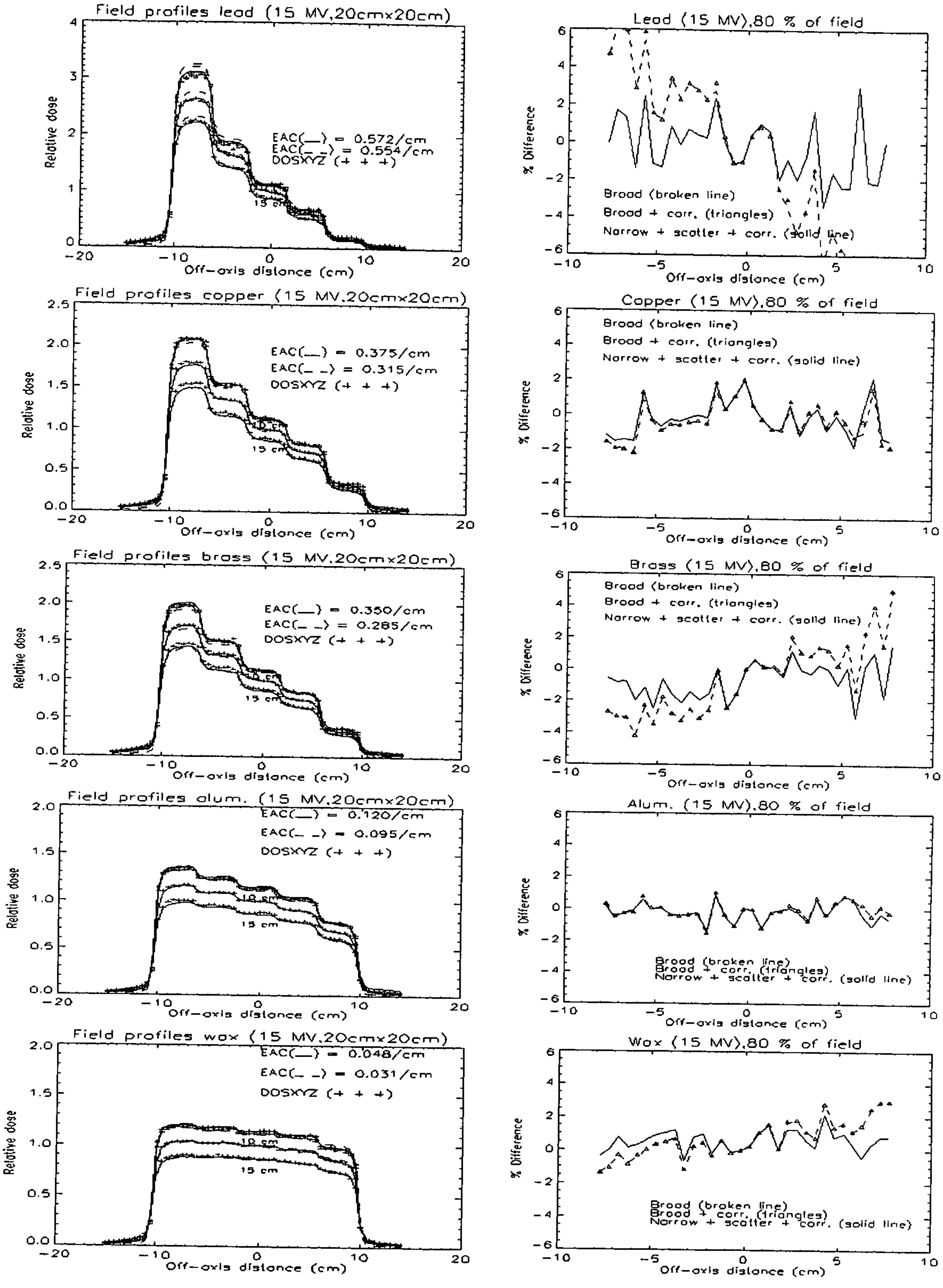

Figure 5.4c left: Relative dose profiles at 15 for method one (Solid line) and three (dashes) and DOSXYZ (+ + +) Right: Local dose percentage difference between all three methods and DOSXYZ dose profile as standard, at a depth of 10 cm. The variance on the DOSXYZ data were between 0.7 and 2.0 percent

5.3.4 Side penetration correction function

The need for such a correction function was realized since the dose profile adjustments are made on an open PB after it traversed a semi-infinite slab of compensator material with a thickness, t. Step-like geometries are not corrected for in this process. For example, the dose difference profiles in figures 5.2a – 5.2c clearly show a zigzag pattern for the broken line data (broad beam EAC). If a side penetration correction is made, the triangle data emerge, which, for at least the 5x5 cm^2 field size cases, indicate improved correlation with the DOSXYZ data. The effect of side penetration can be understood when looking at figure 5.5.

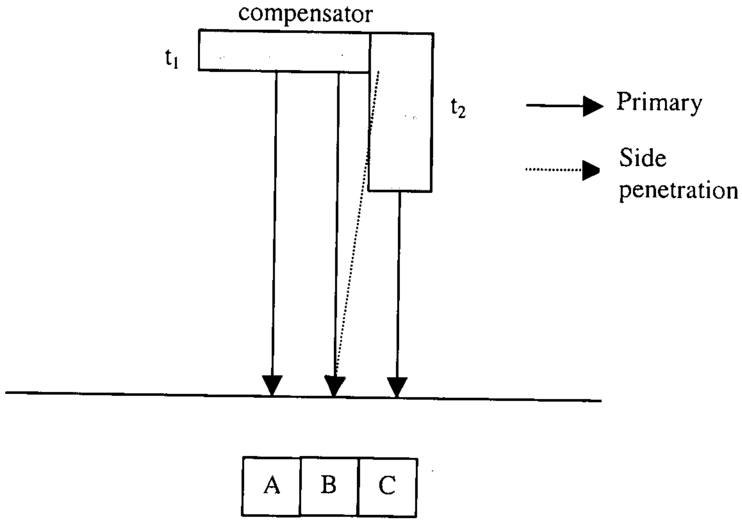

Figure 5.5: Dose is scored voxels A, B and C. Dose enhancement at B due to side penetration from the compensator element.

In figure 5.5 a step in a compensator is shown. The algorithm developed in Chapter 3 does not take side penetration into account. This leads to a under dosing in voxel B. The correction function was determined experimentally and is formulated as:

$$f(x) = 1 + 0.01\delta\left(\rho\frac{Z}{A}\right)(t_{x+1} - t_x)^{\mu} \qquad 5.1$$

where δ is a factor that can be adjusted to enhance or suppress the degree of correction, $\left(\rho\frac{Z}{A}\right)$ is the electron density (in units of N_A) of the medium and $(t_{x+1}-t_x)^{\mu}$ is the difference in the thickness between the steps. The power, μ is the EAC used in the dose calculations. Equation 5.1 is executed when $(t_{x+1}-t_x)\geq 0$, else $f(x+1)=1+0.01\delta\left(\rho\frac{Z}{A}\right)(t_{x+1}-t_x)^{\mu}$ to indicate dose enhancement at the other side of the step in the compensator. Experiments indicated that the degree of dose enhancement was roughly proportional to the electron density of the material. The factor containing the difference in step thickness was found to be too strong at the larger step differences in the step wedge shaped compensator models and it was found that by scaling it to the power of the EAC could give a reasonable correction. The factor 0.01 was included to convert the correction factor to a dose percentage correction. The function f(x) would be unity over a uniform thickness of the compensator as in dose scoring regions A and B in figure 5.5 since $t_x = t_{x+1} = t_1$. Only when a step is encountered will it have values different from unity. Also if the compensator is smooth e.g. having no discrete steps and has no large curvature then $(t_{x+1}-t_x)^{\mu}$ would become small, indicating no significant 'side' penetration. This function has a step like character and is not continuous. Functions like error functions, ERF(x), could be more useful to model side penetration but was not pursued in this study. A reason for using this function is that on a step in the compensator, as depicted in figure 5.5, not only does the dose in voxel B become enhanced but the dose in voxel C should become less due to the shielding effect of the compensator element (t_2). This is an aspect that can be investigated in the future. This, by assumption, would enable the derivation of dose correction factors that are related to the material and geometry of the compensator more accurately. In figures 5.2a to 5.2c the effect of the dose correction function is readily observed for the 5x5 cm^2 field cases. The effect is unfortunately not that observable at the other field sizes. Factors like an increase in in-phantom scatter with field size as well as the variance on the DOSXYZ data play a major role in the evaluation of the success of the correction function. The correction function f(x) is applied to the dose profile D(x) by multiplication:

$$D(x)_{corrected} = D(x) * f(x) \tag{5.2}$$

In the next set of tables (5.2 – 5.4) the following parameters are shown, which are used to describe the local percentage dose differences relative to the DOSXYZ generated data. A) The average percentage dose difference that shows how the relative dose as calculated by the three methods differs on average from that as calculated by DOSXYZ. B) The maximum percentage dose deviation among the three methods. C) The spread (maximum – minimum) in the percentage dose differences for the three methods.

These three methods of dose calculation were chosen to evaluate their individual performance against DOSXYZ.

The first dose calculation method used the open PB of which the dose was weighted according to the thickness of the compensator before applying it in a superposition algorithm. The weight factor is given as:

$$w(t) = \exp(-\mu_B t) \tag{5.3}$$

where μ_B is the broad beam EAC. This EAC value was chosen to conform to the field size studied e.g. using a value obtained for a 10x10 cm^2 field, when the dose was calculated for the same field size. Some authors have used broad beam EACs in their work with compensator materials like cement based materials [1] and gypsum mixtures.[2] Others have studied it to investigate the influence of scatter associated with broad beam geometries and interaction phantoms (patients etc.) for lead.[3, 4] The density for the cement and gypsum mixtures was matching that for aluminum ≈ 2.7 g/cm^3. These can be regarded as medium density compensator materials that is dense enough to weigh the dose sufficiently without having thicknesses that become impractical to use on a shadowtray assembly on a linac. The use of only a broad beam EAC for medium density materials may well be justified when the percentage dose differences are considered. In tables 5.2 – 5.4 the average dose difference for wax ranges from 0.5 to 3.0 percent. For aluminum it is 0.3 to 3.1 percent. For materials such as copper and lead the average dose deviation, for the chosen broad beam EACs, may vary up to 7 percent. The spread in the dose differences when compared to the DOSXYZ dose is much higher. For wax it is between 2.5 and 15 percent and for aluminum between 1.05 and 14 percent. Thus materials having similar densities as aluminum would give reasonable dose correlation, compared to DOSXYZ. The choice for such a broad beam EAC can be made more refined than that chosen for this study. A certain other aspect is that if the broad beam EAC is determined for a certain field size, it does not necessarily take scatter from the absorber into account. This can be seen from dose difference graphs e.g. for copper in figure 5.2 a, lead in figure 5.2b, wax in figures 5.2b and 5.2 c, all the materials in figure 5.3 a. This effect is very prominent for copper and brass in figure 5.4 a. This is reflected in the spread in the dose difference (method 1) in tables 5.2 – 5.4 where these values tend to be larger as a function of field size.

Table 5.2 Evaluation of the local percentage dose differences for the 5x5 cm^2 field case at 6, 8 and 15 MV obtained with three different dose calculation methods (1, 2 and 3). The narrow –and broad beam EACs are indicated by μ_N and μ_B.

5x5 cm^2 field, 6 MV				Average % dose difference			Max % dose deviation			Spread in % dose difference		
				Method								
Material	μ_N	μ_B	δ	3	1	2	3	1	2	3	1	2
Wax	0.059	0.032	1.0	0.31	1.10	1.12	0.70	3.06	3.06	0.84	4.99	4.33
Aluminum	0.131	0.118	1.0	0.58	1.45	0.89	1.34	5.01	2.83	2.04	7.27	4.08
Brass	0.400	0.366	1.0	1.08	3.43	1.32	2.44	8.57	4.57	2.44	10.3	6.54
Copper	0.410	0.358	1.0	0.65	4.63	4.23	1.30	11.06	10.40	2.35	21.46	17.27
Lead	0.570	0.555	1.3	0.85	3.56	0.89	2.46	8.26	2.89	3.91	8.26	4.63
5x5 cm^2 field, 8 MV												
Wax	0.051	0.024	1.0	0.59	2.48	2.48	1.18	8.19	8.19	1.18	11.56	10.92
Aluminum	0.122	0.112	1.0	0.43	0.65	0.41	0.81	2.14	0.82	1.10	2.59	1.52
Brass	0.370	0.342	0.5	0.63	1.79	0.52	1.32	4.37	1.09	1.32	4.37	1.09
Copper	0.391	0.358	0.5	0.69	1.99	0.71	1.10	4.24	1.98	1.16	5.06	2.80
Lead	0.540	0.530	1.3	1.34	4.64	2.46	3.62	11.97	5.47	4.66	12.20	7.89
5x5 cm^2 field, 15 MV												
Wax	0.043	0.016	0.5	0.19	2.39	2.40	0.36	7.00	7.00	0.71	10.12	9.79
Aluminum	0.115	0.093	0.5	0.37	0.65	0.33	0.80	1.77	1.06	1.02	1.77	1.06
Brass	0.350	0.304	0.2	0.48	0.88	0.43	1.10	2.04	1.21	1.12	2.28	1.45
Copper	0.370	0.320	0.4	0.44	1.21	0.36	0.90	3.08	0.82	1.39	3.54	1.29
Lead	0.560	0.530	0.5	0.99	2.41	1.14	2.43	4.98	3.40	2.42	5.20	3.62

Table 5.3 Evaluation of the local percentage dose differences for the 10 x10 cm^2 field case at 6, 8 and 15 MV obtained with three different dose calculation methods (1, 2 and 3). The narrow –and broad beam EACs are indicated by μ_N and μ_B.

				Average % dose difference			Max % dose deviation			Spread in % dose difference		
10x10 cm^2 field, 6 MV				Method								
Material	μ_N	μ_B	δ	3	1	2	3	1	2	3	1	2
Wax	0.064	0.030	0.5	0.61	2.36	2.36	1.44	8.57	8.57	2.51	12.47	12.47
Aluminum	0.134	0.111	0.5	0.51	1.98	1.94	1.51	5.39	5.39	2.41	9.92	9.54
Brass	0.410	0.360	0.5	0.90	3.12	2.72	2.58	6.88	6.12	3.44	12.45	11.69
Copper	0.415	0.338	0.8	0.57	6.40	6.37	1.48	18.32	18.33	2.13	30.48	29.11
Lead	0.590	0.546	0.1	1.23	2.44	2.41	2.27	7.38	6.96	4.43	11.99	11.57
10x10 cm^2 field, 8 MV												
Wax	0.047	0.033	0.5	0.40	1.27	1.20	1.02	3.78	3.78	1.71	6.12	6.12
Aluminum	0.125	0.101	0.5	0.47	1.64	1.57	1.32	4.45	4.45	2.39	8.50	7.88
Brass	0.375	0.337	0.2	0.76	0.88	0.89	2.14	3.46	2.74	3.60	5.36	4.63
Copper	0.385	0.335	0.2	0.65	2.60	2.63	1.75	6.37	6.37	3.23	12.45	11.84
Lead	0.580	0.532	0.5	1.37	1.57	1.68	3.05	5.89	3.77	5.58	8.51	6.88
10x10 cm^2 field, 15 MV												
Wax	0.040	0.031	0.5	0.43	0.53	0.52	1.08	1.58	1.58	1.79	2.56	2.52
Aluminum	0.115	0.085	0.5	0.60	0.96	0.97	1.81	4.21	4.21	2.58	5.38	5.38
Brass	0.305	0.286	0.5	0.92	2.48	2.27	2.93	6.33	6.27	3.52	11.23	11.16
Copper	0.370	0.303	0.5	0.85	1.97	1.78	2.13	5.24	5.05	4.12	9.13	8.90
Lead	0.570	0.555	0.5	0.89	2.78	2.70	2.23	9.52	9.52	3.67	12.55	12.55

Table 5.4 Evaluation of the local percentage dose differences for the 20 x20 cm^2 field case at 6, 8 and 15 MV obtained with three different dose calculation methods (1, 2 and 3). The narrow –and broad beam EACs are indicated by μ_N and μ_B.

20x20 cm^2 field, 6 MV				Average % dose difference			Max % dose deviation			Spread in % dose difference		
				Method								
Material	μ_N	μ_B	δ	3	1	2	3	1	2	3	1	2
Wax	0.068	0.027	1.0	0.51	3.24	3.0	2.03	10.69	9.88	2.80	16.71	15.26
Aluminum	0.135	0.105	1.0	0.91	3.11	3.12	2.51	9.62	9.62	3.30	15.04	14.12
Brass	0.403	0.286	1.0	1.07	1.21	10.21	2.94	33.10	33.10	4.37	51.44	50.69
Copper	0.310	0.296	0.3	1.36	11.03	11.10	3.99	37.58	37.58	6.59	55.35	55.35
Lead	0.570	0.530	1.0	1.47	2.12	2.12	4.16	6.43	6.44	8.14	11.34	11.34
20x20 cm^2 field, 8 MV												
Wax	0.055	0.033	0.5	0.68	1.93	1.94	1.73	7.06	7.06	3.29	10.34	10.34
Aluminum	0.130	0.111	1.0	0.45	0.80	0.80	1.27	2.83	2.83	2.07	4.43	4.43
Brass	0.370	0.285	0.1	1.33	5.74	5.74	3.22	15.81	15.81	5.74	25.35	25.35
Copper	0.390	0.291	0.1	1.09	6.69	6.69	3.16	17.83	17.83	5.80	30.10	30.10
Lead	0.565	0.534	0.1	1.47	2.39	2.39	3.62	13.52	13.52	6.23	18.26	18.26
20x20 cm^2 field, 15 MV												
Wax	0.048	0.031	0.1	0.66	1.05	1.05	2.17	2.96	2.96	2.83	4.31	4.31
Aluminum	0.120	0.095	0.1	0.46	0.43	0.44	1.37	1.53	1.53	2.23	2.42	2.55
Brass	0.350	0.285	0.1	1.03	1.96	1.96	3.04	5.01	5.01	4.57	9.21	9.22
Copper	0.375	0.315	0.1	0.86	0.94	0.96	2.08	2.19	2.20	3.91	4.19	4.20
Lead	0.572	0.554	0.1	1.33	4.53	4.52	3.44	17.04	17.04	6.42	23.56	23.56

The third dose calculation method entailed the transformation of an open PB to include the effects of scatter and beam hardening. Experimentally it was found that a narrow beam EAC is best suited to correlate the dose with that of DOSXYZ as well as the application of a side penetration function. It is well known in literature where scatter is introduced in the dose calculations and the so-called primary dose is scaled that a narrow beam EAC is best suited. The scatter dose can be included in the calculation using radially differentiated scatter-air-ratios (DSAR) [5] or analytical methods.[6 - 9] Large field compensation may also be achieved by calculation of reduction factors (equation 5.3 can be regarded as a reduction factor) through the ratio of tissue-air-ratios [10] or tissue-phantom-ratios.[11]

In this study the method for introducing scatter and beam hardening was developed and discussed in Chapter 3. In short, the dose contribution from an open PB after traversing a compensator element of thickness, t is calculated by:

$$P_{trans}(r,z) = \{P(r,z) + [\alpha(r,z) + \beta(r,z)]t\}w(t) \qquad 5.4$$

Where P_{trans} denotes the transformed open PB, P(r,z), with scatter, α(r,z) and beam hardening, β(r,z) corrections applied to it. The factor w(t) is the weight factor and has the same form as equation 5.3 and t, denotes the thickness of the compensator element. The narrow beam EAC is used, since scatter is included in the modeling of the PB. The variables r and z denotes the perpendicular radial distance (r) from the PB axis and the depth respectively. This transformed PB is then added to the dose in a 3D dose matrix by means of superposition:

$$D(x,y,z) = \sum_{i=1}^{N}\sum_{j=1}^{M} P_{trans}(x-x', y-y', z) \qquad 5.5$$

In equation 5.5 the dose (D) at point (x,y,z) equals the sum of the contribution of each transformed PB, with its PB axis located at (x′,y′), to point (x,y). The z co-ordinate coincides with the depth co-ordinate of the PB. Indices (i,j) denote the position of the PB on the dose calculation grid that contains N+1 voxel boundaries in the x direction and

M+1 voxel boundaries in the y direction. The dose calculation grid spacing and that of the PB were the same. Equation 5.2 was applied to the result of equation 5.5 to correct for side penetration. Equation 5.5 is valid for a parallel beam with unit uniform fluence, otherwise, the fluence, $\Phi(x',y')$ should be included as well as an inverse-square correction to take beam divergence into account for a non-parallel beam.

For all the cases studied in figures 5.2a – 5.4c, method 3 gave the best performance (solid lines). As mentioned, the increasing variance on the data (particularly at the larger fields) introduced noise on the percentage difference data. Bearing this in mind, it is still possible to see that the method developed in this study gives encouraging results. From tables 5.2 – 5.4 it can be observed that the average percentage dose difference is less than 2 percent, lead being the least accurate. This again might be related to larger variance on the DOSXYZ data, since it absorbs most of the incoming photons. For cases where the variance is at its smallest e.g. wax and aluminum in figures 5.2a – c there is very good agreement with the DOSXYZ data. These discrepancies are slightly more than the variance of about 0.3 percent. From table 5.2 the spread in the percentage dose difference is in the order of 2.5 percent for most materials excluding lead which is about 4.5 percent, probably due to more variance on the DOSXYZ data. This higher dose difference spread is also observed at the other field sizes. This parameter indicates how well the calculated data conforms to the DOSXYZ data and serves to indicate additional information, not necessarily reflected in the average percentage dose difference. For example in table 5.2, for wax at 6 MV, the average dose difference for method 1 is 1.12 percent and that for method 3, 0.31 percent. The spread in the percentage difference is 4.33 and 0.84 percent respectively. The average percentage dose difference indicates satisfactory performance for both dose calculation methods, but the spread in these values indicate that method 1 does not conform as well as method 3 to the DOSXYZ values.

The maximum percentage dose deviation is also noted. This is to indicate the maximum local percentage difference with respect to the DOSXYZ data. This must also be evaluated with variance taken into consideration. In all cases method 3 outperformed methods 1 and 2 in tables 5.2 – 5.4.

5.3.5 The effect of scatter and beam hardening correction

To emphasise the effect of scatter and beam hardening, data in this section are presented where the narrow beam EACs have been used for all the calculations. Calculations were done for wax, aluminum, brass, copper and lead, for 5x5 cm^2 (figure 5.5 a) and 20x20 cm^2 (figure 5.5 b) fields at beam energies of 6 (left) and 15 MV (right). The data now presented is for method 3, with the same narrow beam EACs as shown in tables 5.2 and 5.4. The two graphs show the difference between the results with and without scatter and beam hardening correction. The side penetration correction function was enabled in both cases. These data were obtained at a depth of 10 cm in the water phantom.

From figure 5.5a it can be observed that the exclusion of scatter and beam hardening cause a relative percentage dose deviation of between 2 – 3 percent at 6 MV beam energy (left column). At 15 MV (right column) this deviation ranges from 4 – 7 percent at the field edges. These dose deviations are caused by the combined effect of scatter and beam hardening that is absent on the broken line data. The broken line can be viewed as the relative primary dose contribution for an open PB that is not corrected for scatter and beam hardening.

In-phantom scatter increases as a function of depth in, for example, a water phantom, leading to a decrease in EAC values. At 6 MV more lateral scatter should be present than at 15 MV. This would counter the effect of beam hardening to a greater extent at 6 MV than at 15 MV, which could explain the larger deviations encountered at 15 MV. Also prominent is that the deviation increases as a function of material density, being larger for brass, copper and lead, than wax and aluminum at 15 MV. This might be due to more forward scatter generated in the compensator at 15 MV, when compared with 6 MV beams. At 6 MV the photons from the compensator are scattered relatively more lateral, leading to lower dose in the phantom.

For the 20x20 cm^2 field case shown in figure 5.5b an attempt was made to reduce the variance on the displayed data. A 5 point floating average, boxcar, method was employed to smooth the percentage dose difference data, rather than the raw MC generated dose profiles, since more sophisticated filtering techniques are needed in that case. The simple filtering method was employed here merely to resolve the difference between the methods more clearly. The smoothing process introduced bias [12] of about one percent at the field edges. The smoothing process actually improved the performance of the method where only the narrow beam and side penetration corrections were used.

The results in figures 5.5a and 5.5b clearly show that the inclusion of scatter and beam hardening, as developed in Chapter 3, into the dose profile calculations have a significant impact on the shape of the profile. In all cases the use of only a narrow beam EAC will cause the dose difference profile to be slanted, indicating under dosing and over dosing that increases at increasing off-axis positions. The magnitude of the effect ranges from about one percent up to several percent.

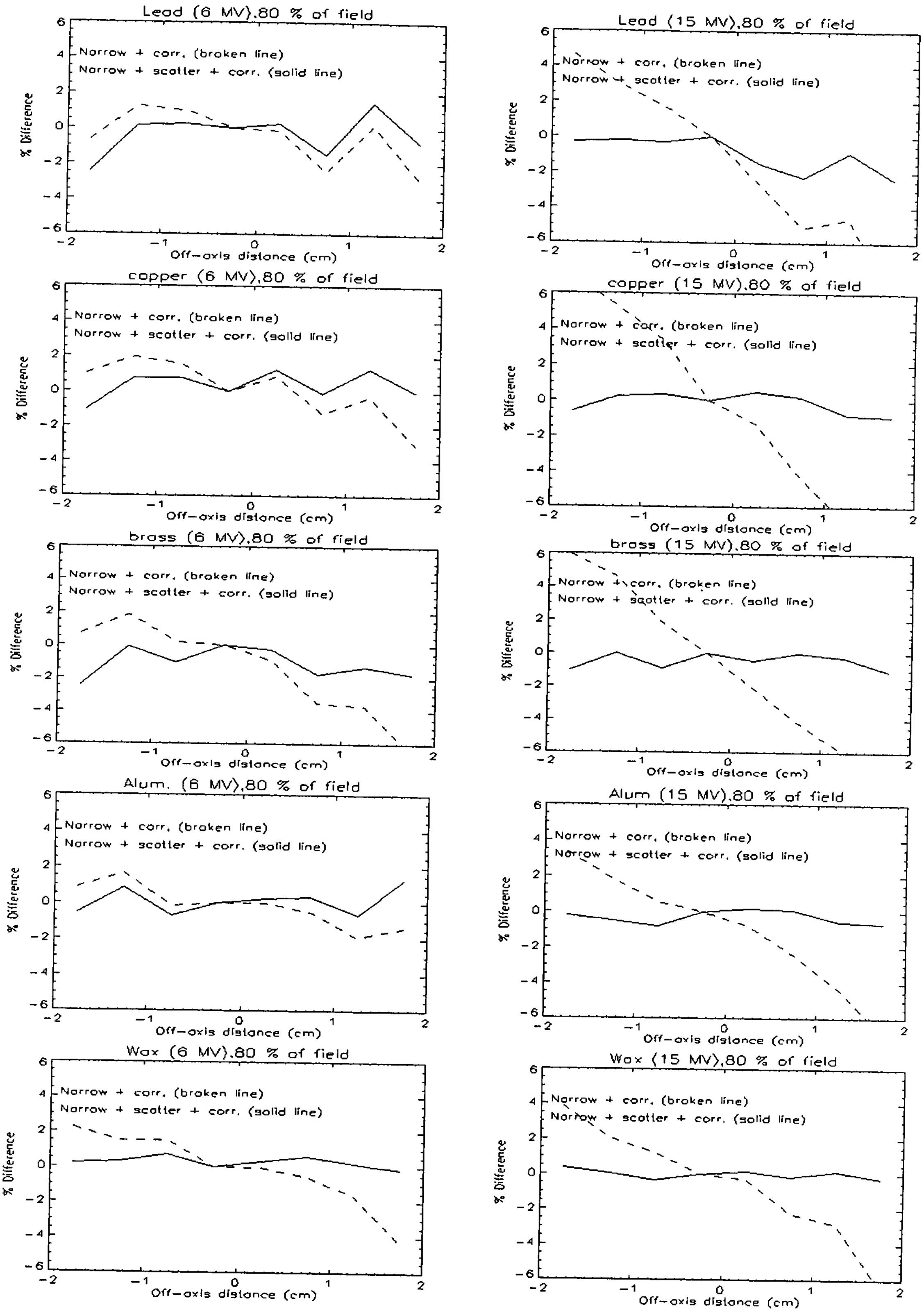

Figure 5.5 a. Percentage dose difference profiles at 10 cm depth for the 5x5cm² fields relative to DOSXYZ for 6 MV (left column) and 15 MV (opposite graphs). The solid line represents the full dose calculation and the broken line without scatter and beam hardening included.

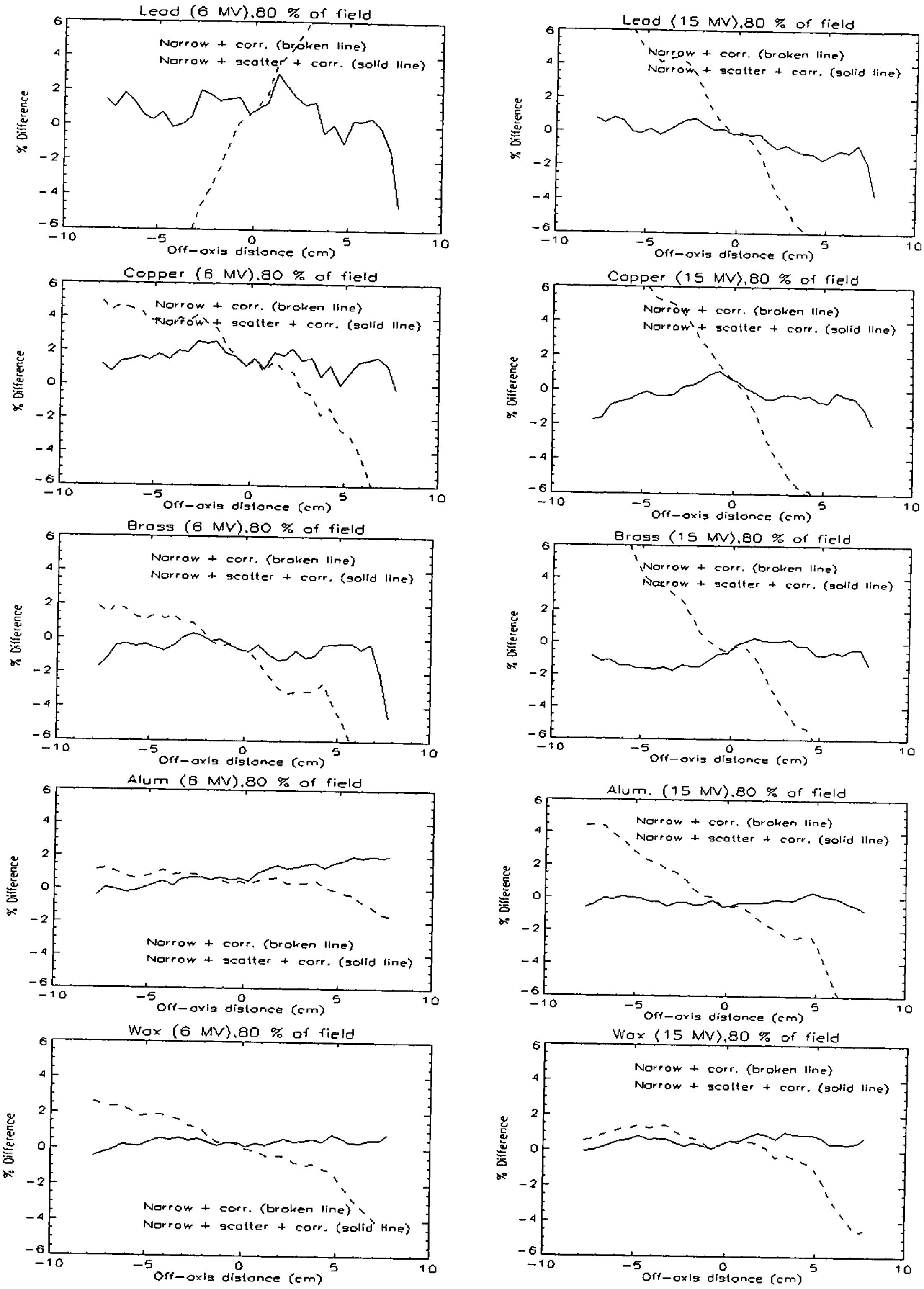

Figure 5.5b. Percentage dose difference profiles at 10 cm depth for the 20x20cm^2 fields relative to DOSXYZ for 6 MV (left column) and 15 MV (opposite graphs). The solid line represents the full dose calculation and the broken line without scatter and beam hardening included.

5.3.6 The properties of the determined narrow beam EACs

In Chapter 2, EACs for beamlets were calculated and related to the theoretical narrow beam EAC values. In the current study it was found that the optimal EAC values that resulted in the best match between the relative dose profile data as calculated with the CPS to that of the DOSXYZ calculated relative dose profiles, differed by a small amount from the EACs as calculated in Chapter 2. These optimally derived EACs will now be referred to as determined EACs.

This section is devoted to the relationship between the determined EAC values and the EAC values in Chapter 2. The determined EAC values are taken from the first column of tables 5.2 to 5.4. In the graphs shown in figure 5.6 the average of the determined EAC values for a material at a certain energy over the three field sizes is used. The reason for using the average EAC values over the three field sizes is that the dose calculation model, in this case a PB model, can be regarded as a sum of a primary and a scatter 'pencil beam'. If the PB were weighted (equation 5.3) then a narrow beam EAC would be the most suited. The choice for this narrow beam EAC should not be field size dependant, since the scatter part and to a lesser extend the beam hardening part of the modified PB should take care of the field size dependence in dose calculations. This is also reflected in the determined narrow beam EAC values in tables 5.2 to 5.4, if they are evaluated for a given material and beam energy over the three field sizes used. The field size dependence on the EAC in Chapter 2 is for varying beamlets or finite-sized PBs.[13, 14] In this study only a single size finite-sized PB was used.

In figure 5.6 the plots show the relationship between the averaged, determined EAC values (y-axis) against the theoretical EAC values from table 2.3 in Chapter 2. Also shown in each graph are a linear regression line, its equation and the correlation coefficient (R^2). For each beam energy, the correlation indicated a linear dependence between the average of the determined and theoretical EAC values. The linear function is shown on each graph in the form:

$$\mu_N = a\mu_T + b \qquad 5.5$$

Where μ_N indicates the determined narrow beam EAC and μ_T is the theoretical counter part. In the graphs μ_N is replaced by variable y and μ_T by x.

From the graphs, and a evaluation of constant, a, in equation 5.5 it can be seen that the determined EAC is about 12 percent lower than the theoretical narrow beam EAC at 6 MV. At 8 and 15 MV this number is 8 percent. A possible reason why the determined EAC is less than the theoretical EAC is as follows: The PB used in the dose calculations was rebinned into a 0.5x0.5 cm^2 voxel array. This corresponds to a finite-size PB. A true PB has no cross sectional area and enters a phantom in a point. Its EAC would correspond closer to the theoretical EAC that was calculated in Chapter 2. For example, at 6 MV, the average of the determined EAC values for brass is 0.404 cm^{-1} over the field sizes used in the dose calculations. Its theoretical counter part has a value of 0.438 cm^{-1}. The constant, b, in equation 5.5 has a relative small value compared to the EAC for aluminum and the other higher density materials. For wax this value is in the order of 10 percent, and thus influence the EAC significantly. Ideally this constant should be zero, since, if the theoretical EAC is non-existent, then the determined EAC should also not exist. This would imply either no beam, and/or, no attenuator in the beam. Thus constant (a) can be assigned to the finiteness of the PB, while constant (b) only serves to optimize the regression procedure and should ideally be zero.

From table 2.2 in Chapter 2 this determined value for the EAC would lie between that for a square beamlet with a side length ranging between 0.5 and 1.0 cm. It is clear from the graphs that the other materials also show this effect. The only, subtle, exception is for the case of wax. At 6 MV its averaged determined EAC has a value of 0.064 cm^{-1}, compared to the calculated theoretical EAC of 0.052 cm^{-1}. At 8 and 15 MV the respective values are better correlated and are found to be nearly the same. The much higher value for the determined EAC might be due to inaccuracies introduced in the calculation method of the theoretical EAC and / or inaccuracies in the beam hardening and scatter modulation for wax at this energy. Nevertheless the determined value gives satisfactory dose calculation results.

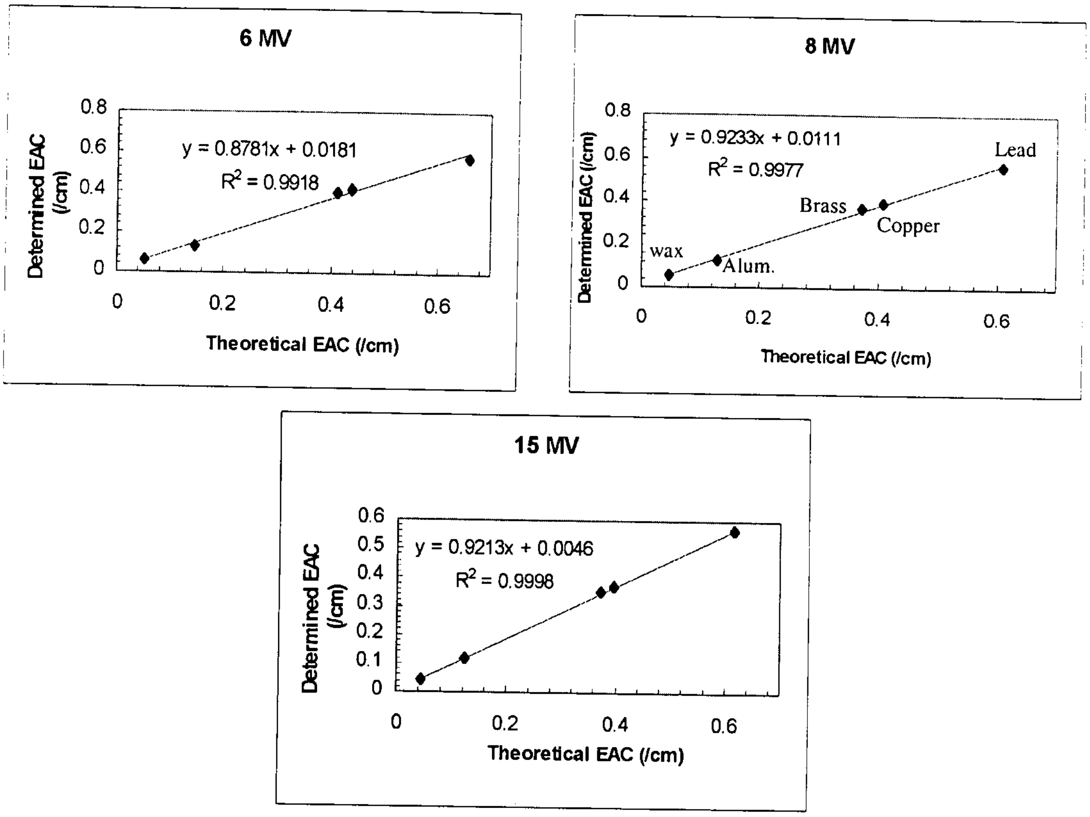

Figure 5.6. Plots of the Determined EAC against the theoretical (calculated) EAC at 6, 8 and 15 MV. The dots represent the average value for the EAC for a material over the three studied field sizes. These materials are shown for the 8 MV case and correspond to the data points on the other graphs.

As a final remark, variance on the data does seem to have some influence since its can be seen that the correlation between the determined EAC and the theoretical EAC is improving as a function of beam energy.

The relationship between the determined EAC and theoretical EAC also suggest that the grid size of the PB may play a role in the determination of their values from dose calculation evaluations, since the well-correlated regression lines do not have a unit slope. The value of these slopes might be linked to the PB grid spacing. In Chapter 2, table 2.3 it can be readily observed that the beamlets, that can be constructed from a smaller finite-sized PB, have different EACs and that these EACs decrease as a well defined function of beamlet size. They also display a depth dependency. Thus it is possible for the determined EACs to also display a depth dependency, since these were derived for a depth of 10 cm. This depth dependency is noticeable in the dose profiles in figures 5.2a to 5.4c. The dose profiles show better correlation with the DOSXYZ data at 10 cm than at other depths, particularly near the surface.

5.4 Determination of the shape of a compensator from a known dose weight matrix (DWM)

The main objective of the compensator planning system (CPS) is to derive a compensator thickness map that can give a certain prescribed dose distribution in a plane of interest. This dose distribution may be expressed in terms of a dose weight matrix. In the previous sections of this Chapter the dose profiles were evaluated for a step wedge compensator. Corresponding dose profiles were calculated on the CPS. A side penetration correction function were also introduced to correlate the calculated relative dose profiles with that of DOSXYZ. These relative dose profiles were calculated at a depth of 10 cm in water.

In this section the side penetration function in conjunction with the determined EAC is used to derive a suitable compensator from a given dose weight matrix (DWM). This DWM or intensity modulated (IM) group was chosen arbitrarily (see figure 5.7) but will in practice be obtained from inverse planning systems.[15 - 23] A DWM is used to design the appropriate compensator. In Chapter 4 the optimization method for obtaining the compensator thickness map was described.

The DWM was set up to produce a step wedge compensator for a field size of 15x15 cm^2, using aluminum as the beam modulation material. The EAC chosen was for a beam energy of 15 MV. It was taken as the average value of (0.115, 0.115 and 0.120 cm^{-1}) as determined from tables 5.2 to 5.4 for each beam size case. The average EAC value was 0.117 cm^{-1}. The DWM was set up as shown in figure 5.7. The PB grid was 0.5x0.5 cm^2 in the xy-plane.

The DWM is to be interpreted as follows: The weight in each section determines how the dose at 10 cm depth should be adjusted. A weight of 1.0 implies that the dose at 10 cm depth should be the same as the dose on the beam axis (reference dose). Any other weight value should then be the corresponding fraction of the particular reference dose.

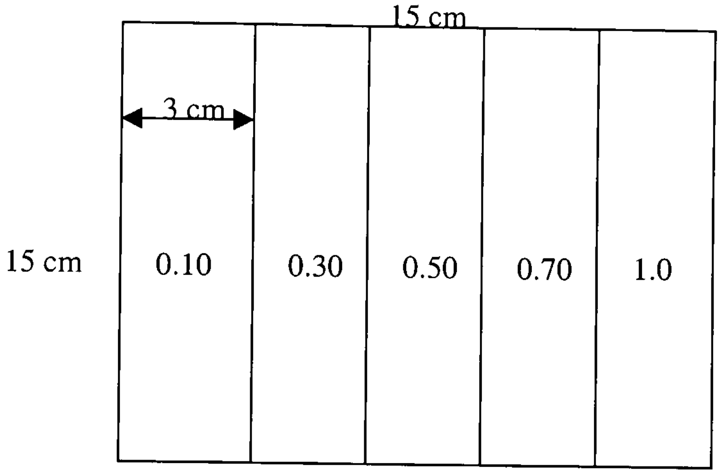

Figure 5.7 A schematic representation of a DWM used for a 15x15 cm^2 field. In each section the dose weight is shown. Each section covered an area of 3x15 cm^2.

For the purpose of illustration, the optimization code performed 6 iterations, starting with the open beam. The results are shown in figure 5.8. The thickness of the aluminum compensator was calculated and the new dose distribution was calculated. For iteration number 1, the graph shows that the dose profile is such that the dose is over estimated. This is because the primary dose has been scaled with the weight factor, from which the initial compensator element thicknesses were derived. This exponential scaling does not include scatter. Thus relative to the normalization point, the dose is over estimated at other parts on the dose profile. If no scatter were present in the PB, then the correct dose profile would have been accomplished the first time. For iteration number 2, the compensator elements are made thicker to suppress the primary dose contribution and the calculated dose profile already shows good agreement with the sought profile. The calculated dose profiles were normalized to the maximum at 10 cm depth. From the set of graphs it can be observed that the calculated dose converges satisfactorily within 4 iterations. This number is also within performance levels of other optimization codes. [24] Only at the steps in the arbitrary dose profile discrepancies occur. These discrepancies tend to diminish only slightly after three further iterations. These discrepancies and those obtained at the field edges are due to the finite dose gradient of a PB. It must be mentioned that the arbitrary dose profile chosen does not mimic a real dose distribution in terms of field edge effects and the described discrepancies would always be present at the 'steps' or any region where the dose changes abruptly. Thus four iterations should be sufficient as shown in this test.

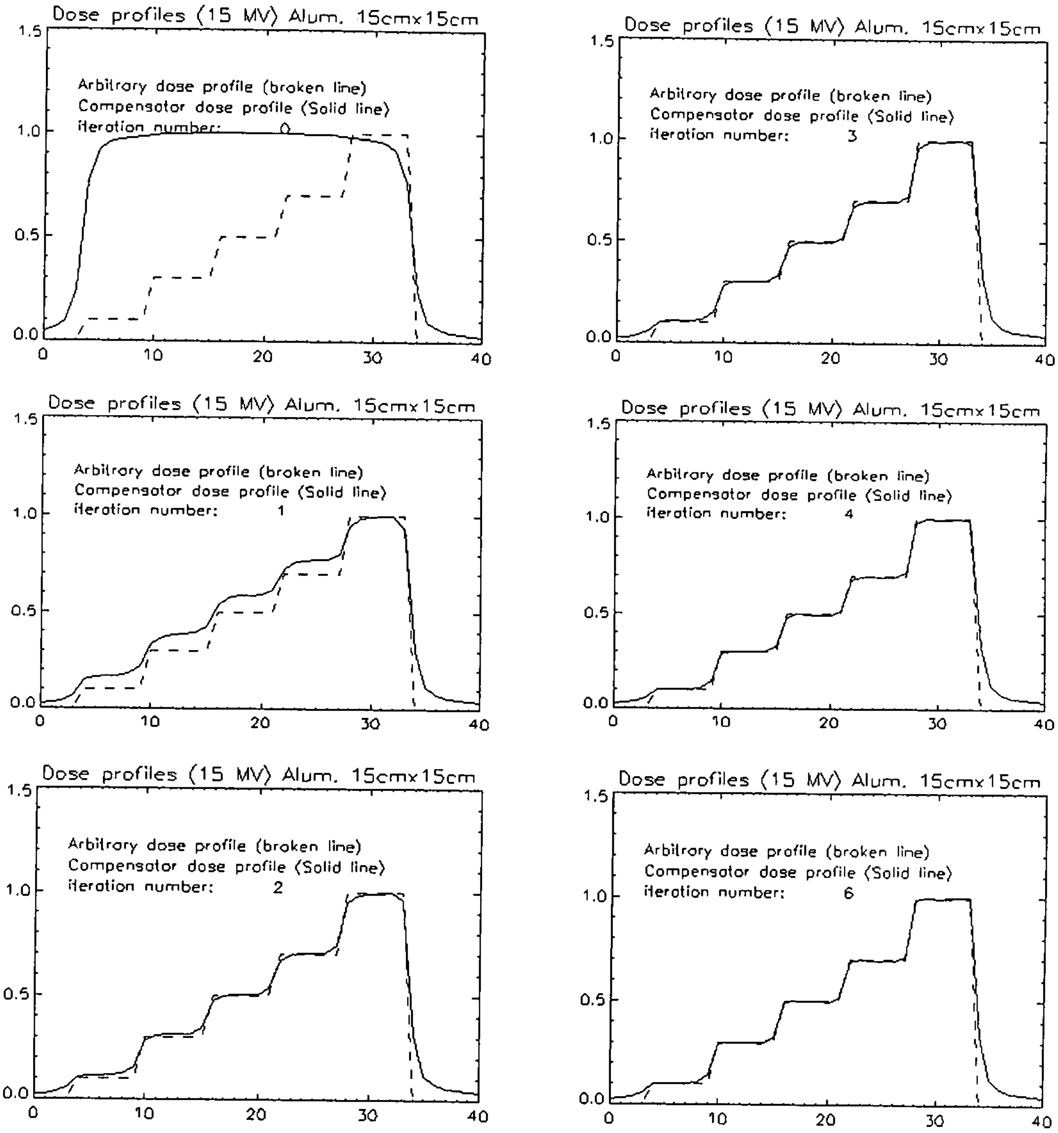

Figure 5.8: The convergence of the dose as calculated with the CPS and a compensator (solid line) to that of the DWM profile (broken line) at a depth of 10 cm in water. The number of iterations is indicatd on each graph and increases from top to bottom in the left and right columns respectively. Note that the field size is in arbitrary units.

In figure 5.9 3-D representations are shown for the dose sought from the DWM, the calculated dose and the compensator shape derived to get this calculated dose. The results shown were obtained after 4 iterations. The dose profiles in figure 5.8 are just 2-D representations of the 3-D data in figure 5.9.

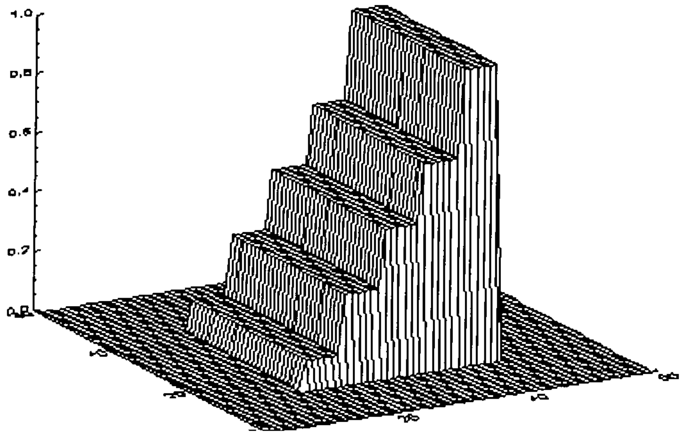

Arbitrary 3-D dose profile determined from the DWM.

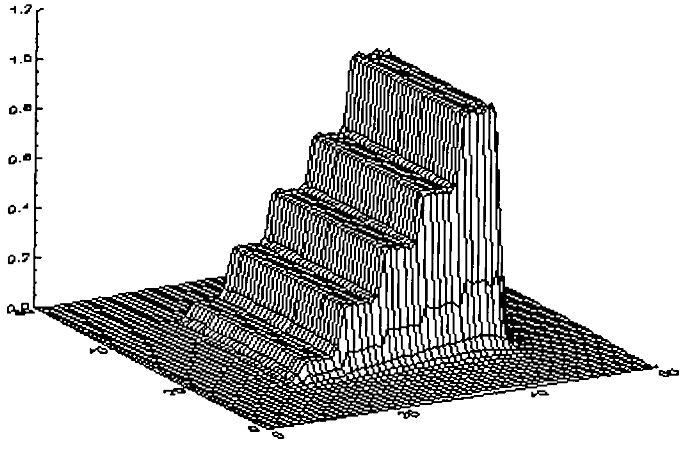

Calculated 3-D dose distribution after 4 iterations.

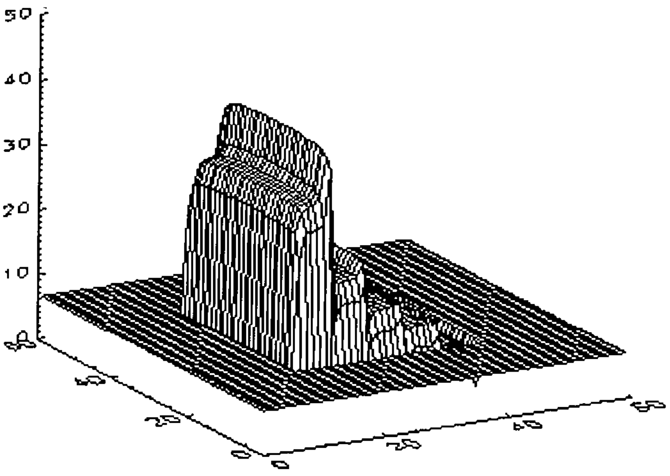

Shape of designed compensator after 4 iterations resulting in the calculated dose distribution (above).

Figure 5.9 The DWM dose profile at 10 cm depth in water is shown (top) with the calculated dose profile for 15 MV x rays at the same depth (middle). The bottom shows the calculated compensator shape for obtaining the calculated dose distribution. Field dimensions are expressed in arbitrary units.

From figures 5.8 and 5.9 it can be observed that there is good correlation between the DWM and the calculated dose profiles and distributions. The bottom part of figure 5.9 shows the compensator shape with a somewhat peculiar shape that warrants an explanation and is provided with the aid of figure 5.10.

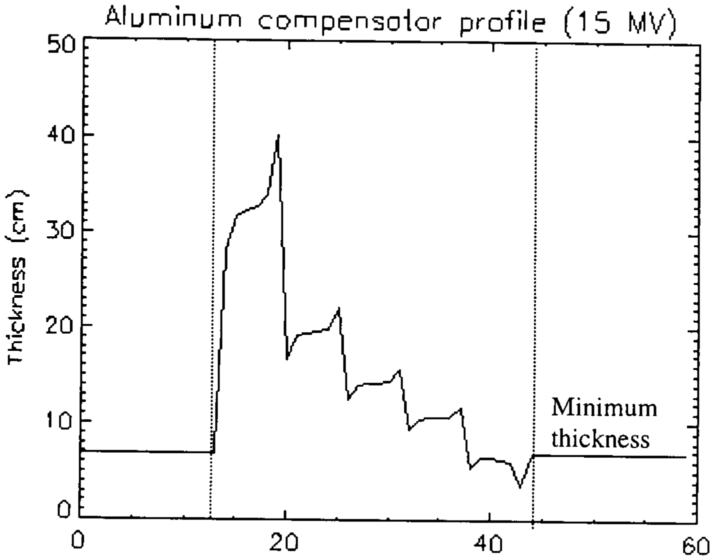

Figure 5.10. A cross sectional profile for the compensator shown in figure 5.9 (bottom).

The compensator profile shown has a finite minimum thickness outside the field boundaries (broken lines). The optimization procedure was altered to avoid the inclusion of negative compensator thickness. Instead, if a part of the compensator were found to be negative, the absolute value of this thickness was added throughout the compensator. This resulted in the minimum thickness of the compensator outside the field boundary, since the starting compensator has zero thickness throughout. Inside the field boundary a region exists where the compensator thickness is less than the minimum thickness. Examination of the top left graph in figure 5.8 shows that the normalized dose profile at 10 cm depth is less than the DWM dose at the corresponding location. The optimization code would adjust the compensator by assigning a negative value to it. This would result in an enhancement of the dose when weighed by equation 5.3.

Near the steps in the DWM the compensator profile has local maxima and minima that appear as over- and under shoots. Just before the step, the dose is suppressed, and after the step the dose is enhanced (local minimum in thickness). This is an attempt of the optimization code to model the step-like profile of the DWM, using the finite sized pencil beam profile.

5.4.1 Primary and total scatter dose contributions

The optimization code scaled the primary dose component of the PB after adjusting it for beam hardening and scatter. The thickness profile in figure 5.10 has large values, ranging from 40 cm down to 7 cm. From this thickness profile the amount of primary radiation can be calculated, using equation 5.3, since the dose maximum is unity. For the primary dose the thickness of aluminum required to suppress the dose to a fraction of 0.1 would be:

$$t = -\frac{\ln(D_{DWM} / D_o)}{EAC} = -\frac{\ln(0.1)}{0.177cm^{-1}} = 19.7cm$$

Thus if only the primary dose was taken into account, then a thickness of 19.7 cm aluminum would have been required to adjust the dose to 10 percent of its maximum value. The thickness in figure 5.10 is nearly twice that. This extra thickness is required since scattered radiation from the compensator and in-phantom scatter contributes to the dose at a certain location in the water phantom. From this argument it would then in principle be possible to calculate the dose enhancement from the total scatter contribution.

If the local required dose was to be 10 percent of the maximum open beam dose, and the value of the designed thickness is 23 cm, then the primary dose contribution can be deduced from:

$$D_{prim} = \exp(-0.177cm^{-1} * 23cm) = 0.02 \text{ or 2 percent.}$$

This indicates that for a beam energy of 15 MV, with an aluminum compensator, with a local thickness of 23 cm, and a field size of 15x15 cm^2, the primary dose contributed would be 2 percent, and thus the total scatter contribution must be 8 percent. This calculation can be applied over the total thickness profile to yield a total scatter profile as shown in figure 5.11.

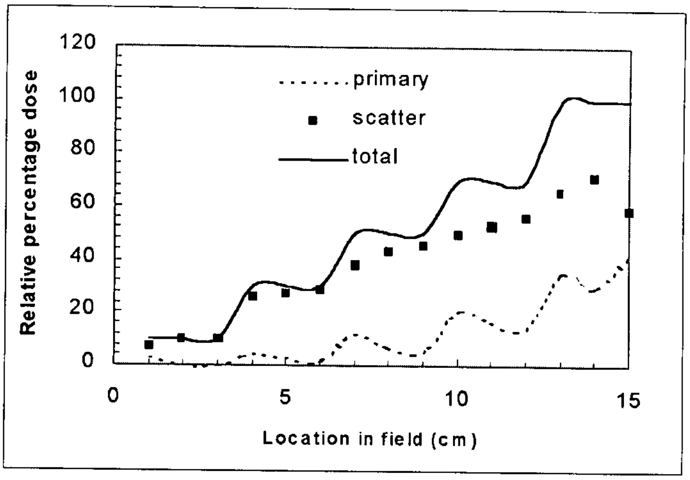

Figure 5.11. Calculated primary and scatter dose components from the compensator profile in figure 5.10. Dose points were sampled 3 per step (solid line).

The scatter component of the dose makes up a much larger portion of the dose at locations where the compensator is thickest, compared to the region where it is thinnest. This scatter dose comes from the compensator itself as well as from in-phantom scatter in the water phantom. At the regions where the most dose suppression is sought e.g. at 10 percent relative dose almost all of the dose contribution is scatter related. The scatter fraction gradually becomes less at larger total dose values. Interestingly, the step like profile is modulated by the primary dose profile, whereas the total scatter profile shows a more gradual trend. This is because multiple scatter has a smoothing effect that tends to soften sharp edges in dose gradients e.g. the calculated dose profiles in figure 5.8.

The method described for determining the total scatter component does not lend itself to the determination of the absolute amount of scatter from the compensator itself. This could be done using the open PB with no scatter adjustment of its profiles, but is not pursued further in this study. Studies [25] have shown that for a 4 MV beam, field size of 20x20 cm^2, a 1 cm copper sheet would produce about 6 percent dose enhancement at a retractal distance of 30 cm on the beam axis. Others [26] studied scatter-to-primary ratios

(SPRs) and found for internal wedges that it varied between 4.4 – 5.4 percent at 6 and 25 MV for field sizes exceeding 20x20 cm^2. Others [6] measured the dose enhancement due to scatter from variable thickness lead-bismuth alloy sheets to be in the order of 2.5 percent at 6 MV and Co-60. For a silicone-tungsten mixture at 6 MV the scatter ranged from 1 – 4 percent for corresponding thickness of 2.2 and 4.4 cm for a 16 x 16 cm^2 field.[27] Others found that the SPR for brass and lead is much the same at beam energies between 4 and 23 MV, but depend on the thickness and the material used. For a 15x15 cm^2 field is was found to be in the order of 3.5 percent.[28] From these studies it can be said that the beam energy does not significantly change the percentage dose contribution due to scatter. The thickness of the material plays a role and that for aluminum the results would most probably lie within the ranges of 2 – 6 percent.

5.5 Conclusion

In this Chapter the performance of the CPS was tested with the PB models developed in Chapter 3. Benchmarking to corresponding DOSXYZ MC simulations showed that for a step wedge shaped compensator a) A side penetration function was needed to account for penetration radiation. This worked very well for the 5x5 cm^2 field cases. B) Suitable EACs were determined and it was found that they are to a large extent field size independent, but show a linear relationship with the theoretical narrow beam counterparts. These slightly lower values for the determined EACs were ascribed to the finite size of the PB. It was also found that the use of a broad beam EAC does not necessarily lead to accurate dose profile modeling, although they were determined for the same field size as that studied. The impact of the scatter and beam hardening corrections on the PB was tested. It was found that the use of the determined EACs without scatter and beam hardening corrections lead to percentage dose discrepancies of 2 – 3 percent at 6 MV and 4 – 7 percent at 15 MV. For the 20x20 cm^2 case the percentage dose curves were smoothed with a box car averaging method, but it introduced bias when compared with original results as discussed.

The dose profiles for the method developed were in very good agreement with the benchmarking DOSXYZ MC generated relative dose profiles. The average dose deviation was less then 1.5 percent for all materials, beam energies and field sizes. The maximum dose deviation was largest for lead in the small field case, on average 1 percent larger. The spread in the dose was also largest for lead. This is thought to be due to increased variance on the DOSXYZ data, since lead is a strong photon absorber. Similar effects were observed for the other field sizes. The increase in field size also introduced an increase in the variance. This influenced the impact of the side penetration function and its delta (δ) constant was set at a low value for the largest field cases. For the smallest field case it was set at nearly unity throughout.

All the data gathered in the DOSXYZ benchmarking process e.g. determined EAC values and delta for the side penetration function were used in an attempt to construct a compensator from a DWM. It was found that a compensator could be designed from this WDM within three to four iterations. If the determined EAC was excepted to weight only the primary dose, then the total scatter dose from this designed compensator could be calculated, from knowledge of the primary dose.

A point of concern is the very large thickness of aluminum required to bring the dose down to 10 percent of its maximum value at a depth of 10 cm in water. This suggests that materials such as lead, copper, woods alloy, brass and other high atomic number/density materials would be more practical in cases where the dose has to be attenuated to such a degree. If the dose gradient and variation were not as severe as in the DWM then aluminum would suffice.

It was found that the variance on the DOSXYZ data used in the benchmarking process plays a significant role. Thus the method developed here would be about 1.5 percent accurate in calculating dose profiles for a compensator for fields smaller than 10x10 cm^2. For the larger fields this could amount to inaccuracies in the order of 2 – 3 percent. These inaccuracies would be relative to the local dose values. Due to long DOSXYZ MC simulation times not enough time was on hand to reduce the variance significantly further than reported here as it took 3 months to complete.

The use of the CPS would thus be to calculate a compensator (typically from a DWM) as a starting point for an MC code on which the full simulation would then be run. The effects of scatter and beam hardening as outlined in Chapter 3 would make it very difficult to adjust dose profiles to include the effects of scatter and beam hardening by other means than using analytic methods like the one developed in this and other studies. This approach differs from simpler ones when an MLC is used for field fluence modulation. Scatter and beam hardening through an actual compensator would have to be modeled during beamlet dose distribution weighing that is absent on MLC based systems.

5.6 References

[1] M.S. Thomsen and N. Ulsø, " Attenuation of 4-20 MV x rays by a new compensator material of cement.", Med. Phys. **29**, 2427 - 2432 (2002).

[2] K.J. Weeks, B.A. Fraass, and K.M. Hutchins, ' Gypsum mixtures for compensator construction.', Med. Phys. **15**, 410 – 414 (1988).

[3] J. Van Dyk, ' Broad beam attenuation of high energy photons in lead', XIV ICMBE and VII ICMP, ESPOO, Finland (1985).

[4] P.M.K. Leung, J. Van Dyk, and J. Robins, ' A method of large irregular field compensation.', Br.J.Radiol. **47**, 805 – 810 (1974).

[5] P.C. Shragge, and M.S. Patterson, ' Improved method for the design of tissue compensators.', Med. Phys. **8**, 885 – 891 (1981).

[6] M.K. Islam, and J. Van Dyk, ' Effects of scatter generated by beam-modifying absorbers in megavoltage photon beams.', Med. Phys. **22**, 2075 – 2081 (1995).

[7] A. Ahnesjö, L. Weber, and P. Nilsson, ' Modeling transmission and scatter for photon beam attenuators.', Med. Phys. **22**, 1711 - 1720 (1995).

[8] Y. Mejaddem, S. Hyödynmaa, R. Svensson, and A. Brahme, ' Photon scatter kernels for intensity modulating radiation therapy filters.', Phys. Med. Biol. **46**, 3215 – 3228 (2001).

[9] E.E El-Khatib, E.B. Podgorsak, and C. Pla, ' The effect of lead attenuators on dose in homogeneous phantoms.', Med. Phys. **13**, 928 – 935 (1986).

[10] A.L. Boyer, ' Compensating filters for high energy x rays.', Med. Phys. **9**, 429 - 433 (1982).

[11] T. Chu, K. Lee, and P. Dunscombe, 'A technique for the evaluation of a missing tissue compensator system.', Med. Phys. **20**, 713 – 716 (1993).

[12] M Fippel, and F. Nüsslin, ' Smoothing Monte Carlo calculated dose distributions by iterative reduction of noise.', Phys. Med. Biol., **48**, 1289 – 1304 (2003).

[13] J.D. Bourland, and E.L. Chaney, 'A finite-size pencil beam model for photon dose calculations in three dimensions.', Med. Phys. **19**, 1401 – 1412 (1992).

[14] O.Z. Ostapiak, Y. Zhu, and J. Van Dyk, ' Refinements of the finite-size pencil beam model of three-dimensional photon dose calculation.', Med. Phys. **24**, 743 – 750 (1997).

[15] S. Liu, B.K. Lind, and A. Brahme, ' Two accurate algorithms for calculating the energy fluence profile in inverse radiation therapy planning.', Phys. Med. Biol. **38**, 1809 – 1824 (1993).

[16] T. Holmes, and T.R. Mackie, ' A comparison of three inverse treatment planning algorithms.', Phys. Med. Biol. **39**, 91 – 106 (1994).

[17] Y. Liu, F-F. Yin, and Q. Gao, ' Variation method for inverse treatment planning.', Med. Phys. **26**, 356 – 363 (1999).

[18] J. Seco, P.M. Evans, and S. Webb, ' An optimization algorithm that incorporates IMRT delivery constraints.', Phys. Med. Biol. **47**, 899 – 915 (2002).

[19] C. Cotrutz, and L. Xing,'Using voxel-dependent importance factors for interactive DVH-based dose optimization.', Phys. Med. Biol. **47**, 1659 – 1669 (2002).

[20] Y. Chen, D. Michalski, C. Houser, and J.M. Galvin, ‘ A deterministic iterative least-squares algorithm for beam weight optimization in conformal radiotherapy.’, Phys. Med. Biol. **47**, 1647 – 1659 (2002).

[21] D.J. Convery, and M.E. Rosenbloom, ‘ Treatment delivery accuracy in intensity-modulated conformal radiotherapy.’, Phys. Med. Biol. **40**, 979 - 999 (1995).

[22] S.M. Crooks, A. Pugachev, C. King, and L. Xing, ’ Examination of the effect of increasing the number of radiation beams on a radiation treatment plan.’, Phys. Med. Biol. **47**, 3485 – 3501 (2002).

[23] A. Boyer, L. Xing, C-M. Ma, B. Curran, R. Hill, A. Kania, and A. Bleier, ‘ Theoretical considerations of minitor unit calculations for intensity modulated beam treatment planning.’, Med. Phys. **26**, 187 – 195 (1999).

[24] G.S. Mageras, R. Mohan, C. Burman, G.D. Barest, and G.J. Kutcher, ‘ Compensators for three-dimensional treatment planning’, Med. Phys. **18**, 133 – 140 (1991).

[25] P-H. Huang and B.E. Bjärngard, “Scattered photons produced by beam-modifying filters”, Med. Phys. **13**, 57 – 63 (1986).

[26] T.C. Zhu, B.E. Bjärngard, and P. Vadash, ‘ Scattered photons from wedges in high-energy x-ray beams.’, Med. Phys. **22**, 1339 – 1342 (1995).

[27] T. Xu, P.M. Shikhaliev, M. Al-Ghazi, and S. Molloi,’ Reshapable physical modulator for intensity modulated radiation therapy.’, Med. Phys. **29**, 2222 – 2229 (2002).

[28] M.E. Castellanos and J.C. Rosenwald, “Evaluation of the scatter field for high-energy photon beam attenuators”, Phys. Med. Biol. **43**, 277 – 290 (1998).

CHAPTER 6

Retrospective comments and future developments of this study

6.1 Introduction

IMRT applications in the radiotherapy environment are fast becoming state of the art. Compensators can be used to realize this treatment modality. When compared to more sophisticated hardware such as MLCs, compensators introduce additional challenges with regard to changing beam characteristics i.e. compensator-induced scatter and spectral changes in the beam. This ultimately leads to perturbations in the absorbed dose in the patient, and, as a result, have to be taken into account for successful IMRT. In this study, a method was developed to model these changing characteristics.

The approach used was based on the concept of a beamlet that corresponds to a compensator element. This beamlet was modeled with a finite sized PB. A method was developed to account for induced scatter and beam hardening by evaluation of the dose profiles of a PB, after traversing a compensator element, made up from a certain material, with thickness, t. This enabled the inclusion of scatter and beam hardening in an effective manner, by adjusting the dose profiles of a cylindrical PB, rebinning it into a cartesian PB and using superposition to add its 3-D dose distribution into a dose matrix. This technique was also applied in the inverse problem of designing a compensator to fit a pre-determined dose profile in a water phantom.

6.2 Assumptions of this study

The first an important assumption of this study was that the x-ray beams were parallel. In reality x-ray beams, emerging from a linear accelerator, are diverging. It was decided to use parallel beams, since it simplified the development of the CPS. It was believed that this would not influence the final conclusions seriously. To take beam divergence into account would entail the tilting of the PBs and applying an inverse square correction.

Another important aspect is that the flattening filter of the accelerator would introduce significant spectral changes in the beam, i.e. it would be ‘harder’ at the central beam axis, and become ‘softer’ near the field edges. This is because of the shape of the filter. This was not taken into account in this study. Only a single, invariant, energy spectrum was assumed. This potential problem could be solved if the energy spectra of the photons emerging from different regions of the flattening filter were determined. Poly-energetic PBs could then be composed, as a weighted sum of mono-energetic PBs, to model the spectral variation across the diameter of the flattening filter. If these constructed poly-energetic PBs traversed the compensator, the alteration of their dose profiles could be handled in a similar way than that for the PBs in this study. This statement is supported by the fact that over the three beam energies studied, the compensator-induced scatter and beam hardening could be modeled by the same functions. The fitting parameters were material and energy dependent.

Further, the modeling of the beam characteristics was demonstrated for a set of materials that had a wide range in atomic number, physical density and electron density. Thus if any other compensating material or energy spectrum were to be used, the method developed in this study would most probably by applicable.

6.3 Future developments

The main contribution of this study was the method developed to include beam hardening and induced-scatter to an open PB dose profile and the development of a CPS to assist in the design of a compensator. In practice, however, other issues must be addressed before this model can be implemented clinically at radiotherapy, National Hospital. A suitable source model will have to be developed for each linear accelerator in our institute. Firstly, with the necessary enhancement, the method developed in this study can be used to model a realistic compensator with the CPS. This compensator model can then be imported into an MC treatment planning code for a full MC simulation to determine the dose-distribution in a patient model.

To realise this goal, the PB based method for deriving the shape of the compensator seems to be the fastest, most efficient way compared to MC simulations. In the latter case, changing the shape of the compensator entails a re-run of the whole simulation that would be too time consuming. The method developed in this study gives a quick result in terms of changing beam characteristics as the thickness of the compensator elements are adjusted. This is not possible with MC, but MC is necessary for the final dose distribution calculation which includes the compensator and patient inhomogeneities.

The second issue is that if compensators are to be used locally for IMRT applications an inverse planning code will have to be obtained or developed to calculate the beamlet weights needed for the design of compensators with the CPS. Using compensators would enable the utilization of IMRT in a relatively economic way and as a further bonus, would reduce the total number of monitor units delivered by the accelerator. As a result, more patients could benefit from the advantages of IMRT. This would simplify quality control since only the compensator is added to the accelerator, as opposed to more comprehensive and costly tests that have to be performed when an MLC is used.

The third issue would be to develop suitable quality assurance programs for using compensators as beam intensity modulation devices.

ABSTRACT

In this study the effect of compensator-induced scatter on external beam dose calculations were studied for compensators of wax, aluminum, brass, copper and lead for 6, 8 and 15 MV parallel x-ray beams. An outline is given of the necessity for the inclusion of compensator induced scatter in the design of compensators for their use in IMRT applications. A method is described for deriving effective attenuation coefficients (EACs), as calculated by the DOSXYZ Monte Carlo (MC) code. Various properties of the EACs were studied, among which their dependence on small beam (beamlet) sizes as well as their depth dependence in water. These EACs are used for the initial approximate design of a compensator. In conjuction with these EACs, scatter and beam hardening is included in the compensator modeling process. Compensator-induced scatter and beam hardening properties were studied in some detail. The EGSnrc based DOSRZnrc MC code was used to study the evolution of a pencil beam (PB) as it traverses different thicknesses of a compensator material. It was found that the relative dose profiles of the PB could be adjusted for scatter and beam hardening using empirically derived functions, and that these adjustments were proportional to the thickness of the compensator material. A compensator planning system (CPS) is described, used in the design of a compensator. Dose calculations are performed with this CPS using the superposition method for cartesian PBs. An algorithm is described that transforms the cylindrical PB as obtained with the DOSRZnrc MC code, into a cartesian PB. The CPS was tested for a step wedge shaped compensator over square field sizes with side lengths of 5, 10 and 20 cm. A correction function was introduced to account for side penetration in the compensator. It was found that the relative dose profiles calculated with the CPS at a depth of 10 cm in water was within 1.5 percent of similar dose profile data derived from DOSXYZ MC dose calculations for a 5x5 cm^2 field. For the 20x20 cm^2 field, the accuracy was within 3 percent in most cases and beam energies. It is also demonstrated how an aluminum compensator can be designed by an iterative method with the CPS to yield a dose profile that conforms accurately to a pre-determined dose profile, such as would be produced by an inverse planning system for IMRT treatments.

Key words: Compensator, Monte Carlo, DOSRZnrc, beam hardening, scatter, IMRT, effective attenuation, pencil beam.

ABSTRAK

In hierdie studie is die effek van kompensator-geïnduseerde verstrooïng op eksterne bundel dosis berekeninge vir was, aluminium, brass, koper en lood kompensators ondersoek, vir paralelle x-straal bundels met energieë van 6, 8 and 15 MV. 'n Oorsig asook die noodsaaklikheid van die studie word uiteengesit t.o.v. kompensator-geinduseerde verstrooïng en die gebruik daarvan in IMRT toepassings. 'n Metode vir die berekening van effektiewe attenuasie koefisiënte (EAKs), met die DOSXYZ Monte Carlo (MC) program, word beskryf. Verskeie eienskappe van die EAKs is bestudeer waaronder die afhanklikheid t.o.v. klein subvelde en diepte in water ondersoek is. Hierdie EAKs word gebruik om 'n voorlopige benaderde kompensator te kan ontwerp. Saam met hierdie EAKs word x-straal bundel verstrooïng en verharding dan ingesluit in die kompensator ontwerp proses, soos bestudeer. Die EGSnrc gebasseerde DOSRZnrc MC program is gebruik om die evolusie van 'n dunbundel (DB), soos dit deur verskillende diktes kompensator materiaal beweeg, te ondersoek. Daar is gevind dat die relatiewe dosis profiele van die DBs aangepas kan word vir verstrooïng en verharding deur die gebruik van empiries- afgeleide funksies, en dat hierdie aanpassings eweredig aan die dikte van die kompensator materiaal is. 'n Kompensator beplanningstelsel (KBS) word beskryf wat dan gebuik word in die ontwerp van 'n kompensator. Dosis berekeninge is met die KBS gedoen en werk op die beginsel van die superponering van kartesiese DBs. 'n Algoritme wat 'n silindriese DB (soos bereken met die DOSRZnrc program) na 'n kartesiese DB omskakel, is ontwikkel. Die KBS is getoets vir 'n stapwig vormige kompensator model vir vierkantige velde met sylengtes van 5, 10 en 20 cm. 'n Korreksie funksie is ingevoer om vir sydelingse stralingspenetrasie in die kompensator te kan korrigeer. Daar was gevind dat dosisprofiele, soos bereken met die KBS by 'n diepte van 10 cm in water binne 1.5 persent ooreengestem het van 'n soortgelyke dosis profiel wat met die DOSXYZ MC program bereken is vir 'n veld grootte van 5x5cm^2. Vir 'n 20x20cm^2 veld was die akkuraatheid binne 3 persent vir die meeste materiale en bundel energieë. Daar word ook gedemonstreer hoe 'n aluminium kompensator ontwerp kan word met 'n iteratiewe metode met die KBS om 'n dosis profiel te lewer wat akkuraat

ooreenstem met 'n voorafbepaalde dosis profiel, soos wat deur 'n inverse beplanningstelsel vir IMRT toepassings, geproduseer sal word.

Acknowledgements

I hereby which to express my deepest gratitude to the following:

The head of the Medical Physics department, Prof. M.G. Lötter for his encouragement and allowing me ample time to conduct this study.

My promotor, Prof. C.A. Willemse for devoting his time and effort in numerous discussions and invaluable guidance, resulting in the crystallization of this study.

My wife, Magda, for sacrificing her time and invaluable encouragement that made this all worth while.

My colleagues, from whom I have derived many ideas and attacking points in making this study a concrete realization.

The Medical Research Council of South Africa for providing funds for this study.